Two-qubit microwave quantum logic gate with $^{9}Be^{+}$ ions in scalable surface-electrode ion traps

Von der Fakultät für Mathematik und Physik
der Gottfried Wilhelm Leibniz Universität Hannover

zur Erlangung des akademischen Grades

Doktor der Naturwissenschaften
- Dr. rer. nat. -

genehmigte Dissertation von

M.Sc. Henning Hahn

2019

Referent:	Prof. Dr. Christian Ospelkaus
Korreferent:	Prof. Dr. Piet Oliver Schmidt
Korreferent:	Prof. Dr. David Lucas
Tag der Promotion:	05.07.2019

Abstract

Towards the goal of a large-scale quantum computer based on trapped ions, near-field microwaves represent a promising approach to perform the technically challenging key operation of a two-qubit entangling gate. In this thesis we present the first microwave-driven two-qubit gate in $^9Be^+$ ions employing a first-order field-independent qubit transition and a scalable surface-electrode ion trap at room temperature. We test the quality of the gate operation by producing a maximally entangled state and measuring the resulting state preparation fidelity in a reduced tomography procedure. For the best two-qubit gate achieved in the system we find this fidelity to be $\mathcal{F} = 98.2 \pm 1.2\,\%$. Following a comprehensive error analysis based on numerical simulations and experimentally determined input parameters, we identify current infidelity contributions of the apparatus. Here, the natural error source of the microwave near-field approach, namely fluctuating AC Zeeman shifts, could be reduced to the 10^{-4} level due to the optimized design of the employed microwave conductor. As we find that the three largest errors can all be reduced upon purely technical improvements, higher fidelities are feasible in the future. Besides the gate realization, the thesis also comprises the initial characterization of the employed ion trap as well as the design and construction of a Raman laser at $\sim 313\,\mathrm{nm}$ which is utilized to perform near ground state cooling of radial modes of a single- and two-ion crystal. Here, ensuing heating rate measurements on a single-ion's radial modes show good agreement with the electric-field noise spectral density expected from literature given the chosen mode frequency and nearest ion-to-electrode distance of $70\,\mu\mathrm{m}$. Finally, we present the operation of a first multi-layer ion trap whose electrode layout features a 3-dimensional microwave conductor intended for performing microwave-driven two-qubit gates. Following a characterization of the resulting near-field pattern using a single ion as a local field probe, we find the multi-layer conductor to have significantly better field properties when compared to an equivalent single-layer design. Given these promising results, future work will focus on the integration of similar microwave circuitry in a multi-zone trap array as envisioned by the QCCD architecture.

Keywords: trapped ions, quantum information processing, hyperfine qubits, near-field microwaves, two-qubit gates

Contents

Chapter 1

Introduction

1.1 Quantum computing with trapped ions

A quantum computer as proposed by Deutsch [DP85] is a universal quantum information processing (QIP) device that has the potential to outperform its 'classical' counterpart in specific problems such as simulating other quantum systems [Fey82], factorizing large numbers into their prime factors [Sho94] or searching large databases [Gro97]. The origin of the quantum computer's performance advantage is based on the exploitation of unique quantum mechanical properties of its elementary unit of information, the quantum bit (qubit), namely the storage and manipulation of superposition states. However, in order for a quantum computer to be of practical use and surpass even state-of-the-art supercomputers in specific tasks, tens to millions of qubits need to be precisely controlled and extremely well isolated from the environment, thus making a physical realization of a large-scale quantum machine challenging.

Currently, a wide variety of platforms for quantum computation including spins in semiconductors, superconducting circuits or atoms is developed all of which offer specific advantages and drawbacks [LJL+10].

While it remains unclear which platform will ultimately succeed, trapped ions are among the most promising and experimentally advanced platforms to date for which recent developments include the implementation of quantum algorithms [MNM+16, FML+17] as well as the realization of a 5-qubit quantum processor [DLF+16]. Here, the qubit is encoded in electronic energy levels of

fundamentally identical atomic ions which are confined in ultra-high vacuum using a 3-dimensional (3D) pseudopotential produced by static and oscillating electric fields [Pau90]. As multiple ions in the same trapping potential repel each other due to the Coulomb interaction, they exhibit collective modes of harmonic motion which, given a sufficiently low temperature, need to be treated quantum mechanically and act as a bus for quantum information processing [CZ95]. Consequently, the two types of degrees of freedom in trapped ion systems are given by the collective motional modes as well as the electronic spin states of each individual ion. Although all elementary requirements for a quantum computer, known as the DiVincenzo criteria [DiV00], have been successfully demonstrated with ions, two main challenges remain when scaling up to large numbers of qubits. Both are briefly presented in the following.

Improving fidelities

The first challenge originates from the requirement of the error probability of all elementary operations (i.e. readout, qubit initialization, quantum logic operations) to stay below a certain threshold in order to enable the implementation of error correction schemes. This is necessary for QIP to be efficient as the fragile quantum information encoded in the qubits can easily decohere due to interactions with the environment. While multiple correction schemes have been proposed, it is often expected that an error probability per operation of 10^{-4} would be sufficient to implement so-called "fault-tolerant" quantum computation [Pre98, Kni10].

In this context, especially the demonstration of a universal gate set, i.e. a group of quantum logic operations any unitary operation on arbitrarily many ions can be composed of, remains technically very demanding. It has been shown that a universal gate set can be expressed by a complete set of single-qubit gates as well as a two-qubit entangling gate [BBC$^+$95, DiV95]; hence present efforts are concentrated on improving these two logic operations. While fault-tolerant single-qubit gates have already been demonstrated several years ago, two-qubit gate fidelities have just recently reached compatible errors as shown in Fig. 1.1. The reason for the latter to be much harder to achieve arises from the fact that, besides control over the spin state as in single-qubit operations, two-qubit gates also require precise control over the ion motion.

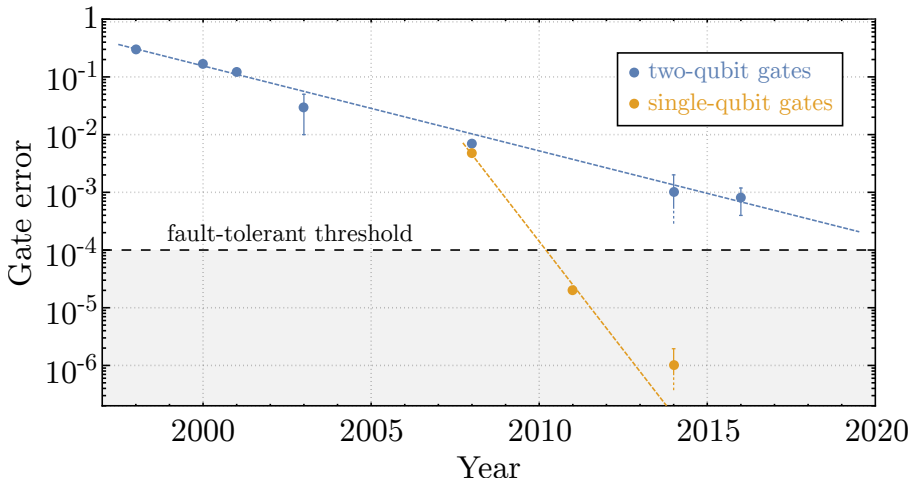

Figure 1.1: Selection of the best single- and two-qubit gate errors achieved in trapped ion systems over the years independent of the used ion species or employed technique. For fault-tolerant quantum computing a gate error below 10^{-4} is required. Following the time at which the gates have been demonstrated, the corresponding references for the single-qubit and two-qubit gate data are [KLR+08] [BWC+11], [HAB+14] and [TWK+98], [SKK+00], [RKM+01], [LDM+03], [BKRB08], [BHL+16], [GTL+16], respectively.

Improving scalability

The second big challenge is given by the demonstration of all elementary operations in a scalable architecture without exceeding the aforementioned error threshold per operation when scaling up. Here, the historically first and probably most intuitive approach is to "simply" increase the number of ions in a single Paul trap while utilizing tightly focused laser beams for their manipulations. Although this is expected to be feasible for the implementation of quantum simulations that are already not tractable with classical computers (the current state-of-the-art includes quantum simulations with 53 ions [ZPH+17]), it is, however, practically limited to a few tens to a hundred of ions [MK13]. The reason for this is that the motional mode spectrum of a chain of N ions scales as $3N$ and hence becomes too dense to allow spectral addressing of specific modes for quantum logic operations without off-resonantly exciting other spectator modes. Additionally, the speed at which entangling gate operations between two ions can be performed also generally decreases with the number of ions due to the increasing mass, thus making fast information processing in large ion chains challenging [MRR+14].

One promising approach to overcome this limitation is the so-called 'quantum charge-coupled device' (QCCD) which was initially proposed by Wineland *et al.* in 1998 [WMI+98] and further discussed in [KMW02]. Here, the ions are held in a trap array consisting of individual zones to perform dedicated tasks such as storage, loading, processing or readout whereas different zones are interconnected via ion transport. Consequently, the number of ions per trap zone can dynamically be broken into smaller groups if required, enabling significantly better control and access to the motional modes when compared to a large ion chain scenario.

Although the QCCD approach is also actively pursued in 3D traps, the so-called surface-electrode ion traps [CBB+05, SCR+06] in which all electrodes are located in a 2-dimensional plane are likely more suitable for large-scale QIP applications as they enable the realization of complex electrode layouts with high reproducibility and precision inherently given by microfabrication techniques. In fact, a strong motivation for the development of surface-electrode ion trap technology was exactly to simplify the fabrication process with respect to 3D ion traps in order to improve scalability [SCR+06].

Over the last decade multiple research groups have successfully demonstrated different aspects of the QCCD architecture in suitable trap structures including fast ion transport through 'T' and 'X' junction in a 3D trap array [HOS+06, BOV+09, BGL+12], ion shuttling through 'Y' and 'X' junctions in microfabricated 2D trap arrays [AUW+10, MHS+11, WAF+13] as well as sympathetic cooling of 'logic ions' with an accompanying refrigerant ion [BDS+03]. The latter is necessary as ions with encoded quantum information, also referred to as 'logic ions', might heat up during storage or transport and hence need to be re-cooled near the Doppler limit or lower before multi-qubit gate operations with high fidelity can again be performed. While any scattered photon on the logic ions from direct laser cooling would irreversibly destroy the quantum information, one possible solution is sympathetic cooling by a different ion species in the same harmonic potential whose required cooling wavelength has negligible effect on the logic ion [KKM+00].

However, towards higher numbers of qubits also the QCCD approach will face scalability challenges as e.g. the preservation of optical laser access for cooling and manipulation using bulky optics outside the vacuum chamber becomes at some point spatially restricted. While possible workarounds for this limitation is the focus of active research and includes the integration of micro-optics like nanophotonic waveguides [MBM+16], mirrors [MVL+11] or

sensors [SVL+17] in surface-electrode ion traps, it is likewise advisable to additionally investigate ways to reduce the required laser overhead in general.

Thesis focus and outline

One approach which contributes to the solution of both challenges towards a large-scale quantum computer based on trapped ions is the microwave near-field approach [OLA+08]. Here, the ions are trapped in scalable surface-electrode ion traps and are manipulated by the fields emanating from embedded microwave conductors rather than tightly focused laser beams which, as will become apparent in the following chapter, is expected to have certain advantages in achieving high gate fidelities. In fact, the lowest gate errors demonstrated with microwaves belong to the best in the field and, in case of single-qubit gates, even represent the current state-of-the-art [HAB+14].

In this thesis, we aim to advance the microwave near-field approach by the following points:

(1) presenting the first microwave-driven two-qubit gate with $^9Be^+$ ions

(2) utilizing a single microwave conductor whose optimized geometry addresses main error sources of previous near-field experiments

(3) testing a 3D microwave conductor for its application to drive entangling gates

The remaining part of the thesis is structured as follows. In **chapter 2**, the basic idea of the microwave near-field approach to drive multi-qubit gates is introduced. Besides deriving the Hamiltonians for quantum logic operations, the chapter also comprises the two-qubit gate theory as well as the needed tools for state analysis. **Chapter 3** presents the chosen ion species and qubit transition and explains basic operations such as qubit initialization, manipulation and readout. **Chapter 4** describes the apparatus used to perform most of the experiments presented later in the thesis. This includes the vacuum setup, laser systems, the magnetic field setup as well as microwave and trap drives. **Chapter 5** comprises all experimental results that have been achieved with the single-layer ion trap and includes a characterization of the near-field pattern using a single ion as local field probe, the two-qubit gate realization as well as the experimental part of the error budget analysis. **Chapter 6** is about the initial testing of a multi-layer ion trap which has been developed

and fabricated in our group. Besides a brief description of the trap design, the chapter contains secular frequency measurements and a characterization of the near-field distribution. The final **chapter 7** briefly summarizes the most relevant results and gives an outlook towards future perspectives of the experiment.

Chapter 2

Microwave-driven quantum logic

This chapter gives an introduction to microwave-driven quantum logic and describes some basic theory behind the experiments performed within this thesis. The chapter starts with a general motivation of the microwave near-field approach and the focus of our research group. Subsequently, the interaction of a single ion with microwave fields is discussed and relevant transitions are identified. Finally, we describe how these transitions can be employed to perform an entangling gate between two ions following the Mølmer-Sørensen protocol.

2.1 Motivation

As mentioned in the introduction, single-qubit and multi-qubit gates are essential ingredients in QIP. Here, single-qubit gates are operations that purely manipulate the electronic state of single qubits in order to e.g. create superposition states, while typical two-qubit gates additionally involve the collective ion motion to mediate an interaction among spin states of different ions.

From an experimental point of view, two-qubit gates are still technically very demanding although the first realizations have already been demonstrated about 20 years ago [TWK$^+$98, SKK$^+$00, LDM$^+$03, SKHR$^+$03]. Among the most successful multi-qubit gates so far are the ones based on the proposals of Mølmer and Sørensen [MS99, SM99, SM00] which utilize a bichromatic radiation field to apply a spin-dependent force on the ions and drive them

along closed loops in motional phase space for a suitably chosen basis[1]. Here, the enclosed area of the performed loops is proportional to an accumulated phase [Ber84], which, given a properly tuned interaction of the ions with the radiation field, can be used to create entanglement between the spin states of multiple ions in another choice of basis.

One great advantage of this kind of entangling gates is that for its ideal implementation the collective ion motion returns back to its initial state after the operation and hence is only transiently excited. As a consequence, the scheme is negligibly sensitive to the initial motional state in typical ion trapping experiments and can also be performed on Doppler-cooled ions, thereby significantly relaxing experimental requirements when compared to earlier proposals [CZ95]. Furthermore, no single-ion addressing is required as both ions can be exposed to the same radiation field.

Experimentally, the spin-dependent force is applied by means of so-called "sideband transitions" which couple the spin and motional state of the ion chain and, depending on the kind of sideband, either remove or add a quantum of motion to the addressed oscillatory mode while simultaneously flipping the spin state (see Sec. 2.3 for further details). The faster these sideband transitions are performed, the higher is the exerted force and thus the speed of the gate operation.

2.1.1 Microwave control of trapped ions

Traditionally, two-qubit gates in trapped ions have predominantly been driven using lasers as they represent the only coherent radiation source whose free-space wavelength λ can exhibit the required field gradient over the ion's wavepacket size (typically nanometer scale) in order to exert a sufficient force on the ion system. A parameter which quantifies this relation is given by the dimensionless Lamb-Dicke parameter

$$\eta = \frac{2\pi q_j^0}{\lambda} \tag{2.1}$$

where $q_j^0 = \sqrt{\hbar/(2m\omega_j)}$ is the spatial extent of the ion's ground state wave function in the harmonic oscillator potential of the ion trap, ω_j is the secular frequency of that oscillator and m is the ion mass. In typical experiments, one tries to achieve $\eta \sim 0.1$ as this enables an effective spin-motion coupling

[1] Note that similar gate schemes have also been proposed by [SdMFZ99, MSJ00].

while still operating in the Lamb-Dicke regime for which $\eta^2 \ll 1$ is a necessary condition.

However, as multiple ion species considered for QIP have qubit transitions with excellent atomic properties in the microwave regime [LOJ+05], one might wonder why initially not microwaves instead of lasers (i.e. stimulated Raman processes) were used to apply the spin-dependent force. To understand this we consider e.g. the frequently used $^9Be^+$ ion which, depending on the externally applied magnetic field, has multiple suitable qubit transitions around 1 GHz (corresponds to $\lambda \sim 30\,\mathrm{cm}$). Confined in a harmonic oscillator potential with a secular frequency of 6 MHz, the corresponding wave packet size of the ion is about 10 nm, resulting in a negligible Lamb-Dicke parameter of about $\eta = 2 \times 10^{-7}$ and hence unpractically long two-qubit gate operations.

Over the years two approaches to overcome the low Lamb-Dicke parameter of free-space microwave radiation have been developed. The first one is the so-called 'MAGIC approach' which has been proposed in [MW01] and was first demonstrated in [JBT+09, KPS+12]. It relies on a static magnetic field gradient along the ion chain in order to induce a spin-motion coupling via global microwave radiation fields.

The other one, and this is the chosen technique within this thesis, is the microwave near-field approach [OLA+08] in which the ions are confined in the near-field regime of microwave conductors embedded in surface-electrode ion traps. Here, the achievable spatial variation of the fields is no longer determined by the free-space wavelength but rather by the ion-to-conductor distance as well as the chosen shape of microwave conductor, thus making spin-motion couplings with oscillating near-field gradients feasible. Since the first successful entangling gate for two $^{25}Mg^+$ ions with near-field microwaves [OWC+11], multiple milestones of the approach such as individual ion addressing for single-qubit operations [WOC+13b, CLH+14, CLS+17] or a high-fidelity entangling gate with an error in the 10^{-3} regime have been demonstrated [HSA+16].

Compared to laser-driven quantum logic operations, the microwave near-field approach offers several advantages: (1) the frequency, phase and amplitude of microwaves are naturally better to control than in the optical frequency regime lasers are typically operating at; (2) suitable microwave setups can be constructed from 'off-the-shelf' microwave components which dramatically reduces the overhead compared to expensive, complex and bulky laser systems; (3) when operating on qubit transitions in the electronic ground state, the near-field method avoids the inherent error source of laser-driven gates given

by photon scattering [OIB+07] and hence might ultimately achieve higher operation fidelities.

However, there are also downsides when working with near-field microwaves which need to be considered. First of all, the achievable gradient approximately scales as d^{-2} with the nearest ion-to-electrode distance d which, besides uncontrollable charging effects of exposed dielectrics from UV laser beams during photoionization or Doppler cooling, makes especially motional ion heating (scales about $\propto d^{-4}$) a non-negligible error contribution in two-qubit gate operations. While the heating process can in principle be alleviated by surface-cleaning methods [AGH+11, HCW+12, DGB+14] or cryogenic temperature [LGL+08, CS14], both countermeasures do still add complexity to the experimental setup. Furthermore, the produced microwave field pattern can, in contrast to tightly focused laser beams, not so easily be localized to an area closely around the ions, potentially causing unwanted cross-talk between the selected ion(s) for the operation and ions in other trap sites when scaling up to larger arrays. Here, solutions such as nulling the disturbing residual fields at the corresponding ion positions exist [CLS+17], but are again only achievable at the cost of additional experimental complexity. Finally, for the simplest geometry of a straight conductor, the gradient at the ion position is naturally accompanied by a residual magnetic field which, depending on the chosen qubit and the residual field polarization, can induce gate error contributions due to fluctuating AC Zeeman shifts or off-resonant excitations. Hence, more complex conductor geometries that minimize the residual field while maintaining the gradient at the ion position can be favorable, thus requiring sophisticated simulations in order to reliably predict the resulting field distribution.

2.1.2 Advanced conductor geometry

In the first demonstration experiment [OWC+11], the desired oscillating near-field gradient and low residual magnetic field at the ion position were achieved by using three independent microwave conductors whose relative phases and amplitudes were carefully adjusted. Although this conductor configuration has certain advantages such as its tunability or the possibility to entirely cancel residual fields, it is technically challenging to maintain the relative phase and amplitude stability between the three conductors as needed for high-fidelity gate operations. In the work of ref. [OWC+11] this was suspected to be one of the main issues limiting the fidelity of the performed two-qubit Mølmer-

Sørensen gate to $76 \pm 3\,\%$.

In our experiment, we desire to build up on this conclusion and develop a single microwave conductor geometry which, besides maintaining the previously mentioned field properties at the ion position, offers intrinsic phase and amplitude stability "by design". As has been shown in previous work [CKDO14, WHZ+17], a meander-like conductor can fulfill these requirements as long as the local field minimum of the resulting magnetic quadrupole is reasonably overlapped with the RF null position where the ions are trapped. In practice, however, such an overlap is difficult to achieve as a complex interplay of high frequency effects like the skin-effect, eddy currents and cross-couplings to other conductors have to be considered. In our group this is accomplished by performing full-wave finite element simulations in which almost the full chip design is parameterized and all electrodes as well as a part of the surrounding periphery (i.e. the filterboard as discussed in later sections) are taken into account[2]. The final conductor design then emerges from an optimization procedure including numerous parametric sweeps. For a previously operated ion trap, this procedure has led to a trap layout whose central region and simulated near-field pattern is illustrated in Fig. 2.1.

2.2 Methods of normal modes

As already mentioned in the introduction, ions can be confined in the center of an ion trap by superimposing oscillating and static electric fields. For instance, in the surface-electrode ion trap whose central electrode layout is depicted in Fig. 2.1, radial ion confinement in the $\hat{x}\hat{z}$-plane is achieved by applying an oscillating voltage to the RF electrode while axial confinement along the $\hat{y}$-axis is established by applying an appropriate set of DC voltages to the DC electrodes. In case of a weaker confinement in the axial than in the radial direction, N identical ions of mass m align along the trap axis whereas the individual ion positions represent the equilibrium at which the restoring force from the external potential exactly compensates the Coulomb repulsion between the ions. Here, the residual oscillatory motion of the ions along the three principle axes of the pseudopotential $\{\boldsymbol{q}_1, \boldsymbol{q}_2, \boldsymbol{q}_3\}$ can best be described by the method of normal modes whose eigenvectors form a complete orthogonal set. In this

[2]The simulation model is based on the FEM software Ansys HFSS 17.2 and is described in ref. [Wah16]. Within this work, all simulations have been performed by Martina Wahnschaffe and/or Giorgio Zarantonello as indicated in the trap chapters.

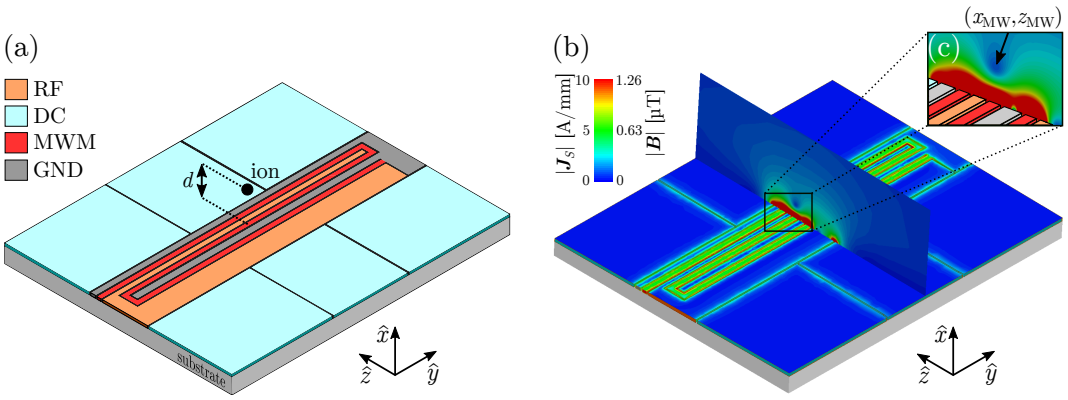

Figure 2.1: Central electrode layout of a former surface-electrode ion trap operated in the group. The trap axis is along the $\hat{y}$-axis. (a) The RF and DC electrodes confine the ion at a distance d above the surface while the meander-like microwave conductor (MWM) is used to produce the desired near-field pattern to induce spin-dependent forces. (b) Simulated surface-current distribution $|\boldsymbol{J}_S|$ and residual magnetic field $|\boldsymbol{B}|$ in the radial $\hat{x}\hat{z}$-plane when the MWM conductor is excited with 1 W at a frequency of about 1 GHz. Ideally, the local minimum $(x_{\mathrm{MW}}, z_{\mathrm{MW}})$ of the resulting near-field field (c) is overlapped with the ion position at the RF minimum.

coordinate representation, a displacement $\delta\boldsymbol{r}_n$ of ion n from the equilibrium position along one principal axis $\boldsymbol{q} \in \{\boldsymbol{q}_1, \boldsymbol{q}_2, \boldsymbol{q}_3\}$ is given by [Jam98b]

$$\delta\boldsymbol{r}_n = \boldsymbol{q} \sum_{j=1}^{N} b_j^n \, q_j^0 (a_j + a_j^\dagger) \tag{2.2}$$

where $q_j^0 = \sqrt{\hbar/(2m\omega_j)}$ denotes the ground state wavepacket size of the quantized motion in normal mode j and a_j ($a_j^\dagger$) the corresponding annihilation (creation) operator. Further, b_j^n is the amplitude for the jth normal mode of ion n along the respective principal axis.

In the simplest case of a single trapped ion (i.e. $N = 1$), the mode spectrum is composed of only three normal modes all of which describe the translation along one of the three principal axes. In the following, these modes are referred to as single-ion center-of-mass (COM) modes and have a mode amplitude equal to one. For $N = 2$, however, the mode spectrum becomes more complex and increases to two modes along each principal axis. Besides the collective translation of the ions along one principle axis in phase (which is referred to as the two-ion COM mode), there is also another normal mode describing the out-of-phase motion of the ions. Depending on whether the considered principle axis is along the axial or one of the radial directions, this kind of

normal mode is also referred to as breathing or rocking mode, respectively. The amplitudes of two-ion rocking modes are $b_j^n \to b_{\text{rock}}^1 = 1/\sqrt{2}$ for the first and $b_{\text{rock}}^2 = -1/\sqrt{2}$ for the second ion.

2.3 Spin-motion coupling using microwaves

This section briefly derives the interaction Hamiltonian of a single trapped ion interacting with an oscillating magnetic field in order to identify relevant transitions for experiments presented later in the thesis. The treatment follows ref. [Osp16, OLA+08] and is restricted to a single-ion COM mode aligned along the $\hat{x}$-axis as well as a fictional electronic two-level system whose states have an energy splitting of $\Delta E = \hbar\omega_0$. Subsequently, the states of the two-level system will be labeled $|\uparrow\rangle$ and $|\downarrow\rangle$ while the quantization field is aligned along the $\hat{z}$-axis.

When interacting with an oscillating magnetic field, the total Hamiltonian of the system can be written as

$$\begin{aligned} H &= H_0 + H_i \\ &= H_e + H_m + H_i \end{aligned} \tag{2.3}$$

where $H_e = \hbar\omega_0\sigma_z/2$ is the Hamiltonian for the two-level system with the Pauli matrix σ_z and $H_m = \hbar\omega_x a_x^\dagger a_x$ the motional Hamiltonian of a quantum harmonic oscillator of frequency ω_x whose creation and annihilation operators are given by $a_x^\dagger$ and a_x, respectively. Note that here we have dropped the ground state energy term of H_m for simplicity. In general, the interaction of an atom with an oscillating magnetic field

$$\boldsymbol{B}(t) = (\boldsymbol{e}_x B_x + \boldsymbol{e}_y B_y + \boldsymbol{e}_z B_z)\cos(\omega t + \varphi) \tag{2.4}$$

is given by the Hamiltonian

$$H_i = -\boldsymbol{\mu}\cdot\boldsymbol{B} \tag{2.5}$$

where $\boldsymbol{\mu}$ is the total magnetic moment of the atom. As we consider the effect of this Hamiltonian on the two-level system, relevant matrix elements only occur between states $(\uparrow, \downarrow)$ where the difference Δm of the quantum number m of the total z projection of the atom's angular momentum is either 0 or ± 1. In the following, we consider these two states separately. In the first case of $\Delta m = 0$, we find

$$H_i = -\left(\mu_\parallel\sigma_x + \mu_z\sigma_z + \mu_{id}\mathbf{1}\right) B_z\cos(\omega t + \varphi) \tag{2.6}$$

where **1** is the 2-by-2 identity matrix. Here, the first term describes resonant transitions between the states $(\uparrow, \downarrow)$ where the projection of the oscillating field on the quantization axis is the relevant field quantity (i.e. the π polarized field component). The second term results from a difference in magnetic moment between the two qubit states and represents an energy shift which is opposite in sign for both qubit states. The third term represents a common mode shift of both energy levels which is irrelevant for the dynamics of the system. For the second case, where $\Delta m = \pm 1$, we find

$$H_i = -\left(\mu_\perp \left(B_x \sigma_x + B_y \sigma_y\right) + \mu_z B_z \sigma_z + \mu_{id} B_z \mathbf{1}\right) \cos\left(\omega t + \varphi\right) \ . \tag{2.7}$$

Note that this time the term responsible for resonant transitions (first term) is caused by field components of the driving field which are perpendicular to the quantization axis (i.e. superpositions of σ_+- and σ_--polarization) while the remaining two terms represent an analog behavior as discussed in the previous case.

In general, these terms can be used for the following quantum logic operations. On the one hand, the terms proportional to σ_x and σ_y can drive resonant spin-flip transitions, but can also be used to implement motional sideband transitions, the key requirement for the Mølmer-Sørensen interaction, as long as an additional spatial variation of the oscillating field's amplitude occurs. On the other hand, the terms proportional to σ_z can in principle be used to implement a geometric phase gate along the lines of [LDM+03] which, however, is only possible for field-dependent qubit transitions as otherwise μ_z vanishes. In a typical scenario, we will consider one of the two state scenarios and apply the rotating wave approximation such that only one of the terms will be left over. Note that in the NIST experiments of [OWC+11] and in the present work, the $\Delta m = 0$ case was used, whereas the microwave experiment at Oxford initially used the $\Delta m = \pm 1$ scenario [AHB+13, HSA+16]. From now on, we will focus on $\Delta m = 0$ and write the magnetic field interaction as

$$H_i = -\mu \sigma_x B \cos\left(\omega t + \varphi\right) \tag{2.8}$$

where we have defined $\mu = \mu_\parallel$ and $B = B_z$.

We now consider the situation where the magnetic field amplitude B becomes a function of position. We assume the magnetic field amplitude to vary along the x-direction and obtain the Hamiltonian

$$H_i = -\mu \sigma_x \cdot B(x) \cos(\omega t + \varphi) \ . \tag{2.9}$$

Expanding the magnetic field around the ion's position via a Taylor expansion and rewriting the position operator as $x = q_x^0(a_x + a_x^\dagger)$ yields

$$H_i = \hbar \cos(\omega t + \varphi) \cdot (\sigma_+ + \sigma_-) \sum_k \frac{\Omega_k}{k!} (a_x + a_x^\dagger)^k \tag{2.10}$$

with the definition

$$\Omega_k = -\frac{\mu}{\hbar} \left. \frac{\partial^k B(x)}{\partial x^k} \right|_{x=0} (q_x^0)^k \ . \tag{2.11}$$

In order to transform the Hamiltonian into the interaction picture, we apply the unitary transformation $U^\dagger H_i U$ where $U = e^{-iH_0 t/\hbar}$. After a few lines of algebra[3] and using the relation $\cos(x) = (e^{ix} + e^{-ix})/2$ we obtain

$$\begin{aligned} H_I = & \frac{\hbar}{2} \left(e^{i(\omega t+\varphi)} + e^{-i(\omega t+\varphi)}\right) \left(\sigma_+ e^{i\omega_0 t} + \sigma_- e^{-i\omega_0 t}\right) \\ & \times \sum_k \frac{\Omega_k}{k!} \left(e^{-i\omega_x t} a_x + e^{i\omega_x t} a_x^\dagger\right)^k \ . \end{aligned} \tag{2.12}$$

Applying the rotating wave approximation which neglects fast oscillating terms of frequency $\pm(\omega + \omega_0)$ and only keeping the $k \in \{0, 1\}$ terms, the Hamiltonian transforms to

$$\begin{aligned} H_I = & \frac{\hbar}{2} \left(\sigma_+ e^{-i((\omega-\omega_0)t+\varphi)} + \sigma_- e^{i((\omega-\omega_0)t+\varphi)}\right) \\ & \times \left(\Omega_0 + \Omega_1 \left(e^{-i\omega_x t} a_x + e^{i\omega_x t} a_x^\dagger\right)\right) \end{aligned} \tag{2.13}$$

and has the following three resonances each of which describes an elementary coherent operation. The first one occurs when the frequency of the oscillating magnetic field is tuned to $\omega = \omega_0$. Here, the Hamiltonian simplifies to

$$H_{car} = \frac{\hbar}{2} \Omega_0 \left(\sigma_+ e^{-i\phi} + \sigma_- e^{i\phi}\right) \tag{2.14}$$

and drives Rabi oscillations with frequency Ω_0 between the states $|\uparrow\rangle$ and $|\downarrow\rangle$ without coupling to the ion's motional state. In the following this kind of transition is referred to as 'carrier transition'. The second operation appears when the field is tuned to $\omega = \omega_0 + \omega_x$. In this case, the Hamiltonian becomes

$$H_{bsb} = \frac{\hbar}{2} \Omega_1 \left(\sigma_- e^{i\phi} a_x + \sigma_+ e^{-i\phi} a_x^\dagger\right) \tag{2.15}$$

[3]The full math makes use of the Baker-Campbell-Haussdorff formula with additional commutator relations and is explicitly outlined in appendix A of reference [Wah16].

and drives so-called 'blue sideband' transitions in which both the electronic spin state and the motional Fock state $|n\rangle$ of the harmonic oscillator are changed. The introduced coupling is given by $|\downarrow\rangle|n\rangle \leftrightarrow |\uparrow\rangle|n+1\rangle$ whereas the frequency of the induced Rabi oscillations is $\sqrt{n+1}\,\Omega_1$. The third and last operation discussed, appears when the driving field's frequency is tuned to $\omega = \omega_0 - \omega_x$. Here, the Hamiltonian simplifies to

$$H_{rsb} = \frac{\hbar}{2}\Omega_1 \left(\sigma_+ e^{-i\phi} a_x + \sigma_- e^{i\phi} a_x^\dagger\right) \tag{2.16}$$

and drives Rabi oscillation between $|\downarrow\rangle|n\rangle \leftrightarrow |\uparrow\rangle|n-1\rangle$ with frequency $\sqrt{n}\,\Omega_1$. Subsequently, this coupling is referred to as 'red sideband' transition. Given these three operations which are depicted in Fig. 2.2, we can draw the following conclusions. On the one hand, we can introduce spin flip operations whose Rabi frequency Ω_0 is directly proportional to the applied oscillating magnetic field B as long as we chose the frequency to be in resonance with the transition ($\omega = \omega_0$). On the other hand, we can also manipulate the motional state of the ions by red and blue sideband transitions when tuning the frequency to $\omega = \omega_0 - \omega_x$ and $\omega = \omega_0 + \omega_x$, respectively. Here, in either case the resulting Rabi frequency is proportional to the gradient B' of the oscillating magnetic field (cf. Eq. 2.11). As we will see in the later sections, the carrier transitions are employed to prepare the ion in a specific hyperfine state of the electronic ground state while the sideband transitions can either be used to cool specific motional modes near the motional ground state or to implement an entangling quantum logic operation on two qubits.

2.4 Two-qubit gate theory

In the following we discuss the theoretical implementation of a two-qubit Mølmer-Sørensen gate which exerts a spin-dependent force on the ion system by means of a bichromatic radiation field whose components are slightly detuned from a blue and red sideband transition. We first derive the associated interaction Hamiltonian in the absence of errors and calculate an exact expression for its propagator. Finally, we investigate the propagator's influence on certain two-qubit states in different basis and show how the MS interaction can be employed to create entanglement.

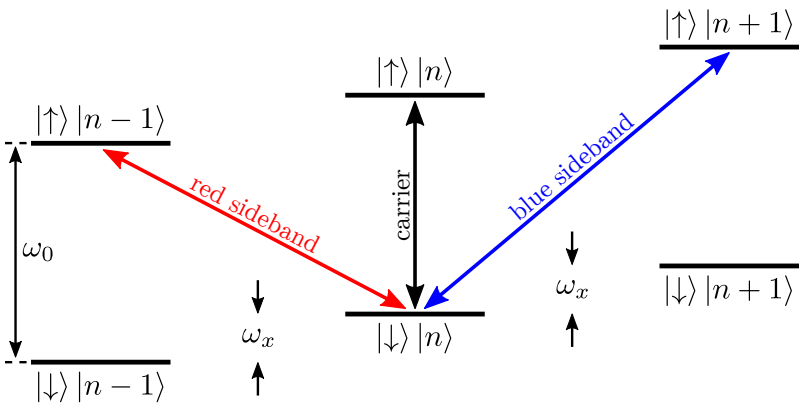

Figure 2.2: A two-level system coupled to a 1-dimensional harmonic oscillator along the $\hat{x}$-axis. The indicated transitions (carrier, blue sideband, red sideband) can be driven by either an oscillating magnetic field B or an oscillating magnetic field gradient B' at the ion position.

2.4.1 Interaction picture Hamiltonian

We now consider $N = 2$ ions which are aligned along the $\hat{y}$-axis and are exposed to an oscillating magnetic field gradient in the $\hat{x}\hat{z}$-plane of the form $\partial B_z/\partial x \cdot x = B' \cdot x$. Let further the interaction be restricted to a single two-ion mode j aligned along the $\hat{x}$-axis. Under these conditions, the Hamiltonian in the interaction picture in the rotating wave approximation (cf. Eq. 2.13) is given by

$$\begin{aligned} H_{MS} = \frac{\hbar}{2} \sum_{n=1}^{N} \tilde{\Omega}_j^n \left(\sigma_-^n e^{i((\omega-\omega_0)t+\varphi)} + \sigma_+^n e^{-i((\omega-\omega_0)t+\varphi)} \right) \\ \times \left(e^{-i\omega_j t} a_j + e^{i\omega_j t} a_j^\dagger \right) \end{aligned} \tag{2.17}$$

where we have defined the Rabi frequency for the coupling of ion n to mode j similar to the single-ion scenario as

$$\tilde{\Omega}_j^n = -\frac{\mu}{\hbar} B' b_j^n q_j^0 \ . \tag{2.18}$$

Let us now assume that the applied gradient has two frequency components detuned by a frequency δ from the motional mode j such that

$$\begin{aligned} \omega_b &= \omega_0 + (\omega_j + \delta) \\ \omega_r &= \omega_0 - (\omega_j + \delta) \ . \end{aligned} \tag{2.19}$$

When inserting both frequency components in Eq. 2.17, the expression becomes

$$\begin{aligned} H_{MS} = \frac{\hbar}{2}\sum_{n=1}^{N}\tilde{\Omega}_j^n\Big[&\sigma_-^n a_j e^{+i((\omega_b-\omega_0-\omega_j)t+\varphi_b)} + \sigma_+^n a_j^\dagger e^{-i((\omega_b-\omega_0-\omega_j)t+\varphi_b)} \\ &+\sigma_-^n a_j^\dagger e^{+i((\omega_r-\omega_0+\omega_j)t+\varphi_r)} + \sigma_+^n a_j e^{-i((\omega_r-\omega_0+\omega_j)t+\varphi_r)}\Big] \end{aligned} \tag{2.20}$$

where we introduce the notation

$$\begin{aligned} \varphi_s &= \frac{1}{2}(\varphi_b+\varphi_r) \\ \varphi_a &= \frac{1}{2}(\varphi_b-\varphi_r) \end{aligned} \tag{2.21}$$

for the phases of the two field components. In the following, Eq. 2.20 will also be referred to as the ideal Mølmer-Sørensen (MS) Hamiltonian. After using the definition of ω_b and ω_r, the Hamiltonian after the rotating wave approximation simplifies to

$$H_{MS} = \frac{\hbar}{2}\sum_{n=1}^{N}\tilde{\Omega}_j^n\left(e^{-i\varphi_s}\sigma_+^n + e^{+i\varphi_s}\sigma_-^n\right)\left(a_j e^{+i(\delta t+\varphi_a)} + a_j^\dagger e^{-i(\delta t+\varphi_a)}\right). \tag{2.22}$$

Here, the first bracketed term can be rewritten as

$$\begin{aligned} &\left(e^{-i\varphi_s}\sigma_+^n + e^{+i\varphi_s}\sigma_-^n\right) \\ =&\frac{1}{2}\left(\sigma_x^n\left(e^{-i\varphi_s}+e^{+i\varphi_s}\right) + i\sigma_y^n\left(e^{-i\varphi_s}-e^{+i\varphi_s}\right)\right) \\ =&\sigma_x^n\cos\varphi_s - \sigma_y^n\sin\varphi_s = \sigma_{\varphi_s}^n \end{aligned} \tag{2.23}$$

where $\sigma_{\varphi_s}^n$ is a Pauli matrix rotated by φ_s in the $\hat{x}\hat{y}$-plane. In case the resulting Rabi frequencies of the two field components are equal for both ions, which is assumed in our experiment, the MS Hamiltonian transforms to

$$H_{MS} = \frac{\hbar}{2}\Omega_g S_{\varphi_s}\left(a_j e^{+i(\delta t+\varphi_a)} + a_j^\dagger e^{-i(\delta t+\varphi_a)}\right) \tag{2.24}$$

where we have used the definitions:

$$\Omega_g = -\frac{\mu}{\hbar}B'\left|b_j^n\right|q_j^0 \tag{2.25}$$

$$S_{\varphi_s} = \sum_{n=1}^{N} sgn(b_j^n)\sigma_{\varphi_s}^n\ . \tag{2.26}$$

In the following, Ω_g is referred to as gate Rabi frequency which, as it is equal for both ions, is excluded from the sum. Further, S_{φ_s} is the collective spin operator.

2.4.2 Time evolution

In order to investigate the time evolution of an initial state $|\psi(t_0)\rangle$ at time t_0 when applying the MS interaction for a time $\Delta t = (t - t_0)$, we can calculate the propagator $\mathcal{U}(\Delta t)$ of the associated Hamiltonian and solve

$$\begin{aligned} |\psi(\Delta t)\rangle &= \mathcal{U}(\Delta t)\,|\psi(t_0)\rangle \\ &= e^{-\frac{i}{\hbar}H_{MS}\Delta t}\,|\psi(t_0)\rangle \ . \end{aligned} \tag{2.27}$$

With Eq. 2.24, the propagator becomes

$$\begin{aligned} \mathcal{U}(\Delta t) &= e^{\left[\dot{\gamma}(t_0)a_j^\dagger - \dot{\gamma}^*(t_0)a_j\right]\Delta t} \\ &= \mathcal{D}(\dot{\gamma}(t_0)\Delta t) \end{aligned} \tag{2.28}$$

where we have defined

$$\dot{\gamma}(t_0) = -i\left(\frac{\Omega_g S_{\varphi_s}}{2}\right) e^{-i(\delta t_0 + \varphi_a)} \tag{2.29}$$

and introduced the displacement operator $\mathcal{D}(\alpha) = e^{\alpha a_j^\dagger - \alpha^* a_j}$. The latter describes a state displacement in position-momentum phase space of magnitude α and has the useful property

$$\mathcal{D}(\alpha)\mathcal{D}(\beta) = \mathcal{D}(\alpha+\beta)e^{i\Im(\alpha\beta^*)} \tag{2.30}$$

which means that the effect of two consecutive displacements is additive up to a phase factor. To derive an analytic solution of the exact MS propagator $\mathcal{U}(t)$ we now divide the time into M intervals of length $\Delta\tilde{t} = t/M$ and concatenate the corresponding propagators such that

$$\begin{aligned} \mathcal{U}(t) &\approx \mathcal{U}(\tilde{t}_M)\cdot\mathcal{U}(\tilde{t}_{M-1})\cdot\ldots\cdot\mathcal{U}(\tilde{t}_1) \\ &\approx \mathcal{D}(\dot{\gamma}(\tilde{t}_{M-1})\Delta\tilde{t})\cdot\mathcal{D}(\dot{\gamma}(\tilde{t}_{M-2})\Delta\tilde{t})\cdot\ldots\cdot\mathcal{D}(\dot{\gamma}(\tilde{t}_0)\Delta\tilde{t}) \end{aligned} \tag{2.31}$$

where $\tilde{t}_j = j\cdot\Delta\tilde{t}$. When exploiting the above property of the displacement operator (Eq. 2.30) and in the limit of infinitesimal time steps (i.e. $\Delta\tilde{t}\to dt$), this expression can be transformed to[4]

$$\mathcal{U}(t) = \mathcal{D}(\gamma(t))\exp\left[-i\left(\frac{\Omega_g S_{\varphi_s}}{2\delta}\right)^2(t\delta - \sin(\delta t))\right] \tag{2.32}$$

where

$$\gamma(t) = -i\left(\frac{\Omega_g S_{\varphi_s}}{\delta}\right)e^{-i\varphi_a}e^{-i\frac{1}{2}\delta t}\sin\left(\frac{1}{2}\delta t\right) \ . \tag{2.33}$$

[4]See appendix A.3 for details on the calculation.

Finally, to get a better understanding of how the MS propagator acts on a two-qubit state, we rewrite Eq. 2.32 as

$$\mathcal{U}(t) = \mathcal{D}(S_{\varphi_s}\alpha(t))e^{-iS_{\varphi_s}^2\Phi(t)} \tag{2.34}$$

and define the motional displacement $\alpha(t)$ and the geometric phase $\Phi(t)$ as

$$\alpha(t) = -i\left(\frac{\Omega_g}{\delta}\right)e^{-i\varphi_a}e^{-i\frac{1}{2}\delta t}\sin\left(\frac{1}{2}\delta t\right) \tag{2.35}$$

$$\Phi(t) = \left(\frac{\Omega_g}{2\delta}\right)^2(t\delta - \sin(\delta t)) \ . \tag{2.36}$$

From this temporal evolution, it is apparent that the motional displacement induced by $\mathcal{D}$ depends on S_{φ_s} and hence, causes eigenstates of the collective spin operator with non-identical eigenvalues λ to perform different trajectories in phase space. Furthermore, while these trajectories are traversed, the eigenstates accumulate a geometric phase which, given by $\lambda^2\Phi(t)$, also depends on their respective eigenvalue. Finally, as the displacement operator term depends on both $\alpha(t)$ and S_{φ_s}, the spin and motional state are generally entangled while applying the MS interaction.

2.4.3 Implementation

Given the analytic solution of the propagator, we now investigate how the MS interaction can be used to implement a two-qubit entangling gate. To this end, we first consider the propagator's action on the eigenbasis of the collective spin operator which, for the example case of $\varphi_s = 0$, is spanned by

$$|\pm\rangle_1 \otimes |\pm\rangle_2 = \frac{|\uparrow\rangle_1 \pm |\downarrow\rangle_1}{\sqrt{2}} \otimes \frac{|\uparrow\rangle_2 \pm |\downarrow\rangle_2}{\sqrt{2}} \ . \tag{2.37}$$

In this basis, the traversed paths of the motional wavepacket in phase space have circular shape and periodically return to the initial state for an interaction time of

$$t = t_g = \frac{2\pi K}{\delta} \tag{2.38}$$

where $K \in \{1, 2, 3, ...\}$ indicates the number of performed loops. Consequently, the propagator in this condition simplifies to

$$\mathcal{U}(t_g) = \exp\left[-\frac{i\pi K\Omega_g^2}{2\delta^2}S_{\varphi_s}^2\right] \ . \tag{2.39}$$

Let us now assume that the mode j is the two-ion rocking mode for which the collective spin operator is

$$\begin{aligned} S_{\varphi_s} &= \sum_{n=1}^{N=2} sgn(b^n_{\text{rock}})\sigma^n_{\varphi_s} \\ &= \sigma^1_x - \sigma^2_x \ . \end{aligned} \tag{2.40}$$

and hence, the eigenvalues λ of the eigenstates $|\pm\pm\rangle$ and $|\pm\mp\rangle$ are given by $\lambda = 0$ and $\lambda = \pm 2$, respectively. In this case and under the additional requirement that

$$\delta = \delta_g = 2\Omega_g\sqrt{K} \tag{2.41}$$

the propagator performs the following operations on the four basis states

$$\begin{aligned} \mathcal{U}(t_g)\,|{+}{+}\rangle &= |{+}{+}\rangle \\ \mathcal{U}(t_g)\,|{+}{-}\rangle &= -i\,|{+}{-}\rangle \\ \mathcal{U}(t_g)\,|{-}{+}\rangle &= -i\,|{-}{+}\rangle \\ \mathcal{U}(t_g)\,|{-}{-}\rangle &= |{-}{-}\rangle \ . \end{aligned} \tag{2.42}$$

While this is a two-qubit phase gate in the $|\pm\rangle$ basis, the computational basis within this thesis is actually chosen to be the eigenstates $|\uparrow\rangle$, $|\downarrow\rangle$ of σ_z. Here, the action of the propagator is

$$\mathcal{U}(t_g)\,|{\uparrow}{\uparrow}\rangle = \frac{e^{-i\pi/4}}{\sqrt{2}}\left(|{\uparrow}{\uparrow}\rangle + i\,|{\downarrow}{\downarrow}\rangle\right) \tag{2.43}$$

$$\mathcal{U}(t_g)\,|{\uparrow}{\downarrow}\rangle = \frac{e^{-i\pi/4}}{\sqrt{2}}\left(|{\uparrow}{\downarrow}\rangle + i\,|{\downarrow}{\uparrow}\rangle\right) \tag{2.44}$$

$$\mathcal{U}(t_g)\,|{\downarrow}{\uparrow}\rangle = \frac{e^{i\pi/4}}{\sqrt{2}}\left(|{\uparrow}{\downarrow}\rangle - i\,|{\downarrow}{\uparrow}\rangle\right) \tag{2.45}$$

$$\mathcal{U}(t_g)\,|{\downarrow}{\downarrow}\rangle = \frac{e^{i\pi/4}}{\sqrt{2}}\left(|{\uparrow}{\uparrow}\rangle - i\,|{\downarrow}{\downarrow}\rangle\right) \ . \tag{2.46}$$

which means that, applied to the four states of the tensor product basis, the interaction generates maximally entangled states. In the following, we will focus only on Eq. 2.43 as it represents the state $|\Psi\rangle$ which we desire to prepare in the experiment.

As a final remark, we note that a higher number of phase loops K makes the gate more resilient against certain error sources such as motional heating [SM00]. However, as becomes apparent from Eq. 2.38 and 2.41, the required

interaction time t_g to prepare the desired state increases with $\sqrt{K}$ when keeping the gate Rabi frequency Ω_g fixed. Consequently, the overall microwave power which is dissipated in the trap also increases. In our gate implementation we limit the overall time of the gate drive to not exceed a conservatively chosen limit at a specific power level in order to avoid a possible damage of the trap (see Sec. 5.3 for further details). Given this boundary condition, we find the best results for $K = 3$ loops.

2.5 Gate analysis

In this section we present the employed tools to analyse the gate operation in respect to its capability to produce the aforementioned maximally entangled state. The first part is about the fidelity measurement while the second part discusses the numerical simulation model which is used to investigate the quantum dynamics of the system in the presence of certain error sources.

2.5.1 Fidelity analysis

We analyse the quality of our gate operation by performing a reduced tomography procedure in which we measure the preparation fidelity of the state the gate actually produces with respect to the ideal outcome given by the maximally entangled state $|\Psi\rangle$ defined in Eq. 2.43. For an arbitrary mixed state ρ, this fidelity is defined as [LDM+03]

$$\mathcal{F} \equiv \langle\Psi|\,\rho\,|\Psi\rangle = \frac{1}{2}\left(\rho_{\downarrow\downarrow,\downarrow\downarrow} + \rho_{\uparrow\uparrow,\uparrow\uparrow}\right) + |\rho_{\uparrow\uparrow,\downarrow\downarrow}| \tag{2.47}$$

where $\rho_{ii,jj} \equiv \langle ii|\,\rho\,|jj\rangle$ with $i, j \in \{\uparrow, \downarrow\}$ is the respective matrix element of the density matrix. To measure the needed quantities in the experiment, we can apply a $\pi/2$ analysis pulse on the qubit transition after the gate operation and observe the global ion fluorescence as a function of the analysis pulse's phase ϕ_a. After employing the full state detection outlined in Sec. 3.5, this measurement reveals oscillations of the population probabilities in $|\uparrow\uparrow\rangle$, $|\uparrow\downarrow\rangle$ and $|\downarrow\uparrow\rangle$, and $|\downarrow\downarrow\rangle$ given by $\mathrm{P}_{\uparrow\uparrow}$, $\mathrm{P}_{\uparrow\downarrow,\downarrow\uparrow}$ and $\mathrm{P}_{\downarrow\downarrow}$, respectively, enabling the determination of the first two matrix elements of Eq. 2.47 through the identification $\mathrm{P}_{\downarrow\downarrow} + \mathrm{P}_{\uparrow\uparrow} = \rho_{\downarrow\downarrow,\downarrow\downarrow} + \rho_{\uparrow\uparrow,\uparrow\uparrow}$. In order to determine the off-diagonal matrix element whose amplitude describes the coherence between $|\downarrow\downarrow\rangle$ and $|\uparrow\uparrow\rangle$, we require to calculate the parity

$$\Pi(\phi_a) = \mathrm{P}_{\downarrow\downarrow}(\phi_a) + \mathrm{P}_{\uparrow\uparrow}(\phi_a) - \mathrm{P}_{\uparrow\downarrow,\downarrow\uparrow}(\phi_a) \tag{2.48}$$

as a function of ϕ_a. Here, the amplitude $|A_\Pi|$ of the observed parity oscillation is equal to $|2\rho_{\uparrow\uparrow,\downarrow\downarrow}|$ [SKK+00].

A few comments about the employed fidelity analysis are in order. First, note that the reduced tomography procedure only measures the resulting state preparation fidelity of a single input state of the basis $\{|\uparrow\uparrow\rangle, |\uparrow\downarrow\rangle, |\downarrow\uparrow\rangle, |\downarrow\downarrow\rangle\}$ and hence is based on the assumption that the resulting error for all remaining input states is equal. While this is a common assumption in the field [SKK+00, LDM+03], the complete characterization of the gate operation actually requires full quantum process tomography [CN97, PCZ97] in which the resulting preparation fidelity for all four input states of the computational basis is measured to determine the mean gate fidelity [RKS+06]. However, as the procedure demands both single-ion addressing and single-ion read-out (cf. Eq. 2.44 - 2.45), its application is not straightforward in our setup and necessitates further implementations of experimental routines [WOC+13b] as well as modifications of the imaging setup.

Second, we are aware that, in order to investigate the two-qubit gate error in a computational scenario, randomized benchmarking would be a suitable choice [KLR+08, GMT+12]. However, as the method involves numerous randomized single-qubit operations on either of the two ions, single-qubit addressing is again required. Additionally, also the gate time on the order of $\sim 1\,\mathrm{ms}$ (cf. Sec. 5.3.1) might make longer gate sequences challenging as error contributions like motional heating and slow frequency drifts of the gate motional mode need to be addressed. Here, the former would require the implementation of sympathetic cooling using a second species [BDS+03, HHJ+09, JHA+09].

2.5.2 Numerical error analysis

In order to identify current limitations of our entangling gate operation, we numerically simulate the evolution of the system's density matrix ρ via a master equation in Lindblad form. This becomes necessary as incoherent error sources like qubit decoherence or motional heating may no longer be treated analytically. For our analysis, the simulations are done with QuTiP [noa16] and use a truncated Hilbert space for the motional mode including the first 25 oscillator levels. However, as all simulations have been performed by Marius Schulte in the group of Klemens Hammerer, they are only briefly discussed here for completeness.

The employed master equation is given by

$$\dot{\rho} = -i[H, \rho] + \mathcal{L}_h\rho + \mathcal{L}_d\rho\,. \tag{2.49}$$

where $H = \tilde{H}_{MS} + H_m + H_z + H_{spec}$ is the system Hamiltonian and $\mathcal{L}_k\rho$ with $k \in \{h, d\}$ are Lindblad terms [SM00]. The Hamiltonian describing the MS interaction is

$$\tilde{H}_{MS} = \frac{\hbar}{2}\sum_{n=1}^{N}(\Omega_B(t)\sigma_+^n a_j^\dagger e^{-i\delta t} + \Omega_R(t)\sigma_+^n a_j e^{i\delta t}) + \text{H.c.} \tag{2.50}$$

and represents an extension to the ideal one given in Eq. 2.20. Here, $N = 2$ denotes the number of ions, δ is the ideal gate detuning, $a_j^\dagger$ (a_j) is the creation (annihilation) operator of the HF rocking mode, we define $\sigma_\pm = (\sigma_x \pm i\sigma_y)/2$, and $\Omega_B(t)$ and $\Omega_R(t)$ are the Rabi frequencies of the bichromatic field components.

In order to translate an observed error into an infidelity, we include the parameter describing the noise in the corresponding term(s) of Eq. 2.49 and project the resulting density matrix onto the ideally prepared state $|\Psi\rangle$ (cf. Sec. 2.5.1) while assuming otherwise ideal gate parameters. Following this procedure, the current analysis considers the following error contributions.

2.5.2.1 Radial mode frequency instabilities

Frequency fluctuations of the HF rocking mode during the gate operation result in an effective change of the chosen gate detuning and hence leave the spin and motional state of the ions entangled at the end of the gate operation. As this leads to a reduced state preparation fidelity of the maximally entangled state, such mode fluctuations need to be considered in the analysis. In our simulations this is accomplished by including the term

$$H_m = \delta_\epsilon(t)a_j^\dagger a_j \tag{2.51}$$

in the system Hamiltonian where $\delta_\epsilon(t)$ represents the relative frequency deviation of the HF rocking mode with respect to its measured center frequency.

As we will see in Sec. 5.3.3.1, we observe two kinds of mode fluctuations in the experiment, both of which are treated differently in the simulations. The first one is a shot-to-shot fluctuation of the mode frequency which is characterized by a secular frequency measurement prior to gate operation. To translate this fluctuation into a gate error, we repeatedly pick out a random

mode frequency from amongst its measured standard deviation (i.e. the mode's FWHM) and average the resulting infidelities for 650 repetitions. The second kind of fluctuation is given by a linear frequency 'chirp' occurring during the gate pulse. Here, the frequency change of the HF rocking mode is modeled by a time-dependent frequency deviation $\delta_\epsilon(t)$ while assuming an otherwise non-varying mode frequency.

While the infidelity of both fluctuations is calculated independently in the simulations, we estimate their combined contribution to the gate error by determining the effective gate detuning for which the sum of both simulated infidelities is smallest. This is feasible as we optimize the gate detuning in the experiment to result in the highest gate fidelity.

2.5.2.2 Off-resonant couplings to spectator modes

Off-resonant driving of the gate operation on other motional modes can contribute an error as the performed loops in phase space of the other modes likely remain open due to vastly wrong chosen gate parameters. In the simulations, we take this error source into account by the term

$$H_{spec} = \frac{\hbar}{2}\Omega_{spec}\sum_{n=1}^{N}(\sigma_+^n + \sigma_-^n)(a_{spec}e^{i(\Delta\nu+\delta)t} + a_{spec}^\dagger e^{-i(\Delta\nu+\delta)t}) \tag{2.52}$$

where Ω_{spec} is the gate Rabi frequency of the chosen spectator mode and $\Delta\nu$ is its relative detuning from the HF rocking mode. As we will see in Sec. 5.3.3.2, we restrict ourselves in the current analysis to only the nearest motional mode (i.e. the LF rocking mode) as it contributes the largest error of this kind.

2.5.2.3 Motional heating

Due to an interaction of the ion with the environment, the motional state of the HF rocking mode can change during the gate operation and induce an error. Following [SM00], we include this incoherent error source in the master equation using a Lindblad term of the form

$$\mathcal{L}_h\rho = \gamma_h(\mathcal{D}[a_j]\rho + \mathcal{D}[a_j^\dagger]\rho) \tag{2.53}$$

where γ_h is the heating rate in phonons/s and we define $\mathcal{D}[\hat{O}]\rho = \hat{O}\rho\hat{O}^\dagger - \hat{O}^\dagger\hat{O}\rho/2 - \rho\hat{O}^\dagger\hat{O}/2$. Note that this is a redefinition of the symbol $\mathcal{D}$.

2.5.2.4 Qubit decoherence

Another non-unitary evolution of the system's density matrix is caused by decoherence of the qubit substates. In this case, the Lindblad term is given by [SM00]

$$\mathcal{L}_d\rho = \frac{\gamma_d}{2}\sum_{n=1}^{N}\mathcal{D}[\sigma_z^n]\rho \tag{2.54}$$

where γ_d is the decoherence rate and we use the same definition as in the Lindblad term of the motional heating $\mathcal{D}[\hat{O}]\rho = \hat{O}\rho\hat{O}^\dagger - \hat{O}^\dagger\hat{O}\rho/2 - \rho\hat{O}^\dagger\hat{O}/2$.

2.5.2.5 Differential AC Zeeman shift fluctuations

Residual fields of the bichromatic gate drive at the ion position can induce a differential AC Zeeman shift on the qubit transition and hence cause an asymmetric offset in the otherwise ideal detuning of the bichromatic field components with respect to the HF rocking mode. While such a shift will result in a wrong gate detuning and consequently lead to an additional error contribution, it can experimentally be compensated by adding a fixed detuning Δ_z to both sideband frequencies (cf. Eq. 5.11- 5.12). However, in practice this compensated shift still fluctuates between subsequent gate operations as e.g. the microwave power in the two sideband drives slightly varies. In the master equation, such a shift is taken into account by including the Hamiltonian

$$H_z = \frac{\Delta_\epsilon}{2}\sum_{n=1}^{N}\sigma_z^n \tag{2.55}$$

where Δ_ϵ denotes the uncompensated AC Zeeman shift. Following the same procedure as for the radial mode instabilities (cf. Sec. 2.5.2.1), we estimate the infidelity contribution due to shot-to-shot fluctuations of Δ_ϵ by randomly choosing a single shift from its measured standard deviation and taking the average of the resulting infidelities of 650 repetitions.

2.5.2.6 Microwave power instability and pulse shape

In order to estimate the gate error caused by Rabi frequency imbalances between the bichromatic field components, we set different values for Ω_B and Ω_R in Eq. 2.50. Besides this, the time-dependence of the Rabi rates is used to model the resulting error of the additional gate dynamics as induced by the envelope shaping of the microwave pulses with a 2 μs long error function at the beginning and end of the pulse (cf. Sec. 4.7.1). Here, we assume equal Rabi

frequencies for both sidebands (i.e. $\Omega_R = \Omega_B$) and include the accompanied variation of the AC Zeeman shift due to the shape of the pulse by adding the Hamiltonian $H_z = \Delta_\epsilon(t)/2 \sum_{n=1}^{N} \sigma_z^n$ with a time-dependent AC Zeeman shift $\Delta_\epsilon(t)$ to the master equation.

Chapter 3

$^{9}Be^{+}$ qubits

Numerous atomic ion species like $^{9}Be^{+}$, $^{25}Mg^{+}$, $^{40}Ca^{+}$, $^{43}Ca^{+}$ or $^{171}Yb^{+}$ are considered for quantum information processing and quantum simulation applications. As each element species has its characteristic atomic properties, all of them have individual advantages and technical challenges depending on the specific scope of the experiment. For the microwave near-field experiments carried out in this thesis, beryllium ions are a suitable choice for the following reasons. First of all, $^{9}Be^{+}$ is the lightest ion species currently considered and thus enables comparably high secular trap frequencies for a given electric field. In consequence, detrimental off-resonant carrier excitations during multi-qubit gates can be highly suppressed. Moreover, the qubit can be encoded in a first-order field-independent transition with $\Delta m_F = 0$, representing a key requirement in our experiment as the resulting microwave near-field pattern of the employed microwave conductor for the two-qubit is mainly linearly polarized. Here, the comparatively low qubit transition frequency also enables a relatively forgiving microwave design. Finally, the work functions of beryllium with 4.98 eV and gold with 5.1 eV are very similar which reduces the occurring patch potentials from deposited neutral atoms due to the ion loading procedure. In the following section, the atomic structure and employed qubit transition are introduced and the basic operations like state preparation, state manipulation and state detection are explained.

3.1 Atomic structure

Beryllium belongs to the group of alkaline earth metals with ^{9}Be being the only stable isotope. With two valence electrons in the neutral state, the electronic level structure becomes comparable to alkali metals once singly ionized to $^9Be^+$.

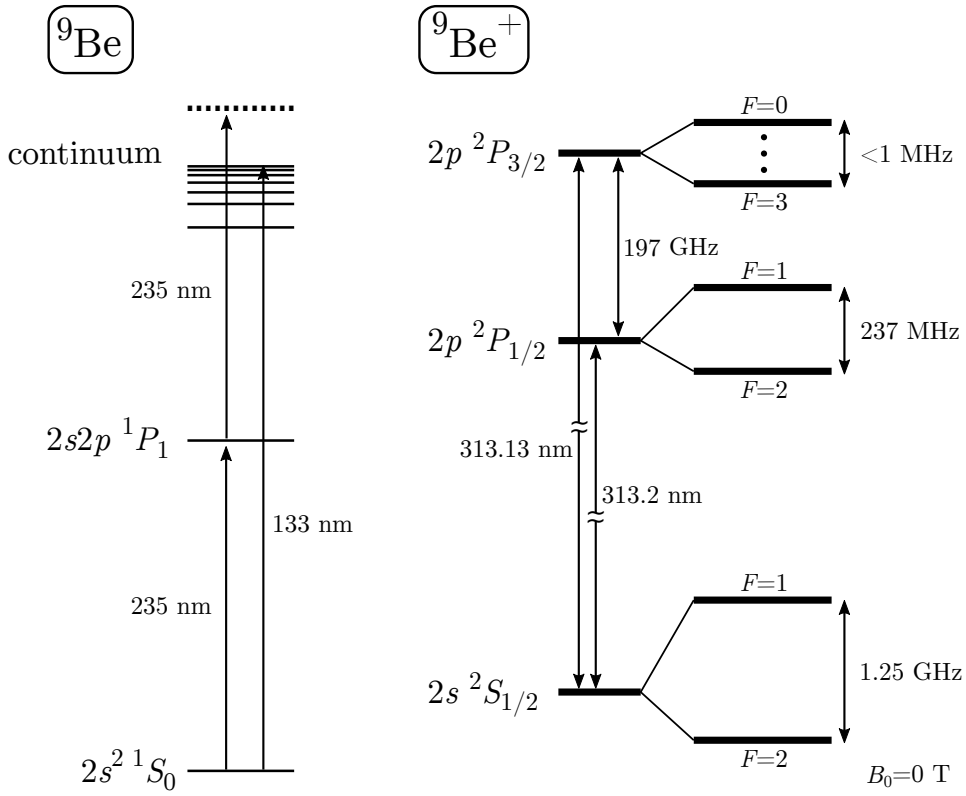

Figure 3.1: Left: Two-photon process used to photo-ionize neutral ^{9}Be. Right: Relevant level structure of $^9Be^+$ at zero magnetic field. Each hyperfine manifold is composed of $2F + 1$ degenerate sub-states.

As direct ionization requires photons of an inconvenient vacuum wavelength of $\simeq 133\,\text{nm}$, a resonant two-photon process with two $\simeq 235\,\text{nm}$ photons for ionization is used in this thesis [KM97]. As depicted on the left of Fig. 3.1, the first photon resonantly excites the electron from the $2s^2\ ^1S_{J=0}$ to the $2s2p\ ^1P_1$ energy level while the second photon gives the electron sufficient kinetic energy to permanently leave the atom's potential to the continuum. In the ionized state, the relevant energy levels are given by the electronic ground state $2s\ ^2S_{1/2}$ as well as the two lowest excited P states. Due to the fine structure splitting the exited states split into the $2p\ ^2P_{1/2}$ and $2p\ ^2P_{3/2}$ levels and

exhibit a frequency splitting of $\sim 197\,\mathrm{GHz}$ based on the values measured in ref. [BWWI85].

The nuclear spin of $^9Be^+$ ($I = \frac{3}{2}$) couples to the total angular momentum of the electrons and forms the hyperfine structure. As for the $^2S_{1/2}$ level, this results in the $F = 1$ and $F = 2$ manifolds which are split by $\sim 1.25\,\mathrm{GHz}$ at low magnetic fields [WBI83, Bla10]. Here, F with $F \in \{|I - J|, ..., I + J\}$ is the quantum number for the atom's total angular momentum $\boldsymbol{F} = \boldsymbol{I} + \boldsymbol{J}$ whereas I and J are the quantum numbers of the nuclear spin $\boldsymbol{I}$ and the total electrons angular momentum $\boldsymbol{J}$, respectively. The corresponding projections on the quantization axis are given by m_F, m_I and m_J. The hyperfine structure of the $^2P_{1/2}$ level extends to an energy range of about 237 MHz [BWWI85] while the hyperfine splitting of the $^2P_{3/2}$ level is below 1 MHz [PAS75]. As shown on the right of Fig. 3.1, the wavelength of a transition between the $^2S_{1/2}$ level and the P levels is in the ultraviolet spectrum around $\sim 313\,\mathrm{nm}$, requiring non-linear frequency conversion for laser light generation.

3.2 Hyperfine qubit

Applying an external magnetic field lifts the degeneracy of the magnetic sub-levels of the $^2S_{1/2}$ and both lower P manifolds due to the Zeeman effect. As has been shown in ref. [LOJ+05], there exist hyperfine transitions in $^2S_{1/2}$ which become to first-order magnetic field-independent at specific magnetic fields, and thus enable coherence times up to several seconds. In contrast to typical clock-transitions of the kind $|F, m_F = 0\rangle \leftrightarrow |F', m_{F'} = 0\rangle$ at zero magnetic field (as for example in $^{171}Yb^+$ [FSL+95]), the field-independent transitions at finite field have the additional advantage of breaking the degeneracy of the magnetic sub-states and giving rise to their spectral resolution during state manipulation. Consequently, these field-independent transitions have become a frequent choice for qubit implementations in QIP [OYM+07, BHL+16, NMM+18].

Fig. 3.2 shows the hyperfine energies of the $^2S_{1/2}$ sub-levels of $^9Be^+$ as a function of an applied external magnetic field up to $B = 25\,\mathrm{mT}$. While the first-order field-independent transitions within this field range are indicated by arrows, their relevant properties are listed in Tab. 3.1 As the produced near-field pattern of the microwave conductor employed for the gate operation is mainly π-polarized and thus requires a magnetic dipole transition with $\Delta m_F = 0$ to maximize the interaction strength, the qubit in this work is encoded on the transition $|2, 1\rangle \equiv |\downarrow\rangle \leftrightarrow |1, 1\rangle \equiv |\uparrow\rangle$ at $B_0 \simeq 22.3\,\mathrm{mT}$.

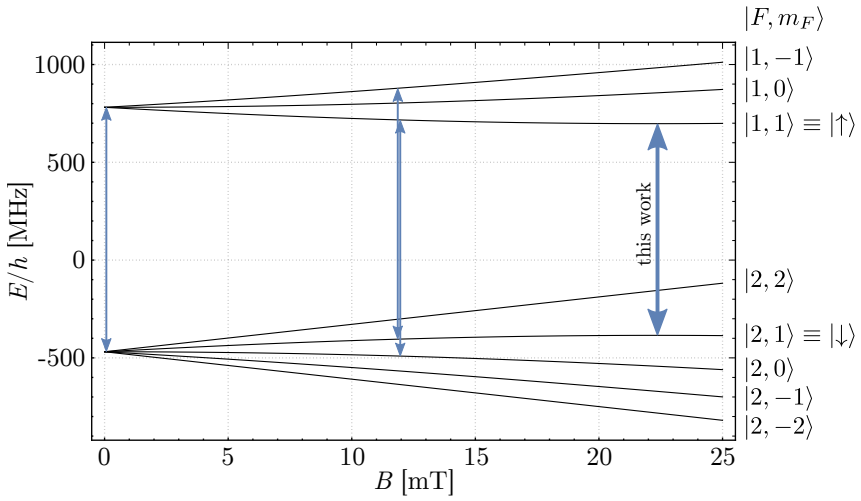

Figure 3.2: Energy shift of the magnetic sub-levels for the electronic ground state $^2S_{1/2}$ of $^9Be^+$ as a function of an external magnetic field B calculated using the Breit-Rabi formula [Lan06]. The arrows indicate transitions for which the linear energy shift vanishes.

3.3 State preparation

To prepare the ions in a well-defined state of the electronic ground state $^2S_{1/2}$ at $B_0 \simeq 22.3\,\mathrm{mT}$ and Doppler cool their motion prior to any experiment, we utilize two superimposed σ^+-polarized laser beams propagating parallel to the quantization axis and tuned near-resonant with the closed cycling transition $^2S_{1/2}\,|2,2\rangle \leftrightarrow {}^2P_{3/2}\left|m_J = \frac{3}{2}, m_I = \frac{3}{2}\right\rangle$ as shown in Fig. 3.3.

While one of the beams is about 10 MHz red detuned from the cycling transition and will be referred to as Blue Doppler (BD), the second beam is about 427 MHz red detuned from the BD and will be referred to as BD Detuned (BDD). The BDD operates at a power of $\sim 400\,\mu\mathrm{W}$ and is used to perform optical pumping of the electronic ground state population to the stretched state $^2S_{1/2}\,|2,2\rangle$ as well as Doppler pre-cooling of hot ions during the ion loading sequence or after thermal background gas collisions. On the other hand, the BD beam performs efficient Doppler cooling on the closed cycling transition only after the pre-cooling while its intensity is set around saturation intensity. The overall sequence to prepare Doppler cooled ions in $|2,2\rangle$ consists of a joint BD/BDD pulse for 10 ms[5] and a subsequent BD only pulse for $10\,\mu\mathrm{s}$.

[5]The purpose of this long pre-cooling time is to enforce a duty-cycle during high-power microwave experiments for which a thermal relaxation can safely be achieved. Hence, much shorter cooling times are also possible.

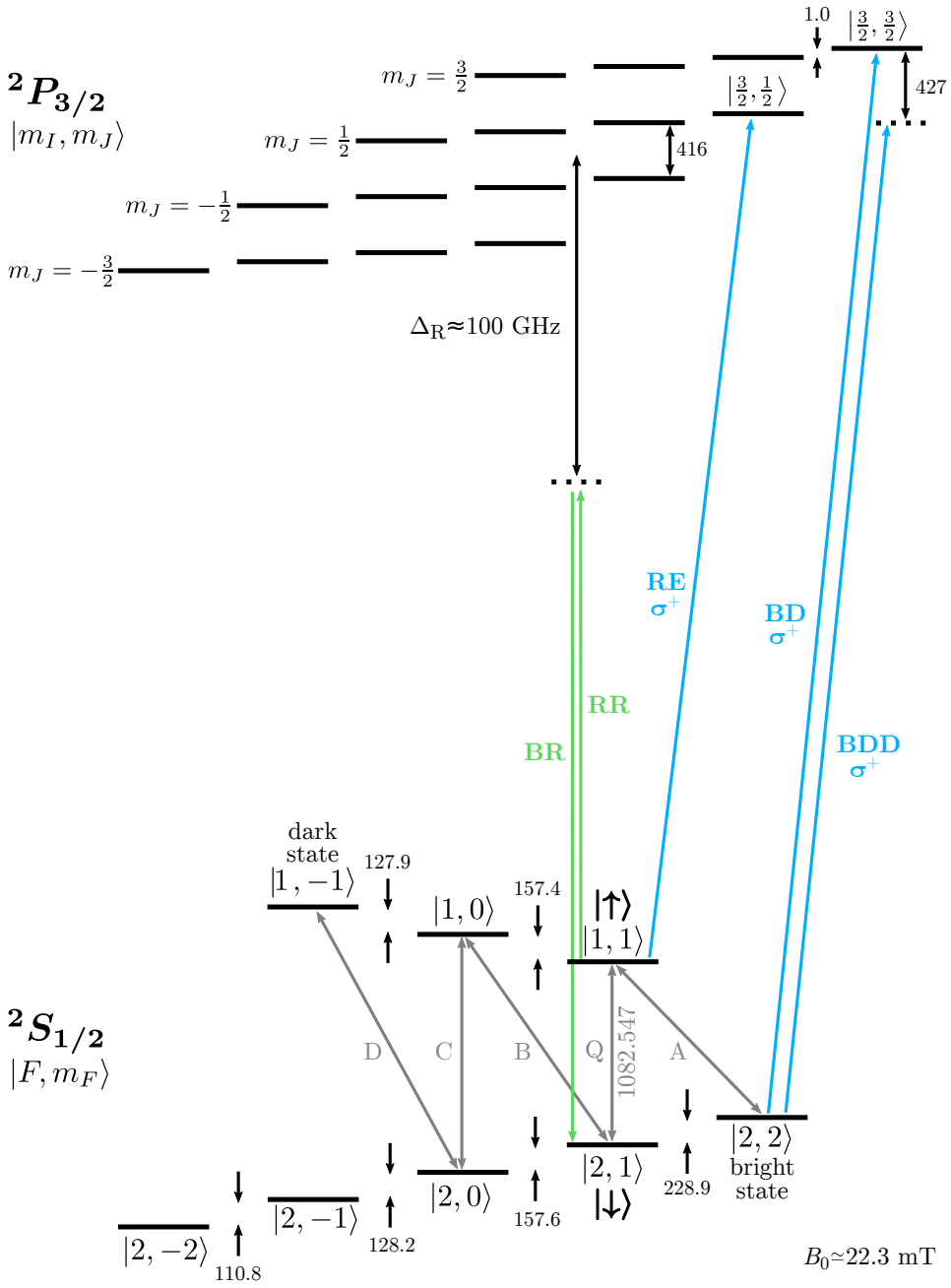

Figure 3.3: Relevant level scheme of $^9Be^+$ at $B_0 \simeq 22.3\,\mathrm{mT}$ (not to scale) including the first-order field-independent qubit transition $|2,1\rangle \equiv |\downarrow\rangle \leftrightarrow |1,1\rangle \equiv |\uparrow\rangle$. If not stated otherwise, all given numbers are in MHz. In the experiments, the hyperfine transitions labeled with capital letters (gray arrows) are addressed via microwave radiation while the colored transitions are driven by optical beams. BD: Doppler cooling and detection, BDD: optical pumping and pre-Doppler cooling of hot ions, BR/RR: Raman transitions for ground state cooling, RE: repumping during sideband cooling.

transition $\lvert F, m_F\rangle \leftrightarrow \lvert F', m_{F'}\rangle$	f_0 [MHz]	B_0 [mT]	$\partial^2 f_0/\partial B^2$ [Hz/μT^2]
$\lvert 2,1\rangle \leftrightarrow \lvert 1,-1\rangle$	1250.017	0.0254	0.2355
$\lvert 2,0\rangle \leftrightarrow \lvert 1,1\rangle$	1207.495	11.945	0.3049
$\lvert 2,1\rangle \leftrightarrow \lvert 1,0\rangle$	1207.352	11.964	0.3049
$\lvert 2,1\rangle \leftrightarrow \lvert 1,1\rangle$	1082.547	22.307	0.3626

Table 3.1: First-order field-independent transitions of the $^2S_{1/2}$ manifold up to an external magnetic field of 25 mT including the corresponding magnetic field B_0 and transition frequency f_0. The second-order field sensitivity of the transitions at the respective B_0 are listed in the right column [Lan06].

For further experimental details and Doppler cooling results see Sec. 5.2.1.

For some experiments like the two-qubit gate, the state preparation procedure is extended by an additional Raman sideband cooling sequence leaving the ion again in $|2,2\rangle$ but with selected motional modes cooled near the motional ground state. The necessary laser beams for Raman sideband cooling are shown in Fig. 3.3 and comprise two counter-propagating Raman beams (labeled RR and BR) as well as a repumping beam (labeled RE). The experimental results of the sideband cooling are presented in Sec. 5.2.2 and 5.2.4.

To initialize the qubit in $|\downarrow\rangle$ or $|\uparrow\rangle$ after optical pumping or state preparation, we subsequently apply microwave-induced π rotations on the transitions labeled A and Q as explained in Sec. 3.4.

3.4 Microwave state manipulation

Many experiments described in this thesis rely on the possibility to coherently prepare the ions in a specific state (or superposition) of the $^2S_{1/2}$ manifold. In our experiment, we use the oscillating magnetic field of an embedded microwave conductor (referred to as MWC_2) to drive the transitions indicated with gray arrows in Fig. 3.3. Here, the close proximity of the conductor to the ion position enables typical Rabi frequencies on the order of a few hundred kHz for an applied microwave power of ~ 250 mW. The Rabi frequencies used in the experiments differ between the two traps discussed in this thesis and hence are listed in separate columns in Tab. 3.2. For an example of a Rabi flopping experiment in the single-layer ion trap, see Fig. 3.4.

	transition $\lvert F, m_F\rangle \leftrightarrow \lvert F', m_{F'}\rangle$	f_0 [MHz]	$\Omega_{SL}/(2\pi)$ [kHz]	$\Omega_{ML}/(2\pi)$ [kHz]
A	$\lvert 2,2\rangle \leftrightarrow \lvert 1,1\rangle$	853.64	357	320
Q	$\lvert 2,1\rangle \leftrightarrow \lvert 1,1\rangle$	1082.55	252	211
B	$\lvert 2,0\rangle \leftrightarrow \lvert 1,1\rangle$	1240.19	290	240
C	$\lvert 2,1\rangle \leftrightarrow \lvert 1,0\rangle$	1239.92	182	143
D	$\lvert 2,0\rangle \leftrightarrow \lvert 1,0\rangle$	1397.56	177	120

Table 3.2: Hyperfine transitions of the $^2S_{1/2}$ manifold used for state manipulation via microwave radiation. The transition frequencies f_0 are given for an external magnetic field of 22.3 mT for which the qubit transition becomes first-order field-independent. The two columns on the right summarize the respective Rabi frequencies achieved in the single-layer ion trap (Ω_{SL}) and multi-layer ion trap (Ω_{ML}) for an applied microwave power of ~ 250 mW.

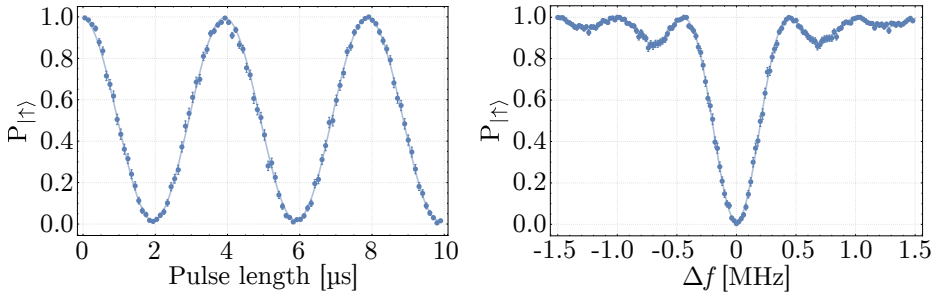

Figure 3.4: Left: Rabi oscillations on the qubit transition in the single-layer ion trap. The data was obtained by preparing the ion in $|\uparrow\rangle$, applying a resonant microwave pulse on the qubit transition and observing the population in $|\uparrow\rangle$ (cf. Sec. 3.5) as a function of the pulse length. The applied microwave power is about 250 mW. Right: Corresponding frequency scan of the microwave pulse around the qubit resonance. The pulse length ($\sim 2\,\mu s$) was matched to perform a π rotation on the qubit transition when on resonance.

3.5 State detection

To read out the qubit states after an experiment, we perform state-dependent fluorescence detection [NSD86, SNBT86, BHIW86] on the closed cycling transition ${}^2S_{1/2}\,|F=2, m_F=2\rangle \leftrightarrow {}^2P_{3/2}\,\left|m_J=\frac{3}{2}, m_I=\frac{3}{2}\right\rangle$ using the BD beam tuned to resonance at approximately saturation intensity. Prior to detection, we transfer all population in $|\uparrow\rangle$ to $|2,2\rangle$ and all population in $|\downarrow\rangle$ to $|1,-1\rangle$ by applying consecutive π rotations on transition A and $\{\mathrm{B},\mathrm{C},\mathrm{D}\}$, respectively. In the following, the $|2,2\rangle$ ($|1,-1\rangle$) state is also referred to as 'bright' ('dark') state; see Fig. 3.3 for an overview. An ion in the bright state scatters about 19.4 million photons per second, a fraction of which is collected using the imaging setup detailed in Sec. 4.6. For a detection interval of 400 μs and one ion prepared in the bright (dark) state, we detect on average around 23 (0.8) photon counts with the BD beam set to saturation intensity. Under the same conditions, the background scattering for an empty trap is about 0.5 photon counts.

As the collected photons from the bright state ideally follow Poisson statistics, we can infer the state population after an experiment by repeating it with the same parameters many times and fit the obtained measurement histogram to a weighted sum of Poisson distributions. For experiments with two ions, the sum consists of three Poisson distributions corresponding to 0-ion, 1-ion and 2-ions bright. The fit parameters are given by the statistical mean of each individual distribution and the mean photon counts for 0-ion and 1-ion bright (we assume the mean photon counts of the 2-ions bright distribution to be the double of the 1-ion bright distribution). Prior to the fitting, we fix the fit parameters of the mean photon counts of 0-ion and 1-ion bright using a reference Ramsey experiment in which we scan the phase of the second $\pi/2$ pulse and assume the outcome of the experiment as a function of the known phase to be perfect. Fig. 3.5 shows an example of a measurement histogram obtained during a Ramsey experiment with two ions. A fit of a sum of weighted distributions to the data (black dashed line in Fig. 3.5 (a)) reveals the probability for the individual population of 0-ion, 1-ion or 2-ions bright to be 37.5 %, 25 % and 37.5 %, respectively. The three Poisson distributions of the sum are highlighted in different colors in Fig. 3.5 (b).

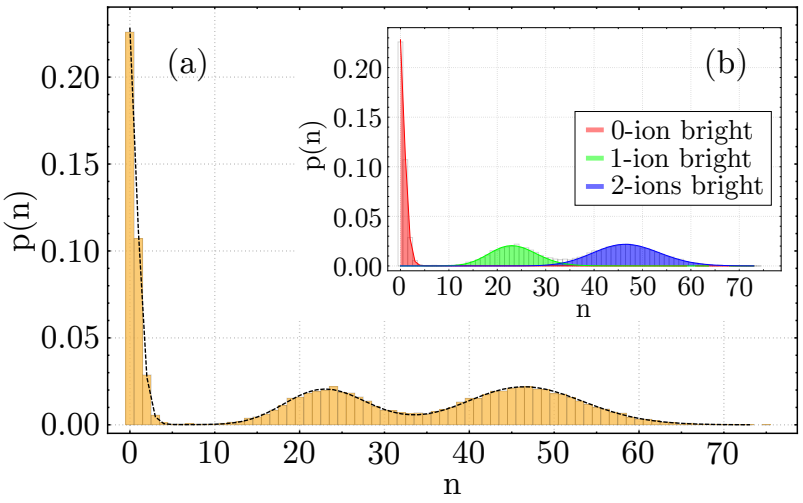

Figure 3.5: Typical measurement histogram of a two-ion experiment on the qubit transition. The data was obtained by summing individual histograms of $N = 30000$ experiments and normalizing the result by the total number of experiments N. (a) Fitting a sum of three Poisson distributions (back dashed line) to the data reveals the populations. (b) Color-coded Poisson distributions contributing to the sum of the associated population probabilities.

3.5.1 Depumping errors

For the two-qubit gate experiments (cf. Sec. 5.3), we extend the fitting procedure of the previous section to a sum of modified Poisson distributions in order to take optical depumping errors, which otherwise would diminish the qubit readout fidelity, into account. In general, two depumping errors can occur during the fluorescence detection of the bright state both of which are discussed in more detail in the following.

3.5.1.1 Bright to dark state leakage

On the one hand, the bright state can be optically pumped out of the closed cycling transition to a dark state due to a wrong polarization of the ideally σ^+-polarized BD beam. Following the selection rules, any π-component in the polarization of the BD beam could couple the bright state ($^2S_{1/2}\left|F=2,m_F=2\right\rangle \equiv {}^2S_{1/2}\left|m_J=\frac{1}{2},m_I=\frac{3}{2}\right\rangle$) to the $^2P_{3/2}\left|m_J=\frac{1}{2}\right\rangle$ manifold while, analogously, any σ^--component could couple the bright state to the $^2P_{3/2}\left|m_J=-\frac{1}{2}\right\rangle$ manifold. However, as the waveplates in the BD beam have been carefully optimized to generate purely σ^+-polarized light at the ion position and both depumping transitions are highly detuned from the closed cycling transition (417 MHz and

834 MHz, respectively), the error source of bright to dark state leakage will be neglected within this thesis.

3.5.1.2 Dark to bright state leakage

On the other hand, the dark state can also be optically pumped into the bright state due to off-resonant couplings to excited states undergoing at least three scattering events. Once in the bright state, the leaked population participates in the photon scattering on the closed cycling transition obeying Poisson statistics with a reduced mean given by

$$\lambda(t) = r_{bg}\gamma_c\tau_d + \gamma_c(\tau_d - t) \tag{3.1}$$

where τ_d is the detection interval, r_{bg} is the rate of background collected photons normalized to γ_c, $\gamma_c = \eta\frac{\gamma}{2}\frac{s_0}{1+s_0}$ is the rate of collected photons from the closed cycling transition, η is the total photon collection efficiency of the imaging setup, s_0 is the on-resonance saturation parameter and t defines the time at which the dark ion enters the bright state. As this depumping error contributes in a non-negligible way to the qubit readout fidelity with our experimental parameters, it is considered in our analysis of the gate experiments.

Following the approach detailed in [Lan06], the time evolution of the probability of the electron to be in the bright state can generally be calculated by solving rate equations including all hyperfine levels of the $S_{1/2}$ manifold and their respective couplings to the two excited P manifolds as briefly explained below. For a more general treatment considering also non-perfectly σ^+-polarized light, see [Lo15].

May $\mathbf{v}$ be an 8-dimensional vector whose entries represent the population of the 8 hyperfine states in the electronic ground state $^2S_{1/2}$ and $\mathbf{\Gamma}$ a matrix whose elements Γ_{ij} are the optical pumping rates from state $|j\rangle \rightarrow |i\rangle$ assuming a pure σ^+-polarization of the BD beam. The non-zero matrix elements Γ_{ij} can be calculated using the Kramers-Heisenberg formula [OLJ+05]:

$$\Gamma_{ij} = \frac{\gamma^3 s_0}{8}\sum_q \left|\sum_k \frac{b_{ij}^{(k,q)}}{\Delta_k + \beta}\right|^2 \tag{3.2}$$

where γ is the detection transition linewidth, $s_0 = I/I_s$ is the saturation parameter, I is the laser intensity, and $b_{ij}^{(k,q)} = \langle i|\mathbf{d}\cdot\sigma^q|k\rangle\langle k|\mathbf{d}\cdot\sigma^+|j\rangle/\mu^2$ is the amplitude of the coupling from $|j\rangle \rightarrow |i\rangle$ through the intermediate excited state $|k\rangle$ normalized to the magnitude of the cycling transition electric

dipole moment $\mu = \left|\left\langle P_{3/2}, F' = 3, m'_F = 3 \left| \mathbf{d} \cdot \sigma^+ \right| S_{1/2}, F = 2, m_F = 2 \right\rangle\right|$. Furthermore, $\mathbf{d}$ is the electric dipole moment, Δ_k the detuning of the detection beam from the $|j\rangle \leftrightarrow |k\rangle$ transition and $\beta = i\,\gamma\frac{\sqrt{1+s_0}}{2}$ is a radiative damping term to produce the saturated scattering rate. The sum over k extends over all excited states in the $P_{1/2}$ and $P_{3/2}$ manifold while the sum over q is over all three possible polarizations of the scattered photons. In contrast to [OLJ+05], the latter has been excluded from the absolute square as it is in principle possible to measure the polarization of the scattered photons. Given an expression for Γ_{ij}, the rate of population transfer of each state is given by

$$\frac{\partial v_i}{\partial t} = \sum_j \Gamma_{ij} v_j - v_i \sum_j \Gamma_{ji} \ . \tag{3.3}$$

Rewriting Eq. 3.3 in matrix notation yields:

$$\frac{\partial \mathbf{v}}{\partial t} = \mathbf{M} \cdot \mathbf{v} \tag{3.4}$$

where $\mathbf{M} = \mathbf{\Gamma} - \mathbf{D}(\mathbf{1^T} \cdot \mathbf{\Gamma})$, $\mathbf{1}$ is an 8-by-1 matrix of ones, and $\mathbf{D(x)}$ is a diagonal matrix whose elements are given by the elements of the vector $\mathbf{x}$. Following [Lan06], the linear system of differential equations in Eq. 3.3 has time-dependent solutions for the population of each state of the form

$$v_{ij}(t) = \sum_{m=1}^{8} a_{ij}^{(m)} e^{-\omega_m t} \tag{3.5}$$

where m runs over all hyperfine levels of the $S_{1/2}$ manifold and $a_{ij}^{(m)}$ and ω_m are factors of the solution which dependent on the matrix $\mathbf{M}$ as well as the initial condition represented by j. As we are only concerned with the probability of detecting the ion in the bright state at time t with the ion initially prepared in another hyperfine state $|j\rangle$ at $t = 0$, Eq. 3.5 evaluates to

$$P_{j\to|2,2\rangle}(t) = v_{i=|2,2\rangle j}(t) = 1 - \sum_{m=1}^{7} a_{i=|2,2\rangle j}^{(m)} e^{-\omega_m t} \quad . \tag{3.6}$$

Using Eq. 3.6 we can plot the probability of the ion to be optically pumped into the bright state as a function of the detection interval for different initial states. As shown in Fig. 3.6, the state $|1,-1\rangle$ has the smallest probability due to its highest detuning of 1139 MHz from the closed cycling transition. Consequently, we use this state as a shelved dark state for the population in $|\downarrow\rangle$ prior to the detection.

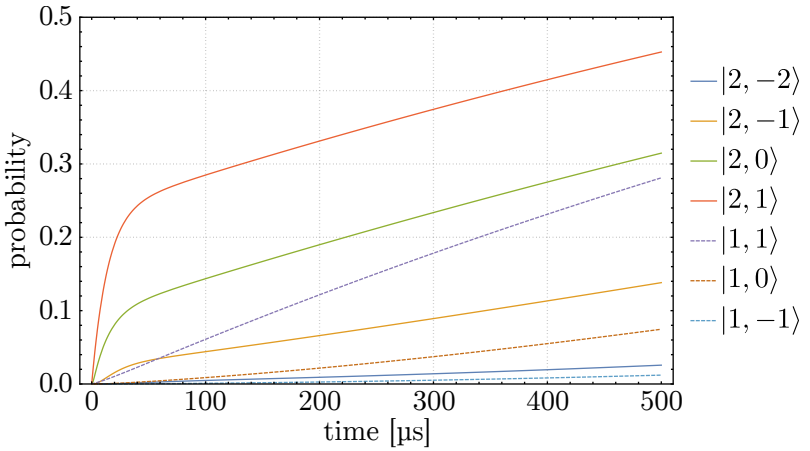

Figure 3.6: Simulation of the probability of the electron to be optically pumped into the bright state $|2,2\rangle$ at time t during the detection interval given the different initial hyperfine states of the $S_{1/2}$ manifold on the right. In the experiment we use a detection interval of $\tau_d = 400\,\mu$s.

In order to consider the dark state $\rightarrow$ bright state leakage during the detection interval in the fitting procedure of the populations and thus improve our qubit readout fidelity, the distribution of photon counts for an ion in the dark state needs to be studied. Based on Eq. 3.6 this leakage probability is given by the sum over exponential terms, resulting in the probability distribution of collected photons for an ion prepared in the dark state to be represented by a convolution of Poisson and exponential distributions [Kin99]. Following the analysis by Acton *et al.* [ABH$^+$05] and C. Langer [Lan06], the probability of detecting n photons for an ion prepared in the dark state can be calculated by

$$\begin{aligned} p(n|j) = \sum_m a^{(m)}_{i=|2,2\rangle j} e^{-\omega_m \tau_d} \Bigg[P(n|r_{bg}\gamma_c\tau_d) + \frac{\omega_m \gamma_c^n e^{-\omega_m \tau_d r_{bg}}}{(\gamma_c - \omega_m)^{n+1}} \\ \times \Big\{ \mathcal{P}(n+1, (\gamma_c - \omega_m)(1+r_{bg})\tau_d) \\ - \mathcal{P}(n+1, (\gamma_c - \omega_m) r_{bg} \tau_d) \Big\} \Bigg] \end{aligned} \tag{3.7}$$

where τ_d is the detection interval, $P(n|\lambda) = \frac{e^{-\lambda}\lambda^n}{n!}$ is a Poisson distribution giving the probability of detecting n photons with mean λ, $\gamma_c = \eta_c \frac{\gamma}{2} \frac{s_0}{1+s_0}$ is the rate of collected photons from the closed cycling transition (with η_c being the total photon collection efficiency of the imaging setup), r_{bg} is the rate of background collected photons normalized to γ_c and $\mathcal{P}(a,x) \equiv \frac{1}{(a-1)!}\int_0^x e^{-y} y^{a-1} dy$ is the incomplete Gamma function normalized such that $\mathcal{P}(a,\infty) = 1$.

Using Eq. 3.7 in combination with our detection time and saturation pa-

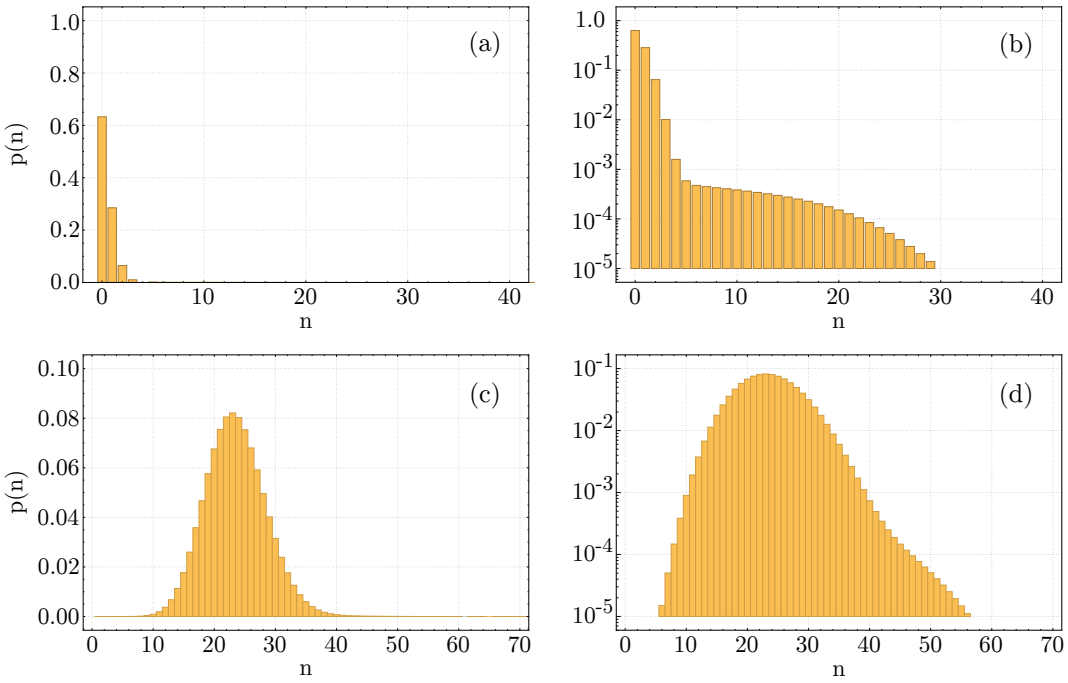

Figure 3.7: Calculated histograms for 0-ion bright (upper row) and 1-ion bright (lower row) including optical depumping from the dark state into the bright state for a detection interval of $\tau_d = 400\,\mu$s and the BD beam set to saturation intensity. The left column shows the histograms on a linear scale while the right column shows the same data on a log scale.

rameter, we obtain the new 0-ion and 1-ion bright Poisson distributions for the fitting procedure shown in Fig. 3.7. Note that the Poisson distribution representing 2-ions bright is not affected by dark state $\rightarrow$ bright state leakage and hence is not modified.

Chapter 4

Apparatus

This chapter details the experimental apparatus that is common to the experiments with the single- and multi-layer ion trap described in the subsequent chapters. While parts of the apparatus have been set up by previous group members[6], the presented thesis was mainly concerned with the design and construction of the Raman beamline, the first testing of the hybrid setup as well as a comprehensive revision of the complete vacuum setup, trap and microwave drives.

4.1 Vacuum setup

A false-colored schematic of the complete vacuum setup and close-by periphery is shown in Figure 4.1. The whole setup is placed on a 12.7 mm thick breadboard that is situated above a hole in the optical table. The main vacuum chamber is a "spherical octagon" with eight radial DN40 CF fittings between two parallel DN100 CF fittings[7]. The trap assembly is mounted upside down to a custom DN100 CF flange with electrical feedthroughs which positions the trap to the octagon's center. The electrical feedthroughs comprise a 15-pin D-sub feedthrough for DC trap voltages, one high-voltage feedthrough[8] for the trap RF and three SMA feedthroughs for microwave signals used for qubit manipulation. For optical laser access, six of the octagon's radial ports are

[6] i.e. Matthias Kohnen and Martina Wahnschaffe, see ref. [Wah16] for further details.
[7] Kimball Physics, MCF600-SphOct-F2C8
[8] Hositrad, 21309-01-cf

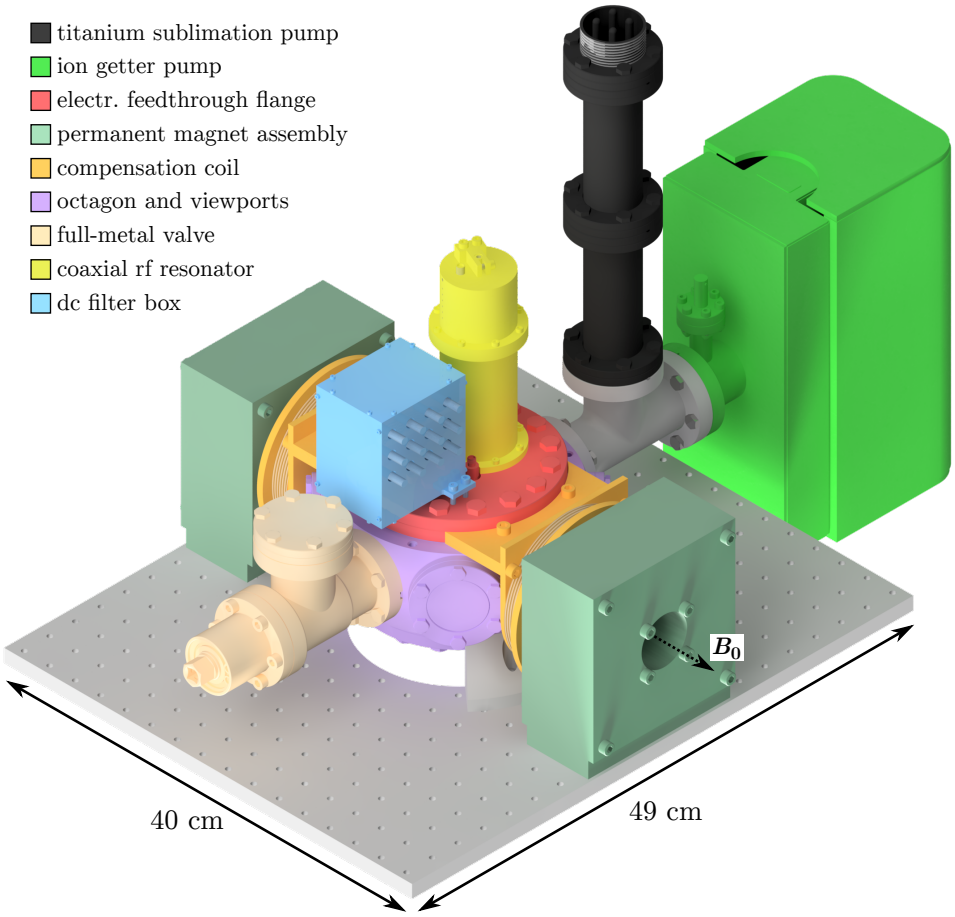

Figure 4.1: False-colored vacuum setup and surrounding periphery.

occupied with DN40 viewports (Fig. 4.2). The imaging setup (cf. Sec. 4.6) for ion fluorescence detection is placed below the vacuum setup and collects photons through a DN100 re-entrant viewport at the bottom of the octagon. All viewports are made from UV fused silica and have a UV anti-reflection coating for 235 nm and 313 nm.

While one of the two remaining octagon's radial sides is connected to a full-metal valve for pre-pumping, the other one connects a titanium sublimation pump with three filaments[9] and an ion-getter pump[10] via a T-piece. The final pressure during operation given by the current on the ion-getter pump controller is around $\leq 1 \times 10^{-11}$ mbar and offers sufficient vacuum quality for the experiments carried out in this thesis.

[9] VACOM, titanium sublimation pump 360819
[10] Gamma Vacuum, TiTan 75S Ion Pump

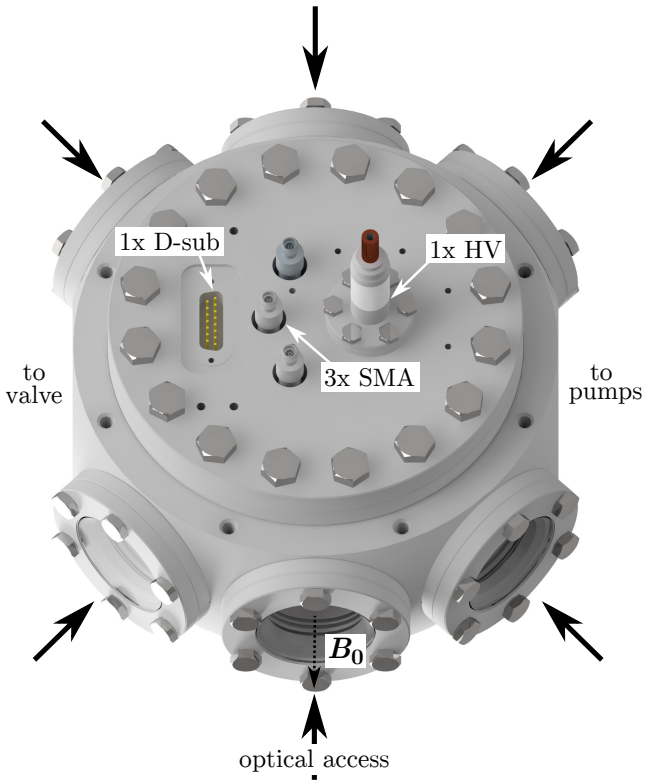

Figure 4.2: Octagon vacuum chamber with six viewports for optical laser access and DN100 flange with one 15-pin D-sub, three SMA and one high-voltage (HV) feedthrough. The latter is connected to the flange via a DN16 CF fitting.

4.2 Bias field

The magnetic field $\boldsymbol{B_0}$ which defines the quantization axis along z' and creates the first-order field-independent qubit transition at $B \simeq 22.3\,\mathrm{mT}$ is produced by a pair of permanent magnet assemblies and a pair of compensation coils which are directly mounted on the octagon vacuum chamber (see Figure 4.1). While the magnet assemblies produce the major part of the field, the compensation coils are used to fine-adjust the magnetic field at the ion's position as well as to compensate possible long-term drifts of the field produced by the magnets. As the presented hybrid setup combines low-noise properties of permanent magnets with the versatility of magnetic field coils, it is a suitable choice to produce long-lived qubit states needed for robust quantum control [HKW+18]. While the coils and magnet assemblies were developed in previous work [Jac17], the field simulations of the magnet assemblies are based on code and ideas by [Jac17] as well as the group of Tobias Schaetz and hence were only modified in this thesis to match the experimental requirements.

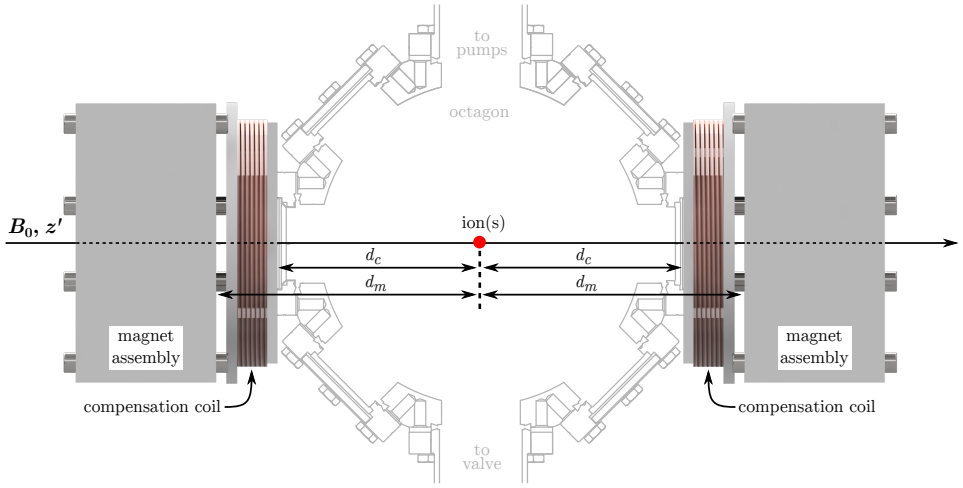

Figure 4.3: Top view of the hybrid setup with quantization axis along z' and the defined distances of each compensation coil and magnet assembly to the ion ($z' = 0$)

4.2.1 Permanent magnets

The permanent magnets used in the magnet assemblies are commercial neodymium magnets[11] (NdFeB) of grade N45 and are among the strongest type of permanent magnets commercially available. The rare earth magnets have a cylindrical shape with dimensions $\varnothing 10 \times 20\,\mathrm{mm}$ and a remanent magnetization of $B_r = 1.32$ - $1.37\,\mathrm{T}$ with a temperature coefficient of about $\kappa = -1.2 \times 10^{-3}\,\mathrm{K}^{-1}$. Stacked to a group of three, the magnets are placed in a magnet holder made of aluminum which has multiple tight-fit magnet sockets to align the stacks parallel to the quantization axis. A front and back panel keep the magnet stacks in position along a direction parallel to the plane. To maintain optical access to the ion trap when placing the magnet assemblies on the optical table, they have a circular through-hole with dimension $\varnothing 44.5\,\mathrm{mm}$ centered around the quantization axis. Here, a magnet assembly without front panel as well as the magnet stack configuration is shown in Appendix A.1.

In the experiment, the two magnet assemblies are placed at a distance $d_m = 130\,\mathrm{mm}$ from the ion position at $z' = 0$ with the front panels of the assemblies facing each other. The magnetic field along the quantization axis (z') was simulated using the open source software package RADIA [CEC98, ECC97] interfaced with Wolfram Mathematica 11.0 and is shown in Fig. 4.4. At the ion position, the simulated magnetic field is $B_{z'=0} \simeq 24.57\,\mathrm{mT}$ and varies about $3\,\mu\mathrm{T/mm}$ around the center.

[11] supermagnete.de, S-10-20-N

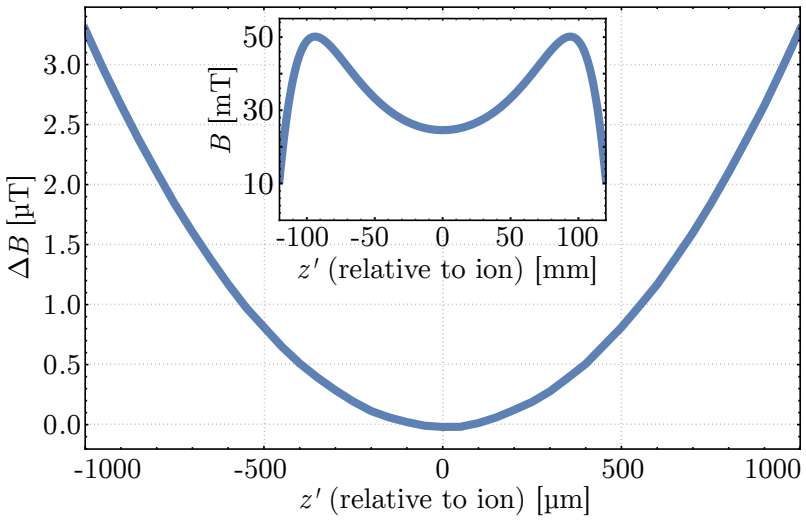

Figure 4.4: Simulated B field variation of two magnet assemblies around $B_{z'=0} \simeq 24.57\,\mathrm{mT}$ along the z'-axis (inset shows larger range).

However, even though the field was simulated and the distance of the assemblies were aligned carefully, the experimentally measured magnetic field at the ion position differs from simulations and was determined to be $\simeq 21.8\,\mathrm{mT}$ by measuring the frequency of transition A and a subsequent calculation of the applied field. The reason for the mismatch is likely caused by magnetic materials within the optical table bending magnetic field lines.

4.2.2 Compensation coils

The compensation coils are needed to bridge the difference between the field needed for the qubit transition at $B \simeq 22.3\,\mathrm{mT}$ and the field produced by the permanent magnets. Like the magnet assemblies, the coils have a through-hole in their geometric center aligned with the viewport of the vacuum chamber in order to maintain optical access. For each coil an enameled copper wire with radius $r = 0.6745\,\mathrm{mm}$ was used to produce 189 windings on an aluminum holder with radius 37.5 mm. Placed between the magnet assemblies, each coil has a distance of d_c to the ion (Fig. 4.3). Electronically, the coils are connected in series with a total resistance of $1.59\,\Omega$ and are powered by a programmable low-noise power supply[12] interfaced with our experiment control via GPIB.

The relative change of the total magnetic field of the hybrid setup as a function of current applied to the compensation coils was measured by observing

[12] Rhode & Schwarz HMP4040

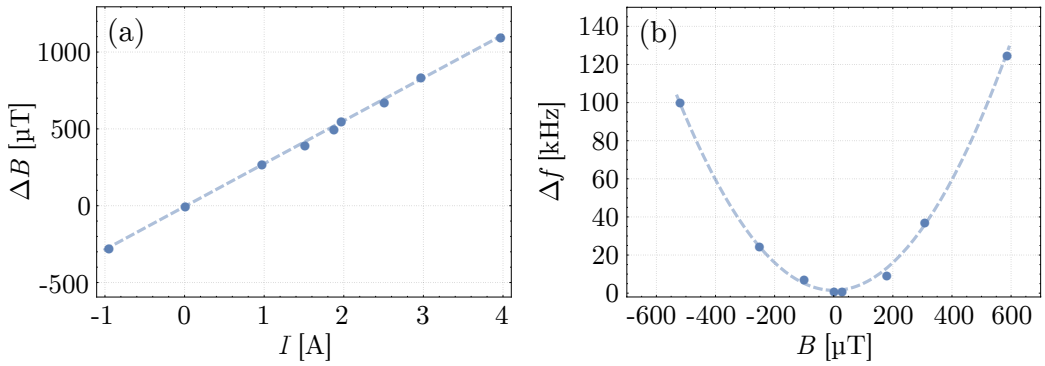

Figure 4.5: (a) Relative change of the magnetic field produced by the compensation coils as a function of the applied current. The data was obtained by performing Rabi frequency scans on a field-sensitive transition. The dashed line shows a linear fit to the data. (b) Relative change of the qubit transition frequency as a function of applied magnetic field. Each data point was measured using standard Ramsey spectroscopy methods. At $B = 0$ the total magnetic field corresponds to $B \simeq 22.3\,\mathrm{mT}$. The dashed line shows a quadratic fit to the data.

the induced frequency shift on the field-sensitive transition A in a frequency scan of a π pulse and scaling it with the corresponding calculated magnetic field sensitivity of $-14.02\,\mathrm{kHz}/\mu\mathrm{T}$. The result is shown in Fig. 4.5 (a) and indicates a linear field change of $(279.35 \pm 3.04)\,\mu\mathrm{T/A}$. With the characterization of the magnetic field produced by the compensation coils, the variation of the transition frequency of the first-order field-independent qubit transition as a function of the applied magnetic field can be measured. Fig. 4.5 (b) shows the result of a Ramsey frequency scan of the qubit transition for different magnetic fields applied, revealing the expected first-order field-independent behavior of the transition around $B \simeq 22.3\,\mathrm{mT}$ at $\Delta B = 0$.

4.2.3 Hybrid setup performance

In order to investigate the free-running magnetic field stability of the hybrid setup, the frequency of transition A was tracked as a function of time during 60 min using a Ramsey frequency scan. The frequency variation was translated into a B field variation by dividing the frequency shift by the transition's magnetic field sensitivity. As depicted in Fig. 4.6, the total magnetic field changes by roughly $1.7\,\mu\mathrm{T}$ in a 60 min interval and is clearly correlated with the temperature drift of the magnet assemblies recorded in a simultaneous measurement.

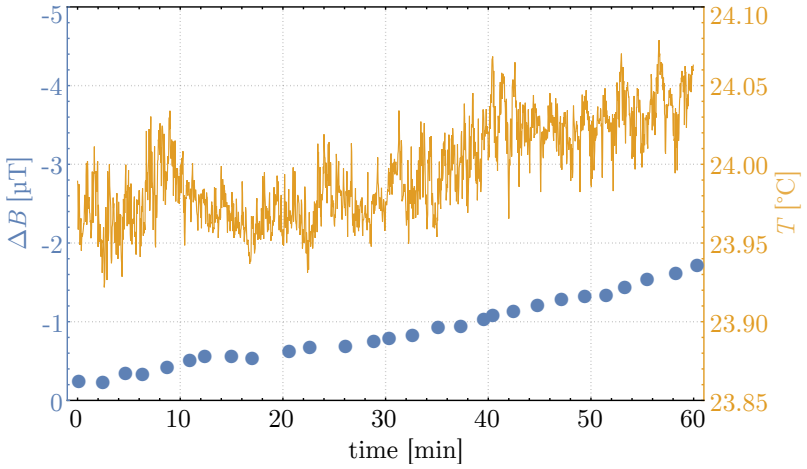

Figure 4.6: Two-axes plot showing the relative magnetic field change of the hybrid setup and the temperature of one magnet assembly over time. At $\Delta B = 0$ the total magnetic field corresponds to $B \simeq 22.3\,\mathrm{mT}$.

For a temperature drift of $\Delta T = 65\,\mathrm{mK}$ and a magnetic field of 21.8 mT produced by the magnet assemblies, the observed field change is approximately in line with the temperature coefficient of the remanent magnetization. As a magnetic field mismatch can result in imperfect qubit shelving or state preparation (cf. Sec. 3.5), the magnetic field is re-centered at 22.3 mT before every sensitive measurement by performing a Ramsey experiment on transition A and adjusting the current applied to the compensation coils appropriately.

To emphasize the benefit of the hybrid setup over using solely a pair of field coils to generate the quantization field at 22.3 mT, we determine the coherence time of a field-sensitive transition for both cases. As shown in Fig. 4.7, the coherence time using the hybrid setup is about 10 times longer compared to the one using only field coils[13]. Based on the coherence times, the rms amplitude of the effective magnetic field fluctuations using the hybrid setup evaluates to [RSK+16]

$$\sqrt{\langle \Delta B^2 \rangle} = \frac{\hbar}{\mu_B \, \tau_2} = 32.85\,\mathrm{nT} \tag{4.1}$$

including the magnetic field sensitivity of the transition (cf. Sec. 4.2.2).

[13]The data using solely field coils was taken in a previous version of the apparatus employing the field coils characterized in ref. [Gro14] and a power supply from Delta Elektronika (model: SM 70-90). The installed ion trap was the 'SpyderTrap' and is described in ref. [WHZ+17].

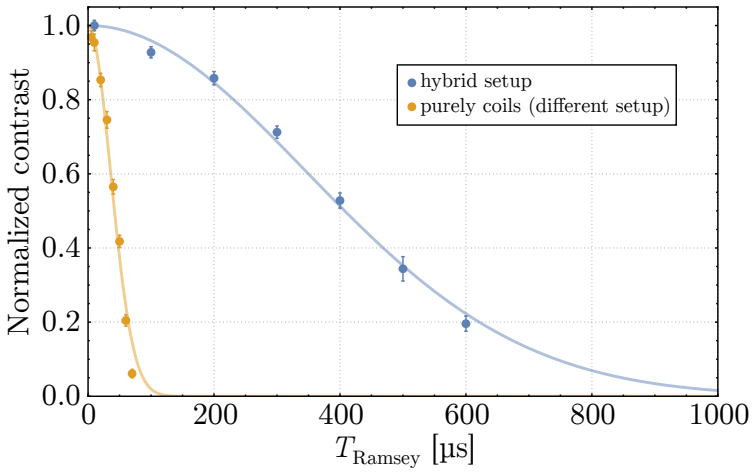

Figure 4.7: Normalized contrast of a series of Ramsey experiments on the field-sensitive transition A as a function of the Ramsey time T_{Ramsey} between two $\pi/2$ pulses. While the blue data was measured using the hybrid setup to produce the quantization field of 22.3 mT, the orange data was taken purely using a pair of field coils. The solid lines are fits to the data using a Gaussian decay function $e^{-\left(\tau/\sqrt{2}\tau_2\right)^2}$. The extracted coherence time τ_2 of the fits is given by the time where the normalized contrast has decreased to $1/\sqrt{e}$ and is 346 μs for the hybrid setup and 36 μs for the field coils.

4.3 Trap drives

4.3.1 RF setup

The radio-frequency signal applied to the ion trap is generated in a chain of commercial RF devices and is subsequently amplified in a custom built RF resonator. A simplified version of the setup before the resonator is shown in Fig. 4.8 and includes a tunable RF signal generator[14] and a low-noise amplifier[15]. In total, the setup can produce up to ≈ 22 dBm at frequencies up to 512 MHz. The directional coupler samples -10 dB of the power reflected by the resonator and is used to optimize the impedance matching between the resonator and the remaining RF chain as well as for monitoring during normal operation. The ground loop between the signal generator's ground and the trap's ground is interrupted via a DC-DC block before the resonator. As for the experiments in Ch. 5, the amplifier is placed in an insulated enclosure enabling passive temperature-stabilization and is operated close to its 1 dB

[14] Hewlett Packard, HP 8640B
[15] Mini Circuits, ZHL-2010+

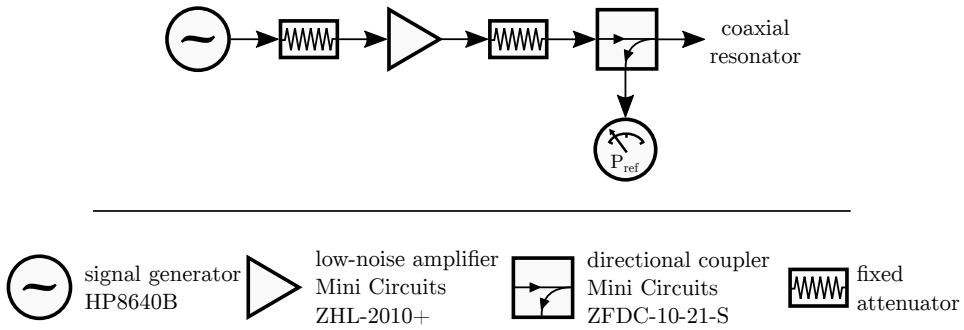

Figure 4.8: Simplified signal path for generating low-noise RF trap voltages that are coupled to the RF resonator

compression point in order to reduce possible amplitude variations of the signal generator. In the whole setup, only SMA parts and semi-rigid SMA cables are used.

4.3.1.1 RF resonator

The home-built RF resonator used for voltage amplification of the trap RF has a coaxial configuration [JMBW95] which is formed by an inner conductor made of copper and a surrounding shield made of aluminum (see Fig. 4.9). The resonator extends from atmosphere into the vacuum chamber and has a modular design which allows to change the resonator's length at atmosphere l as well as the resonator's resonance frequency w_R in discrete steps if needed[16]. The inner conductor has a diameter of $\varnothing 6\,\mathrm{mm}$ and extends into the vacuum chamber via a high-voltage feedthrough with DN16 CF fitting which itself is bolted to the DN100 feedthrough flange (Fig. 4.2). The outer shield is directly connected to ground via the feedthrough flange and has an inner diameter of $\varnothing 50\,\mathrm{mm}$ at atmosphere and $\simeq \varnothing 16\,\mathrm{mm}$ at vacuum. While the inner conductor is connected to the outer shield via an aluminum clamp at the top, it ends at vacuum side on a trace of a custom circuit board as introduced in Sec. 5.1.5 and 6.1.3. The RF signal is coupled into the resonator using a wire loop whose enclosed area is adjusted externally to optimize the incoupling efficiency. To reduce the possible impact of lab temperature drifts on the electrical properties of the resonator, the whole resonator is enclosed in several foam sheets and a space blanket.

In a simplified treatment, the resonance behavior of the resonator can be

[16]This might become useful when other trap designs with different capacitances are installed.

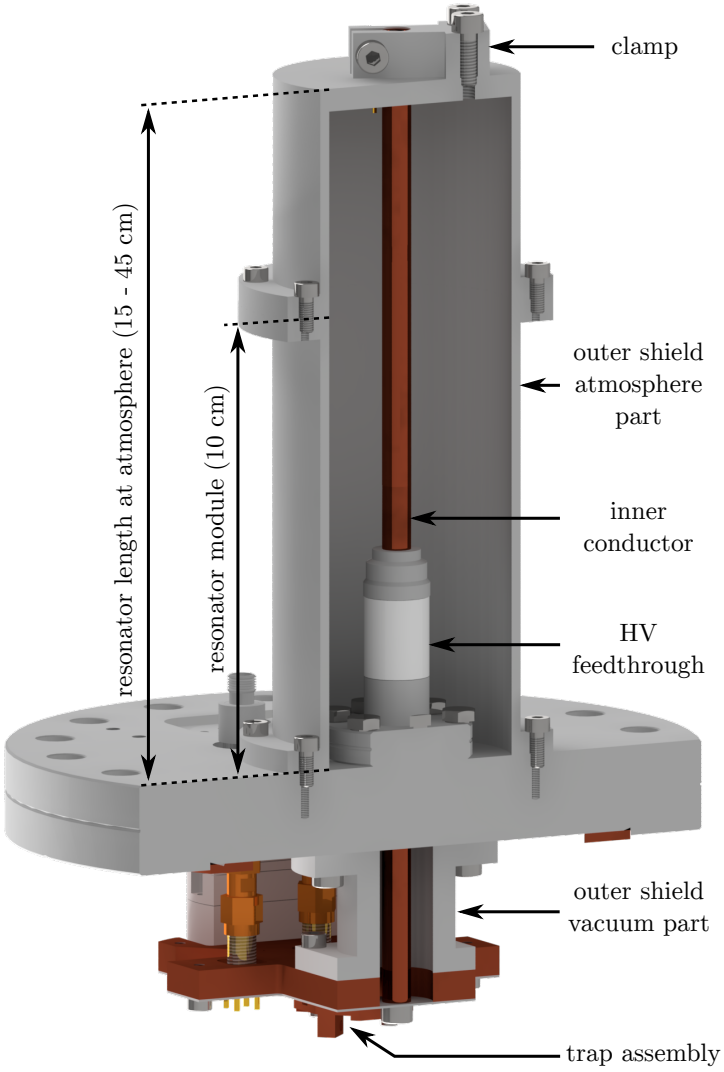

Figure 4.9: Cross-section of the coaxial RF resonator. The resonator length and resonance frequency can be changed in discrete steps due to its modular design. The wire loop used for incoupling is soldered to a SMA jack next to the clamp and is not shown here. The design is inspired by ref. [JMBW95]

expressed as an RLC circuit with the resonator's inductance L_r, capacitance C_r and resistance R_r. In order to infer the capacitance C_t of an installed trap assembly (where $C_t \parallel C_r$) from the resonator's resonance frequency ω_R via the relation

$$\omega_R = \frac{1}{\sqrt{L_r \cdot (C_r + C_t)}} \tag{4.2}$$

both L_r and C_r have to be determined in a separate measurement using known capacitive loads. Following this, Fig. 4.10 (left) shows ω_R^{-2} as a function of connected capacitors for an exemplary resonator length of $l = 15\,\mathrm{cm}$. While the slope of the linear fit determines the inductance to $L_{r,l=15\mathrm{cm}} \simeq 97.2\,\mathrm{nH}$, its intercept with the $\hat{y}$-axis allows to calculate the capacitance to $C_{r,l=15\mathrm{cm}} \simeq 5.5\,\mathrm{pF}$. Using these values and resonator lengths, the capacitance of the single-layer trap assembly (cf. Sec. 5.1.5) was measured to be $\simeq 3.28\,\mathrm{pF}$.

Repeating the measurement for two different resonator length l_1 and l_2 ($l_2 > l_1$) enables an approximation of the resonator's inductance $L_r(l)$ and capacitance $C_r(l)$ as a function of the length l. Assuming a linear dependence of both properties, they are given by

$$\begin{aligned} C_r(l) &= C_{r,\mathrm{offset}} + C_{r,l} \cdot l \\ L_r(l) &= L_{r,\mathrm{offset}} + L_{r,l} \cdot l \end{aligned} \tag{4.3}$$

with

$$\begin{aligned} C_{r,l} &= \frac{C_{r,l_2} - C_{r,l_1}}{l_2 - l_1} \\ L_{r,l} &= \frac{L_{r,l_2} - L_{r,l_1}}{l_2 - l_1} \\ C_{r,\mathrm{offset}} &= C_{r,l_1} - L_{r,l} \cdot l_1 \\ L_{r,\mathrm{offset}} &= L_{l_1} - L_{r,l} \cdot l_1 \ . \end{aligned} \tag{4.4}$$

Following this approach in a separate measurement, we obtain $C_{r,\mathrm{offset}} = 1.96\,\mathrm{pF}$, $L_{r,\mathrm{offset}} = 36\,\mathrm{nH}$, $C_{r,l} = 0.24\,\frac{\mathrm{pF}}{\mathrm{cm}}$ and $L_{r,l} = 4.08\,\frac{\mathrm{nH}}{\mathrm{cm}}$ and can estimate ω_R for an arbitrary connected C_t as a function of the resonator length using Eq. 4.2 as exemplary shown for $C_t = 3.28\,\mathrm{pF}$ in Fig. 4.10 (right).

In order to estimate the applied RF voltage to the trap for a given RF input power, the resonator's resistance R_r has to be known. As most of the experiments within this thesis are performed with the single-layer assembly (cf. Ch. 5) and a 45 cm long resonator, the following treatment focuses on this

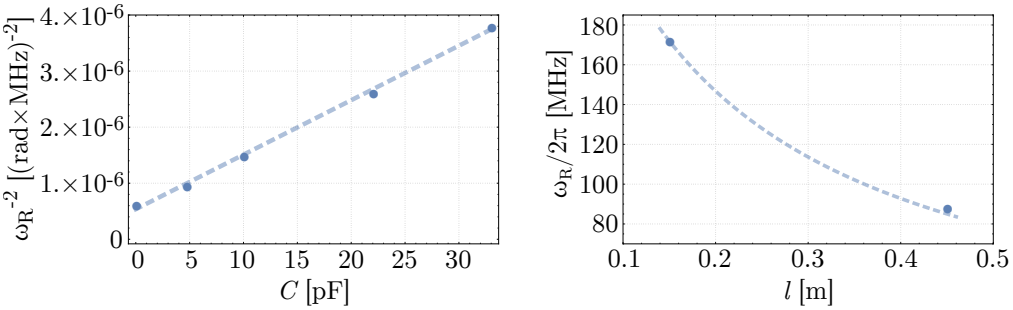

Figure 4.10: Left: measured resonance frequency for a resonator length of $l = 15\,\text{cm}$ as a function of known capacitive loads. The dashed line is a linear fit to the data points. Right: resonance frequency for $C_t = 3.28\,\text{pF}$ as a function of resonator length. While points correspond to measured data, the dashed line follows the calculated values obtained using the approach explained in the text.

specific experimental condition. Fig. 4.11 (left) displays a S_{11} measurement using a Vector Network Analyzer yielding a loaded quality factor of $Q_{\text{loaded}} \simeq 367$. On resonance the resonator resistance for $l = 45\text{cm}$ can be estimated as

$$R_{r,l=45\text{cm}} = Q\sqrt{\frac{L_{r,l=45\text{cm}}}{C_{r,l=45\text{cm}} + C_t}} \tag{4.5}$$

where Q represents the resonator's unloaded quality factor. Inserting $C_t = 3.28\,\text{pF}$, $C_{r,l=45\text{cm}} = 12.7\,\text{pF}$ and $L_{r,l=45\text{cm}} = 219.6\,\text{nH}$ in Eq. 4.5 and assuming $Q = 2 \cdot Q_{\text{loaded}}$, we obtain $R_{r,l=45\text{cm}} = 86.13\,\text{k}\Omega$. Based on the resistance, the RF voltage at the trap can be calculated for different applied RF powers (see Fig. 4.11 on the right).

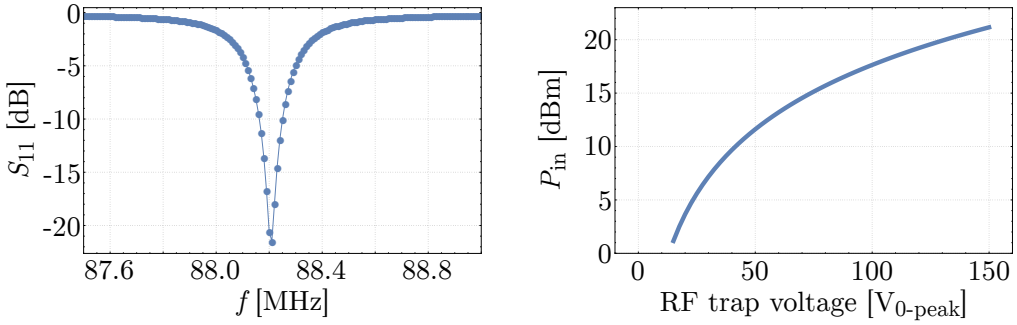

Figure 4.11: Left: S_{11} measurement for a resonator length of 45 cm while the single-layer trap assembly with $C_t = 3.28\,\text{pF}$ is connected. A Lorentzian fit yields a full width at half maximum of $\sim 240\,\text{kHz}$ and a Q_{loaded} factor of ~ 367. Right: Calculated applied RF voltage at the trap for given RF input powers at the resonator based on $R_{r,l=45\text{cm}}$.

4.3.2 DC setup

The DC trap voltages used for axial ion confinement and ion positioning are produced by several multi-channel arbitrary waveform generators [BWB+13, Bow15] developed for applications like fast ion transport or microwave pulse shaping. The generators are based on 16-bit digital-analog converters with an update rate of 50 MHz and an output voltage range of ±10 V. Each output channel is connected to the DC filterbox shown in Fig. 4.12 (a) using SMA cables. The filterbox holds a stack of 3-channel custom printed-circuit boards (PCBs) for low-pass filtering[17] of each DC voltage (see Fig. 4.12 (b)) and is directly mounted to the feedthrough flange introduced in 4.1 using the 15-pin D-sub connector. While hooked up to floating power supplies, the signal grounds of all generator channels are kept isolated from the aluminum case via PVC shoulder washers to avoid ground loops. As for the experiments in Ch. 6, the output voltage range of the generators can be extended to ±50 V by interposing another 3-channel PCB including low-noise voltage amplifiers[18] between the generator outputs and the filterbox inputs. An example of such an amplifier board is shown in Fig. 4.12 (c).

As explained in Sec. 5.1.5, the D-sub feedthrough is routed onto a filter-board inside the vacuum chamber holding a second low-pass filter stage of RC filters with $f_{\mathrm{co}} = 194\,\mathrm{kHz}$ for each DC channel. The filter performance of both DC filter stages combined was investigated by measuring its filter transfer function and is shown for one channel in Fig. 4.13.

4.4 Photoionization laser system

As outlined in Sec. 3.1, the photoionization process of neutral beryllium relies on a resonant two-photon process using 235 nm photons. In our experiment, the 235 nm light is generated by frequency-quadrupling a commercial solid-state laser system[19] producing up to 1.5 W at 940 nm as shown in Fig. 4.14. After passing an optical isolator, the infrared light is coupled into a power enhancement bow-tie cavity with an intra-cavity periodically poled potassium titanyl phosphate (PPKTP) crystal for frequency-doubling. It has dimensions of $1 \times 2 \times 20\,\mathrm{mm}^3$, a poling period of 5.925 μm and an anti-reflection coating for

[17] Mini Circuits, LPF-B0R3+, $f_{\mathrm{co}} = 460\,\mathrm{kHz}$
[18] Linear Technology Corporation, LTC6090
[19] Toptica Photonics, TA pro 13160

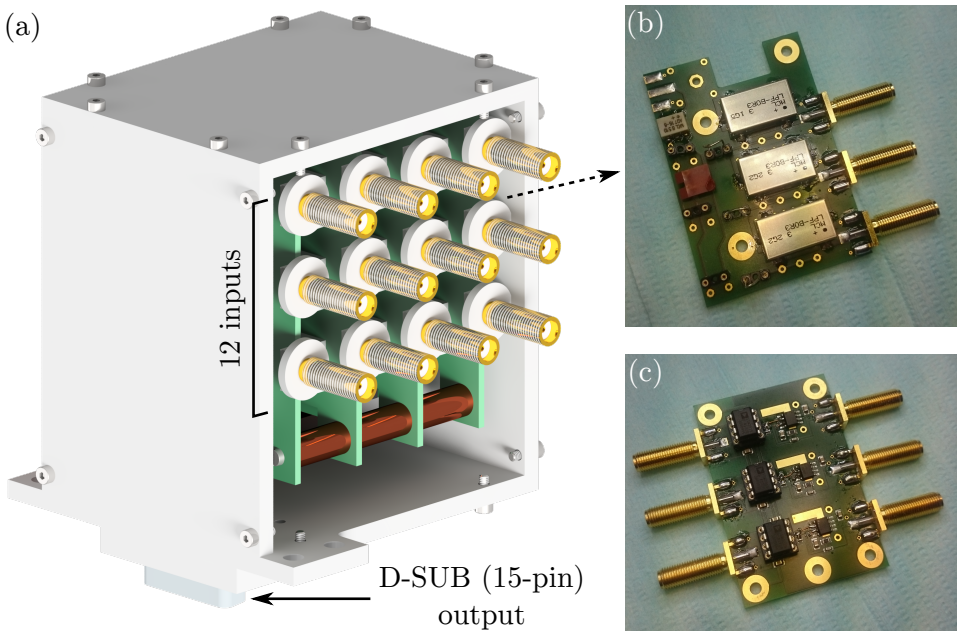

Figure 4.12: DC filterbox setup. (a) DC filterbox with 12 SMA inputs and one D-sub (15-pin) output. The filterbox holds a stack of 3-channel printed-circuit boards for low-pass filtering, as shown in inset (b), and is directly mounted on the vacuum chamber. (c) High-voltage amplifier boards to extend the output voltage of the arbitrary waveform generators from $\pm 10\,\mathrm{V}$ to $\pm 50\,\mathrm{V}$ if needed.

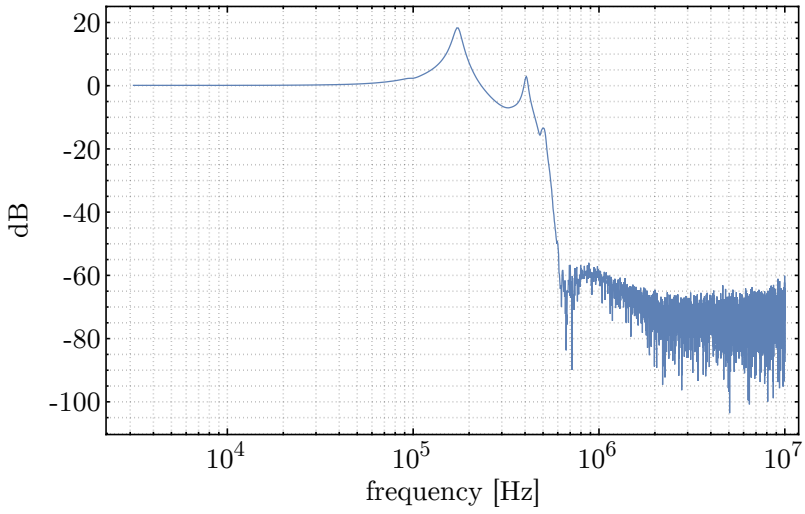

Figure 4.13: Filter function of the combined filter system. The $\hat{y}$-axis shows the output signal level after the filters relative to the input signal level as a function of the frequency. At typical secular frequencies for our traps between $1 - 10\,\mathrm{MHz}$, the electronic noise suppression is above $60\,\mathrm{dB}$.

940/470 nm. To fulfill the quasi phase-matching condition and maximize the conversion efficiency, the PPKTP crystal is temperature-stabilized to 21.7 °C in a custom intra-cavity oven. In normal operation, the first cavity generates around $P_{\text{out}} \simeq 240\,\text{mW}$ at 470 nm for $P_{\text{in}} \simeq 1\,\text{W}$ at 940 nm. After splitting the power with another beryllium lab, around half of the optical power in the blue is coupled into the second power enhancement bow-tie cavity using an intra-cavity $4 \times 4 \times 10\,\text{mm}^3$ Brewster-cut BBO crystal with type-I critical phase matching for frequency-doubling. At an input power of $P_{\text{in}} \simeq 100\,\text{mW}$, this cavity produces up to $P_{out} \simeq 5\,\text{mW}$ at 235 nm. Both cavities are locked in length by the Pound-Drever-Hall technique [DHK+83] for which the needed sidebands are produced via laser current modulation. The frequency of the diode laser is monitored after the first SHG via a wavemeter and manually tuned to an experimentally optimized value of 638.03950 THz [Wah16] by adjusting the piezo voltage of the 940 nm laser system.

After a single-pass AOM for fast beam switching, the 235 nm beam passes a telescope and pin-hole for transversal mode-cleaning. Finally, an $f = 150\,\text{mm}$ lens focuses the beam into the vacuum chamber, producing a beam diameter of $\sim 40\,\mu\text{m}$ at the ion position. As deep UV photons can induce surface charging in the trap which in turn can cause uncontrollable secular frequency drifts, we reduce the power of the UV beam to a few hundred μW and limit the time pulse of the laser to a couple of ms (cf. Sec. 5.1.6).

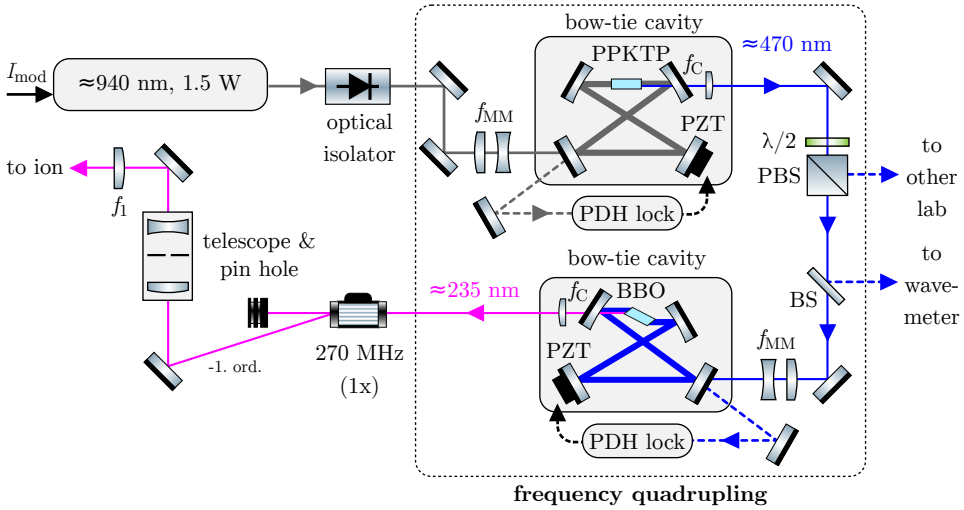

Figure 4.14: Laser system for the resonant two-step photoionization of neutral beryllium ions. The setup is based on a frequency-quadrupled commercial solid-state laser system. See [LAK+13] for further details.

4.5 Cooling and detection laser system

As explained in Chapter 3, five UV laser beams with different wavelengths around $\approx 313\,\mathrm{nm}$ are needed in order to perform state initialization, Doppler cooling/state detection, optical pumping and Raman sideband cooling on the beryllium ions. Following the approach detailed in [WOV+11], the 313 nm light is produced by utilizing multiple nonlinear frequency conversions on the outputs of commercially available fiber lasers[20] running at $\approx 1051\,\mathrm{nm}$ and $\approx 1550\,\mathrm{nm}$. As depicted in Fig. 4.15, the UV light generation starts with the sum-frequency generation (SFG) of a 1051 nm and 1550 nm fiber laser, the output beams of which are overlapped in a magnesium-doped periodically poled lithium niobate (MgO:PPLN) crystal[21] using a dichroic mirror.

The PPLN crystal has dimensions of $0.5 \times 10 \times 40\,\mathrm{mm}^3$ and contains three poled channels with cross-section of $0.5 \times 0.5\,\mathrm{mm}^2$ and period lengths of $11.12\,\mu\mathrm{m}$, $11.17\,\mu\mathrm{m}$ and $11.22\,\mu\mathrm{m}$, respectively. To maximize conversion efficiency, both infrared beams are vertically polarized with respect to the large crystal surface and focused inside the crystal center with a measured free space waist of $\omega_{1051} = 42.1 \pm 1\,\mu\mathrm{m}$ and $\omega_{1550} = 44.7 \pm 2\,\mu\mathrm{m}$, respectively. For quasi phase-matching, the crystal temperature is stabilized at 190.59 °C with 0.01 °C stability. The generated sum-frequency light at $\approx 626\,\mathrm{nm}$ is separated from the infrared beams after the PPLN using a dichroic mirror. For input powers of $P_{1051} = 5.04\,\mathrm{W}$ and $P_{1550} = 4.65\,\mathrm{W}$, the SFG setup generates up to $P_{626} = 3.07\,\mathrm{W}$ in the red. Based on these power levels and the crystal length $l_{\mathrm{PPLN}} = 40\,\mathrm{mm}$, the SFG efficiency η_{SFG} can be calculated to

$$\eta_{\mathrm{SFG}} = \frac{P_{626}}{P_{1051} \times P_{1550} \times l_{\mathrm{PPLN}}} = 3.27\,\%\mathrm{W}^{-1}\mathrm{cm}^{-1} \tag{4.6}$$

and is in good agreement with the ones found in the literature [WOV+11, LAK+13]. In order to produce a second 626 nm beam line with different frequency, the unconverted 1051 nm light of the first SFG setup is overlapped with the output of a second 1550 nm fiber laser with slightly lower wavelength than the other one in a second SFG setup. With a PPLN crystal temperature of 169.75 °C for quasi-phase matching and similar free space waists as given before, this SFG setup generates up to $P_{626} = 0.82\,\mathrm{W}$ for input powers of

[20] NKT Photonics, seed laser: Koheras Adjustik, fiber amplifier: Koheras Boostik HPA
[21] Covesion Ltd.

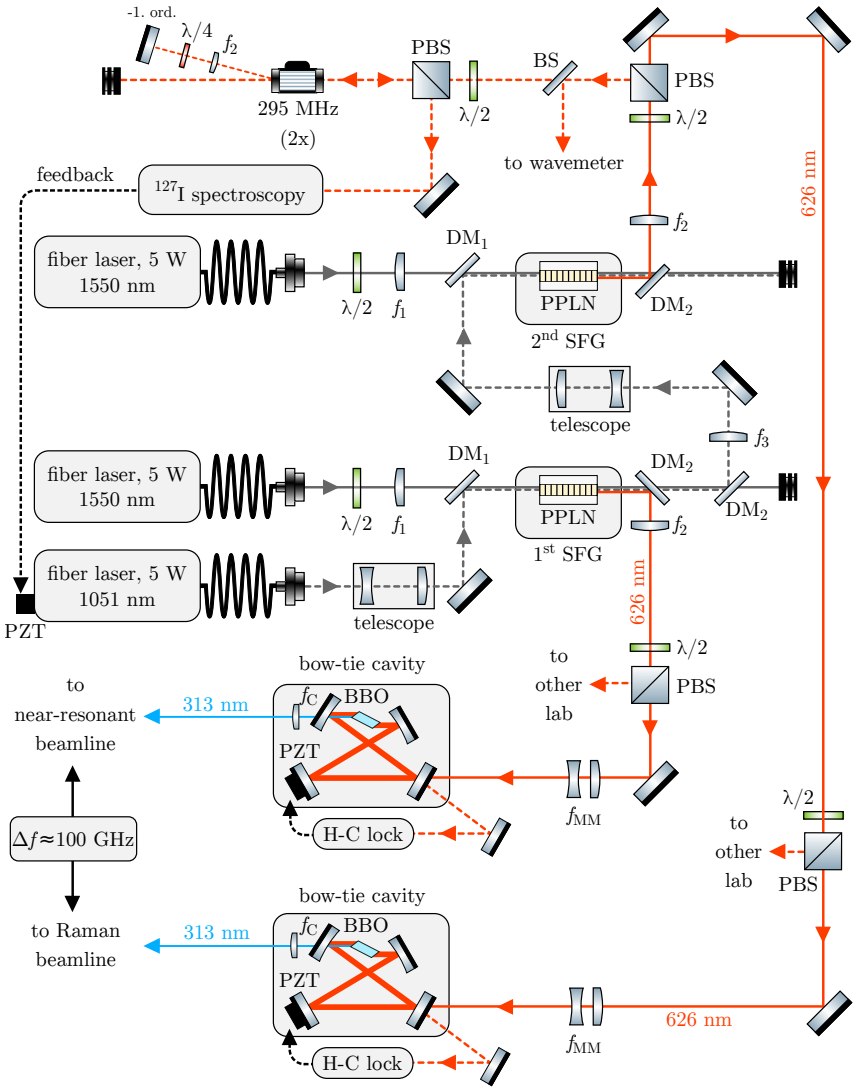

Figure 4.15: All-solid state continuous laser system for the generation of 313 nm light based on multiple nonlinear frequency conversions of commercial fiber lasers. In the first stage, a 1051 nm fiber laser is subsequently mixed with two 1550 nm lasers running at slightly different wavelength in order to generate two 626 nm beams utilizing the sum-frequency generation technique. In the second stage, both 626 nm beams are frequency-doubled to the UV using a power enhancement cavity in bow-tie configuration. The two resulting beams at 313 nm have a relative detuning of ~ 100 GHz and can be used to generate Raman beams for motional sideband cooling as well as near-resonant beams for Doppler cooling and resonant interactions.

$P_{1051} = 2.3\,\mathrm{W}$ and $P_{1550} = 4.75\,\mathrm{W}$. Using Eq. 4.6 this calculates to an efficiency of $\eta_{\mathrm{SFG}} = 1.87\,\%\mathrm{W}^{-1}\mathrm{cm}^{-1}$. Here, the difference in conversion efficiency between both SFG setups is likely caused by the distorted beam profile of the 1051 nm laser after passing the first SFG setup.

To frequency stabilize the red light produced in the second SFG setup to sub-MHz level, a fraction of the beam is frequency shifted to the red by 590 MHz using an acousto-optical modulator (AOM) and subsequently coupled into a frequency-modulation (FM) spectroscopy setup [BLLO83]. Here, the beam is frequency-modulated with a 40 MHz AOM and locked to an absorption line in molecular iodine ^{127}I using electric feedback on the 1051 nm fiber laser's piezo input, similar to [Ste14].

After sharing the power of both 626 nm beamlines with another lab, each beam is coupled into a power enhancement bow-tie cavity using an intra-cavity Brewster-cut BBO with dimensions of $4 \times 4 \times 20\,\mathrm{mm}^3$ for second-harmonic generation (SHG). Type-I critical phase matching is achieved by aligning the crystal's angle with respect to the circulating intra-cavity beam using a 5-axis translation stage. Both cavities are locked in length via feedback on a piezo-mounted cavity mirror. The locking setup is based on the Hänsch-Couillaud technique [HC80] and includes a digital PI controller [HMF+18]. The output power at 313 nm of one cavity as a function of input power at 626 nm is shown in Fig. 4.16.

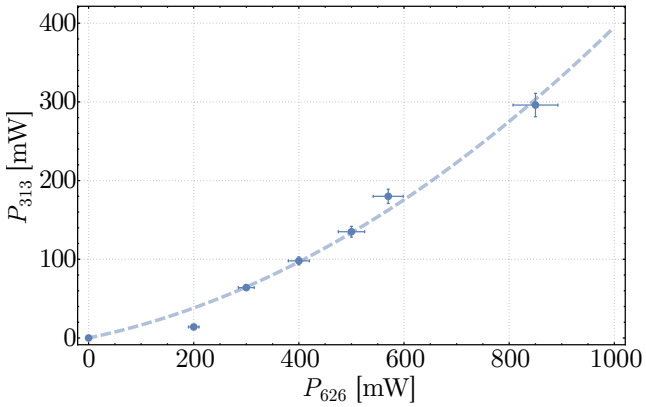

Figure 4.16: UV output power of the frequency doubling cavity in the Raman beamline as a function of red input power send to the cavity. The dashed line shows a quadratic fit to the data points. The error bars indicate the uncertainty of the thermal power sensor.

After the SHG stage, the first and second beam have absolute frequencies of $\simeq$957.296766 THz and $\simeq$957.396766 THz, respectively. While the first beam

is $\sim 100\,\mathrm{GHz}$ red detuned to the $^2S_{1/2} \leftrightarrow {}^2P_{3/2}$ transition (D2 line of Be II, $\lambda_{D2} \simeq 313.12\,\mathrm{nm}$) and used to generate Raman beams for driving motional sideband transitions, the second beam is near-resonant with the D2 line and used to generate beams for state initialization, Doppler cooling/state detection and repumping.

4.5.1 Raman beamline

Fig. 4.17 shows the UV setup of the beamline used for generating two Raman beams. After the cavity, the 313 nm light is first intensity stabilized by diffracting the intensity above a certain threshold into the 1st order of an 110 MHz AOM[22]. Using a digital PI controller [HMF+18] for feedback, the stabilization setup reduces the rms intensity fluctuations on the two Raman beams by a factor of six as depicted in Fig. 4.18.

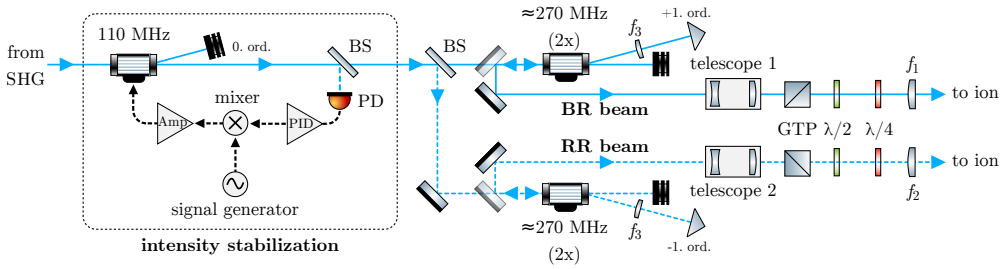

Figure 4.17: UV AOM setup to generate two Raman beams for driving motional sidebands of the qubit transition.

After splitting the beam with a 50:50 beamsplitter into two beams called 'blue Raman' (BR) and 'red Raman' (RR), both beams are frequency-split by two 270 MHz AOMs[23] in double-pass configuration. Using a tunable DDS unit as RF source for the BR AOM and a digitally controlled RF signal generator[24] at a fixed frequency for the RR AOM, the relative frequency difference between both beams can be set around the qubit transition frequency at $\omega_{\mathrm{qubit}} \simeq 1082.55\,\mathrm{MHz}$ with a common detuning of about 100 GHz from the next optical transition. The beat signal obtained by overlapping both Raman beams on a fast photodiode connected to a spectrum analyzer is depicted in Fig. 4.19 and gives a full width at half maximum of $140 \pm 21\,\mathrm{Hz}$ based on a Lorentzian fit of the central peak.

[22] Gooch & Housego
[23] IntraAction
[24] Trinity Power

After passing a telescope for beam shaping and a Glan-Taylor prism for polarization cleaning, the BR (RR) beam passes two waveplates to set the polarization and is focused into the vacuum chamber using an $f_1 = f_2 = 150\,\text{mm}$ lens. The resulting beam diameters above the ion trap are both about $\sim 30\mu\text{m}$. For Raman sideband cooling, we typically set the power of each beam around 150 - 200 μW and optimize the beam polarization experimentally by maximizing the Rabi frequency. The latter is necessary as the employed beam configuration (cf. Fig. 5.6) does not allow any pure σ^+, σ^- or π beam polarization with respect to the quantization axis.

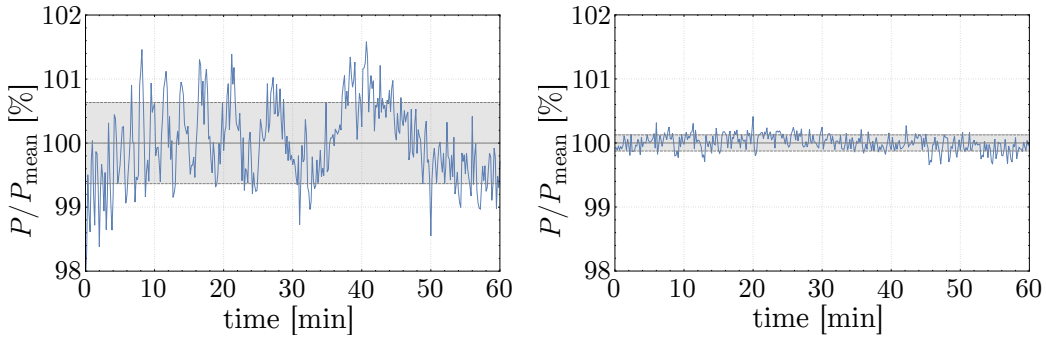

Figure 4.18: Power variation of the RR beam relative to the beam's mean power over time. The solid grey lines indicate the mean power, the dotted gray lines show the standard deviation from the mean. Left: with intensity stabilization disabled. Right: with intensity stabilization enabled.

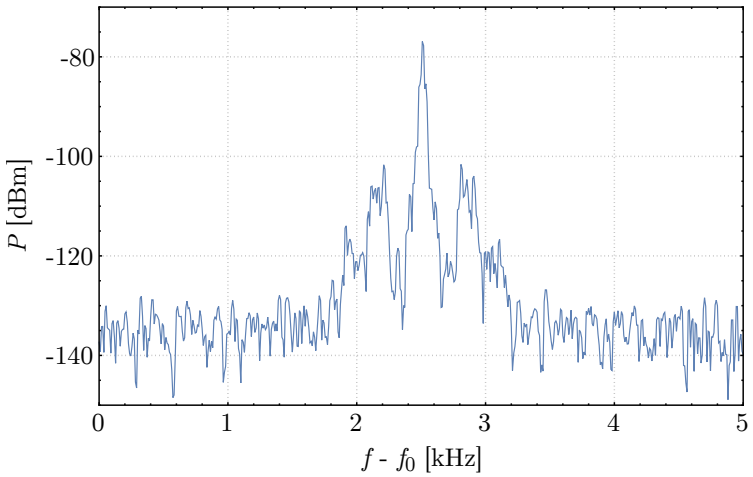

Figure 4.19: Beat signal of the two Raman beams with a relative detuning near the qubit transition as a function of frequency where $f_0 \simeq 1082.54459\,\text{MHz}$.

4.5.2 Near-resonant beamline

After passing an intensity stabilization as for the detuned beamline, the 313 nm light of the near-resonant beamline is split into the three beams called 'blue Doppler' (BD), 'blue Doppler detuned' (BDD) and 'repumper' (RE) using two 50:50 beamsplitters (see Fig. 4.20).

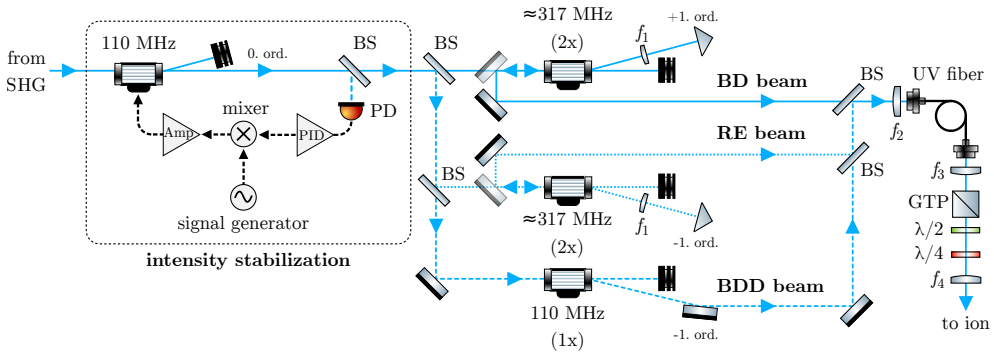

Figure 4.20: UV AOM setup of the near-resonant beamline. The 313 nm light is divided into three beams with different frequency called 'Blue Doppler' (BD), 'Blue Doppler Detuned' (BDD) and 'repumper' (RE). Before being delivered to the ions, all beams are merged in a UV fiber.

The BD beam is blue shifted by 634 MHz using a double-pass AOM[25] and can be fine tuned to perform either state-dependent fluorescence detection or Doppler cooling on the closed cycling transition. In the experiment the BD power is set around the saturation intensity of the transition. The BDD (BD detuned) is about 744 MHz red detuned from the BD and has a few orders of magnitude more power than the BD beam. It is mainly used to efficiently Doppler cool hot ions in the loading sequence (cf. Sec. 5.1.6) as well as for state initialization of the ion to the stretched state $\left|{}^2S_{1/2}, F = 2, m_F = 2\right\rangle$ via optical pumping. The RE beam is about 1268 MHz red detuned from the BD and is needed to transfer population during motional sideband cooling into the target state $\left|{}^2S_{1/2}, F = 2, m_F = 2\right\rangle$ by resonantly driving the $\left|{}^2S_{1/2}, F = 1, m_F = 1\right\rangle \leftrightarrow \left|{}^2P_{3/2}, m_J = 1/2, m_I = 3/2\right\rangle$ transition. To simplify the beam-alignment and to improve the mode-quality, all three beams are again overlapped via two 50:50 beamsplitters and coupled into a 20 cm long single-mode hollow-core photonic crystal fiber with deep-UV transmission [GFW+14]. After passing a collimation lens and polarization optics for a pure σ^+-polarization, the merged beam is focused into the vacuum chamber

[25] IntraAction

along the quantization axis. The lens has a focal length of $f = 150\,\text{mm}$ and generates a beam diameter of about $40\,\mu\text{m}$ at the ion position. Based on this waist, the power levels of the BD and RE beam are set to a few μW while the BDD beam power is typically set to $\sim 400\,\mu\text{W}$.

4.6 Imaging setup

The read-out of the ion state is performed via state-dependent fluorescence detection on the closed cycling transition (cf. Sec. 3.5) using the BD beam of the near-resonant beamline (cf. Sec. 4.5). The full imaging setup consists of a custom objective[26] and a subsequent commercial microscope objective[27] as sketched in Fig. 4.21. While the microscope objective has an unknown lens configuration with a magnification of 3×, the custom objective consists of 5 individual lenses and has a magnification of 13× . The custom objective's numerical aperture is NA = 0.41 and thus covers about 4.4% of the solid angle. It is placed at atmosphere inside a re-entrant viewport at the bottom of the vacuum chamber in order to maintain the ideal working distance to the ions of around 47.2 mm.

[26] Sill Optics, custom
[27] Thorlabs, LMU-3X-UVB

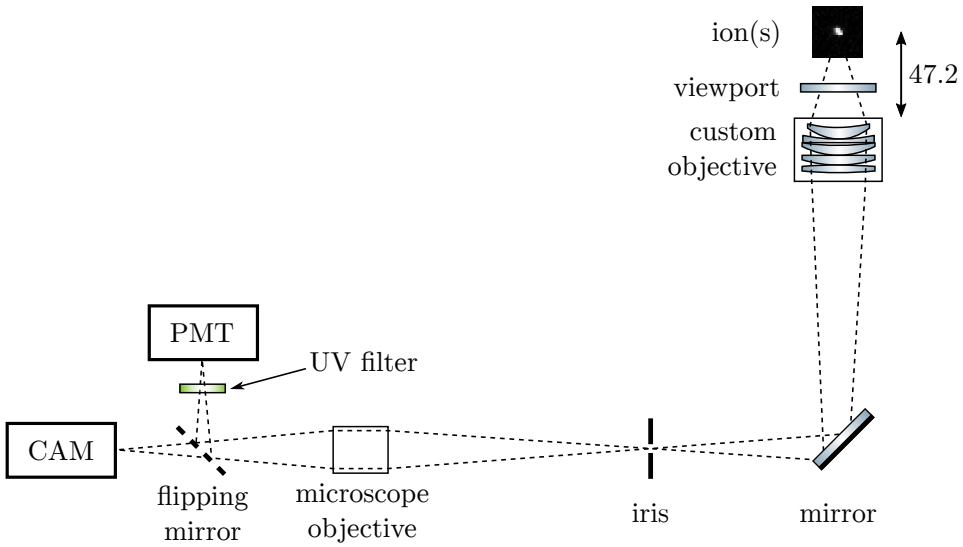

Figure 4.21: Schematic of the imaging setup used for state-dependent fluorescence detection of the $^9Be^+$ ions at $\simeq$313 nm. The total magnification of the imaging setup is 39. Distances in mm (not to scale).

After the custom objective, the collected light is reflected at a 2" UV mirror[28] at 45° and produces an intermediate image a few cm before the microscope objective. Depending on the position of a 1" flipping mirror, the microscope objective re-images the ions either onto an EMCCD camera[29] or a photon-multiplier tube[30] (PMT) with about 20 % quantum efficiency at 313 nm. While the EMCCD camera produces an image with spatial resolution mainly used for optimizing the alignment of the laser beams, the PMT is connected to the input of the experiment control system (cf. Sec. 4.8) to count single photon detection events. For alignment of the image, the custom objective is mounted to a 3-axis translation stage based on linear piezo actuators with 5 nm resolution and position feedback[31].

Finally, to reduce the background signal during experiments, we place an iris in the first image plane and a UV bandpass filter[32] with 89 % transmission at 313 nm in front of the PMT and enclose the whole beam path in a tube system. At around saturation intensity and a detection time of 400 μs the average photon counts are typically around 21 photons/s. Following the Rayleigh criterion, the resolution of an almost identical imaging setup was determined to be $< 2\,\mu$m in the custom objective's focal plane [Ude15] and is sufficient to resolve individual ions of a two-ion crystal in our setup given the typical ion-ion-distance of $\sim 8\,\mu$m (multi-layer trap) and $\sim 9\,\mu$m (single-layer trap).

4.7 Microwave setup

For the required quantum logic operations on our qubit transition as well as general state manipulation we need in total three microwave drives all of which are depicted in Fig. 4.22. The carrier drive is connected to the microwave conductor of the ion trap labeled MWC_2 (cf. Fig. 5.1) and is used to produce an oscillating magnetic field at the ion position in order to carry out spin-flip operations on hyperfine transitions of the $^2S_{1/2}$ manifold with frequencies ranging between 850 and 1400 MHz (cf. Sec. 3.4). The signal generation starts with a DDS unit whose frequency and phase are controlled via our experiment control (cf. Sec. 4.8). Producing sine waves of frequencies up to 500 MHz, the DDS output is at first frequency-quadrupled [Gro14] and subsequently

[28] Thorlabs, PF1-0-03-F01
[29] Andor, DU-885K-C00-VP
[30] Hamamatsu Photonics, H8259-01
[31] PI, N-472.210
[32] Thorlabs, FGUV11-UV

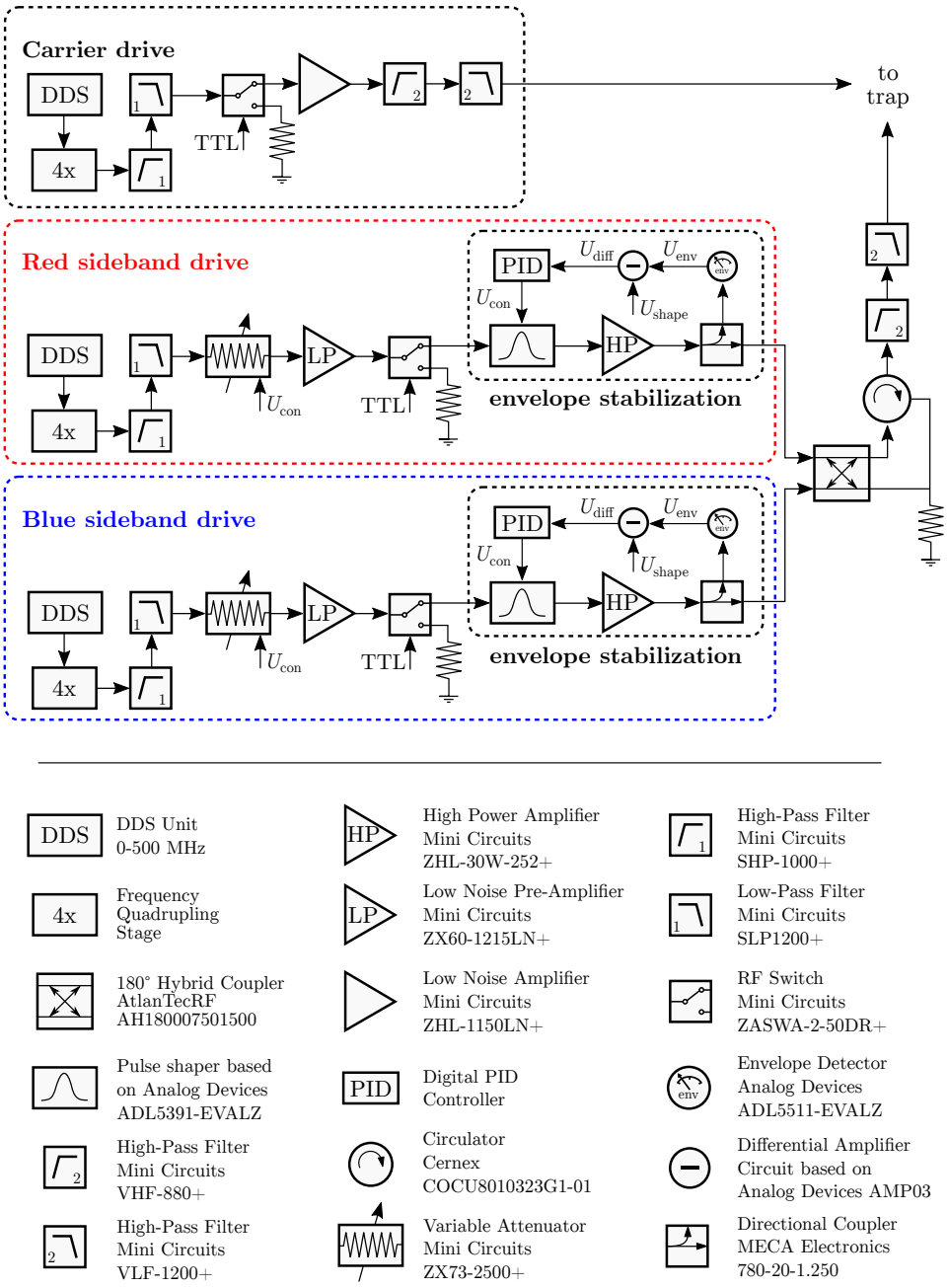

Figure 4.22: Microwave setup for driving carrier transitions between 853-1764 MHz and motional sidebands around 1082.55 MHz.

bandpass filtered with a low-pass and high-pass filter in series. After a TTL-controlled rf switch and a low-noise broadband amplifier, the signal is routed to the trap assembly via a SMA feedthrough of the feedthrough flange (cf. Fig. 4.2).

The red and blue sideband drives are both connected to the microwave conductor labeled MWM and are used to each produce an oscillating magnetic near-field gradient at the ion position suitable for driving motional sidebands on the qubit transition at $\omega_0 \simeq 1082.55\,\mathrm{MHz}$. If turned on simultaneously, both drives can also be used to perform multi-qubit gates based on the Mølmer-Sørensen interaction. As for the carrier drive, the signal generation starts with a DDS unit, a frequency quadrupling stage and a bandpass filter whereas the signal amplitude can be adjusted via the control voltage U_{con} of a voltage controlled attenuater. After passing a low-noise pre-amplifier and a TTL-controlled rf switch, the microwave signal is fed into the envelope stabilization circuit including a multiplier for pulse shaping and a high power broadband amplifier (cf. Sec. 4.7.1 for details on the envelope stabilization). The amplified red and blue sideband signals are combined in a 180° hybrid coupler and pass a subsequently connected 3-port circulator in order to suppress any effect of possible back-reflection from the transmission line on the forwarded microwave signal. Finally, the signal is again bandpass filtered and routed to the ion trap. The output spectrum of each sideband drive is shown in Fig. 4.23. In future experiments, the spectral purity of the sideband drives could be improved by a custom line filter after the hybrid coupler [Sep16].

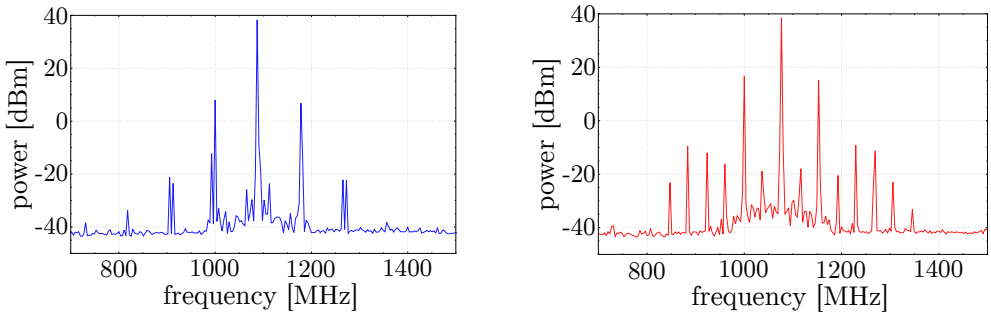

Figure 4.23: Output spectrum of the blue (left) and red (right) sideband drive when set to their respective frequency used for sideband cooling and the gate ($f_{\mathrm{BSB}} \simeq 1088.8\,\mathrm{MHz}$ and $f_{\mathrm{RSB}} \simeq 1076.2\,\mathrm{MHz}$). Both spectra were obtained by connecting a spectrum analyzer to the combined output of the sideband drives with just one sideband drive turned on. The multiple peaks are caused by frequency mixings of the DDS set frequency and its 1 GHz clock in the quadrupling stage.

4.7.1 Microwave envelope stabilization

The envelope stabilization is used to stabilize the high power amplifier output of each sideband drive to a time-dependent reference waveform [BWB+13] with voltage U_{shape} as shown in Fig. 4.22. The stabilization circuit starts by sampling $-20\,\text{dB}$ of the amplifier output via a directional coupler and feeding the sampled signal into an envelope detector[33]. Here, the detector's output voltage $U_{\text{out}} = U_{\text{env}} + U_{\text{ref}}$ is given by the sum of the corresponding envelope signal U_{env} and the detector's internal reference voltage U_{ref}. After a first differential amplifier circuit[34] to subtract the reference voltage and obtain the pure envelope voltage, the signal is fed into a second differential amplifier circuit in which the reference waveform voltage U_{shape} is subtracted from U_{env}. The resulting difference voltage $U_{\text{diff}} = U_{\text{env}} - U_{\text{shape}}$ is used as an input of a digital PI controller [HMF+18] with 14-bit resolution. The feedback loop is closed by routing the controller's output voltage U_{con} to the input of a multiplier-based[35] pulse shaper [Gro12].

In the experiment, the envelope stabilization circuit serves two main purposes. On the one hand, it is used to adiabatically shape the otherwise rectangular microwave sideband pulses after the rf switch with a $2\,\mu$s long cumulative error function. On the other hand, it suppresses the infidelity contribution of a fluctuating differential AC Zeeman shift during multi-qubit operations due to amplitude noise on the two sideband pulses. Fig. 4.24 shows a pulse-shaped blue sideband pulse after the envelope stabilization with parameters comparable to the ones used for the gate experiments in Sec. 5.3. The envelope signal was measured after the high power amplifier using the envelope detector and the differential amplifier circuit as shown in Fig. 4.22. The error function of the reference waveform at the beginning and end of the pulse was set to $2\,\mu$s while the flat pulse part between them has a length of about $808\,\mu$s. Averaged over 210 pulses, we find the envelope for both sideband to vary about $0.04\,\%$ of the flat part's mean after $38\,\mu$s, corresponding to a power variation of $0.08\,\%$ with respect to the flat part's mean power. To determine the performance of the envelope stabilization for future experiments and pulse shapes, an oscillating sine-wave with known amplitude $A_{\text{ref}} = 2\,\text{V}_{\text{pp}}$ and frequency f_{ref} is applied to the reference waveform input of the circuit while U_{env} is monitored as a function of f_{ref}. The bandwidth of the circuit is defined as the frequency at

[33] Analog Devices, ADL5511-EVALZ
[34] based on Analog Devices, AMP03
[35] Analog Devices, ADL5391-EVALZ

which U_{env} has decreased by 3 dB with respect to its initial value at $f_{\mathrm{ref}} \simeq 0$ Hz and was found to be $\simeq 618$ kHz (see Fig. 4.25).

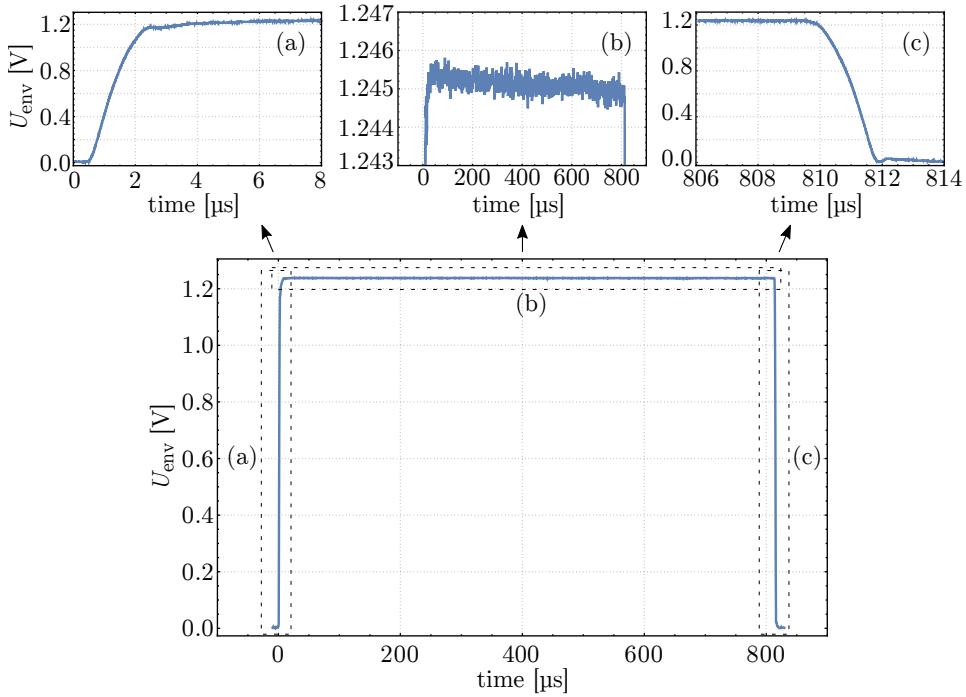

Figure 4.24: Bottom: envelope stabilized blue sideband pulse produced by the blue sideband drive as shown in Fig. 4.22. The error function used for pulse-shaping at the beginning (a) and end (c) of the pulse is about 2 μs long. The flat part (b) is about 808 μs long and corresponds to an applied microwave power of 37.4 dBm.

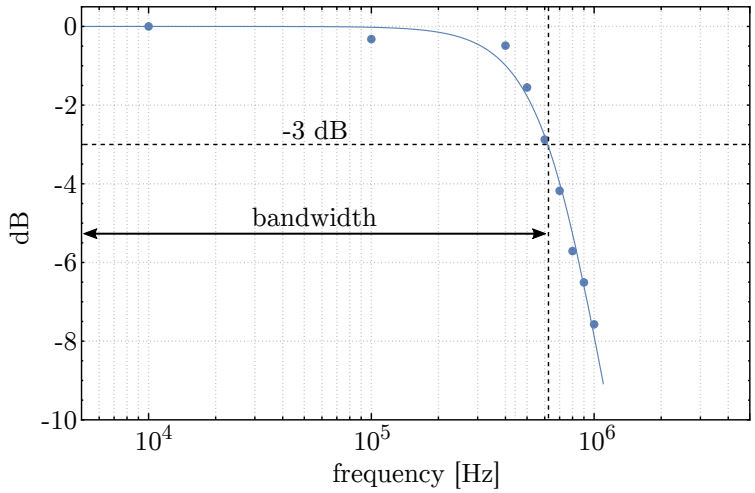

Figure 4.25: Bandwidth measurement of the envelope stabilization circuit as explained in the main text. A fit indicates a bandwidth of around 618.841 kHz.

4.8 Experiment control system

The experiment control system used in this thesis is based on hardware and software developed in the Ion Storage Group of the National Institute of Standards and Technology (NIST) [Lan06] and ported to Windows 7 and Visual C++ 2010 as explained in [Gro12]. The hardware is based on a field-programmable gate array (FPGA) with a 62.5 MHz clock[36] and includes 16 TTL outputs, 2 PMT counter inputs and 8 direct digital synthesizer (DDS) channels.

The TTL signals are mainly used for microwave and laser signal switching and have a minimum TTL pulse length of 48 ns and an amplitude of 3.3 V. One of the PMT inputs is connected to the PMT used in the imaging system (cf. Sec. 4.6) and enables access to the average photon counts during experiments. The DDS units are controllable in phase and frequency and mainly serve as RF sources for the microwave drives and laser AOMs. They have a 1 GHz clock and produce sinusoidal output signals up to 500 MHz.

As mentioned in Sec. 4.7.1 and 4.3.2, we use arbitrary waveform generators [BWB+13, Bow15] to produce time-dependent voltage waveforms for pulse-shaping as well as 10 DC trap voltages for axial ion confinement. The waveform generators are based on 16-bit digital-to-analog converters (DACs) with 50 MHz update rate and a voltage range of ±10 V. The waveforms are based on splines and are stored on the boards beforehand using a USB connection. Time-dependent signals are synchronized via a TTL input. For further details see [Lan06, Gro12].

[36] PLL synthesized from a 10 MHz signal generated by a hydrogen maser

Chapter 5

Single-layer ion trap

This chapter includes all experiments performed in the single-layer ion trap called ConsTrap and constitutes the main part of the experimental work of this thesis. The chapter begins with an introduction of the trap and continues with a description of the trap assembly as well as the ion loading procedure. Following a brief explanation of the used method for minimizing micromotion, the near-field pattern of the microwave conductor intended for driving sideband transitions is analysed in a Ramsey-type experiment utilizing a single ion as a local field probe. After a presentation of the sideband cooling and heating rate results employing the new established Raman beamline, the near-field pattern of the embedded conductor is used to demonstrate microwave sideband cooling of a radial motional mode as well as an entangling two-qubit gate in a MS protocol. The chapter concludes with an explanation of all characterization experiments involved in the numerical error analysis of the gate operation as well as a presentation of the derived error budget.

5.1 The trap

5.1.1 Electrode layout

The ConsTrap is a room-temperature, microfabricated, single-layer surface-electrode (SE) ion trap which has been designed to enable multi-qubit gates utilizing the microwave near-field approach [OLA+08]. The overall electrode layout is based on a previous SE trap design developed in our group [Wah16]

and includes several small design changes such as a new RF electrode shape to further decrease axial micromotion and a higher ion-to-electrode distance to alleviate the entangling gate error induced by motional heating. The central electrode layout of the trap is sketched in Fig. 5.1 and consists of 10 DC electrodes, one split RF electrode, one meander-like microwave conductor (MWM) and two additional microwave conductors routed around the central DC electrodes (DC_3 and DC_8).

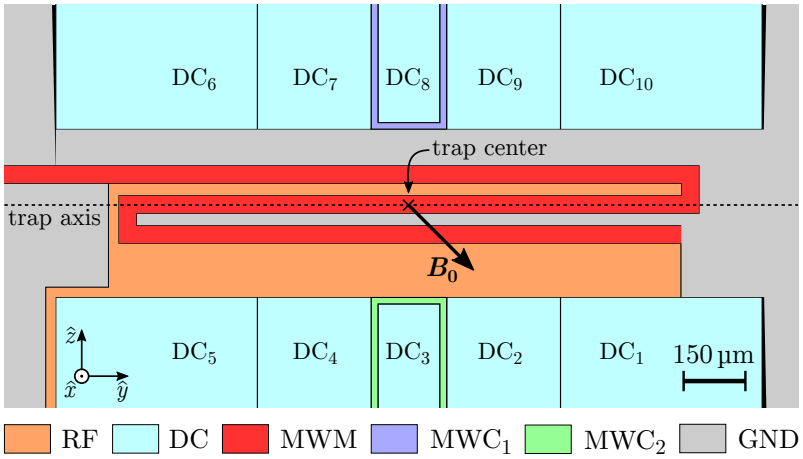

Figure 5.1: Central electrode layout of the ConsTrap ion trap. The ions are confined 70 μm above the indicated trap center using one split RF electrode and 10 DC control electrodes. The meander-shaped microwave conductor labeled MWM is used to drive motional sideband transitions as well as two-qubit entangling gates. Global spin state manipulation of the ions is carried out using the field pattern generated by the microwave conductor MWC_2. The remaining microwave conductor labeled MWC_1 is a backup for MWC_2 and remains unused in this thesis. Figure reproduced from [HZS+19].

While the DC and RF electrodes are dedicated to axially and radially confine the ions about 70 μm above the trap surface as outlined in the following section, the microwave conductors are designed to enable microwave quantum logic operations. For global spin state manipulation, we apply a microwave current to the microwave conductor labeled MWC_2 which produces an oscillating magnetic field amplitude at the ion position. Typical Rabi frequencies are given in Tab. 3.2. In contrast, applying a current to the MWM conductor generates an oscillating magnetic near-field gradient at the ion position suitable for driving motional sideband transitions or multi-qubit gates. The overall electrode layout has been optimized employing the finite element simulation model detailed in [Wah16]. Here, the optimization criterion was to result in

a MWM field pattern producing a high oscillating field gradient (with linear polarization and projection along the quantization axis) and low-residual fields at the RF null position[37].

5.1.2 Secular frequencies

For confining the ions in the radial $\hat{x}\hat{z}$-plane, we apply an RF voltage at 88.2 MHz with an adjustable amplitude to the RF resonator while all remaining electrodes are held at RF ground. Axial confinement along the $\hat{y}$-direction (trap axis) is then provided by applying $\mathrm{DC}_{1-10} = \{0.618, 0.055, 0.120, 1.200, -4.652, -2.017, 4.938, -6.831, 5.470, -5.921\}$ V to the respective DC electrodes. In order to enable efficient Doppler cooling of all motional modes, the potential has been calculated using the gapless plane approximation [OM01, Wes08] to result in an axial trap frequency of 1.1 MHz and to rotate the high-frequency radial mode (otherwise perpendicular to the trap surface) by about 25° with respect to the $\hat{x}$-axis.

Experimentally, we measure the resulting secular frequencies by applying an oscillating 'tickle' voltage to DC_2 and observing the fluorescence of the ion as a function of the tickle frequency. Once it is resonant with a motional mode frequency, the ion heats up and the ion fluorescence reduces due to the Doppler effect. Following this procedure, we determine the axial mode frequency of a single ion to be $\omega_{\mathrm{ax}} = 2\pi \times 1.1$ MHz and the radial LF and HF mode frequencies to be around ~ 6.4 MHz with a relative frequency splitting between 30 and 42.5 kHz depending on experimental conditions and the applied potentials. When calculating the radial mode frequencies back through our simulation model, we find best agreement for an RF voltage of $\sim 76\,\mathrm{V}_{0-\mathrm{peak}}$ which is approximately consistent with the expected value of $\sim 83\,\mathrm{V}_{0-\mathrm{peak}}$ following the coaxial resonator calculations (cf. Fig. 4.11) and the measured RF power of ~ 16 dBm. Given the simulated RF voltage of $\sim 76\,\mathrm{V}_{0-\mathrm{peak}}$, we can calculate the total electric potential $\phi_{\mathrm{total}} = \phi_{\mathrm{RF}} + \phi_{\mathrm{DC}}$ in the radial plane as shown in Fig. 5.2 resulting in an intrinsic trap depth of about 28 meV.

However, even though all mode frequencies are in acceptable agreement with our simulations, the quite similar Rabi frequencies of both radial modes observed during the sideband cooling experiments (cf. Sec. 5.2.2) indicate an HF mode rotation of $\sim 40°$ with respect to the $\hat{x}$-axis rather than the simulated

[37] Further details on the simulations about the ConsTrap design will be published in the PhD thesis of Giorgio Zarantonello. The simulation software is Anysy HFSS 17.2.

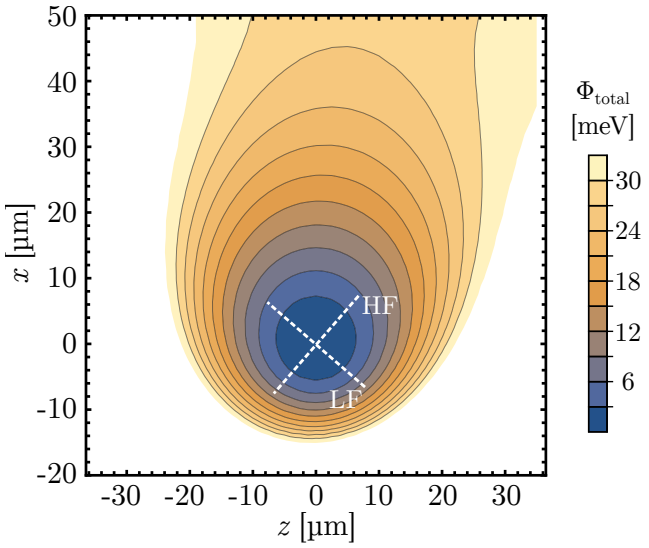

Figure 5.2: Simulated total electric potential ϕ_{total} in the radial plane based on the conditions given in the text. The plot axes are with respect to the RF null position at which the potential is smallest. The intrinsic trap depth is defined as the saddle point of the potential while the dashed lines indicate the estimated orientations of a single ion's LF and HF radial mode based on measurements.

$\sim 25°$. Potential reasons for this mismatch are electric stray fields which alter the potential at the ion position and have also been observed in a stronger way in other surface traps [WOC+13a].

5.1.3 DC shim fields

In order to displace the ions in the radial plane as needed for a measurement of the magnetic near-field gradient (cf. Sec 5.1.8) or minimizing excess micromotion in the radial plane (cf. Sec. 5.1.7), we superimpose the DC voltages for axial confinement with additional DC shim voltages on the order of a few mV. Similar to [WOC+13a], the directions of radial displacement are chosen along the two orthogonal axes for which the projection of the micromotion amplitude along the BD beam direction is maximized and minimized, respectively.

5.1.4 Fabrication

The fabrication of the ConsTrap follows the Single Level Processing (SLP) method as sketched in Fig. 5.3 and was carried out by Amado Bautista-Salvador at the cleanroom facility at Physikalische-Technische Bundesanstalt (PTB), Braunschweig. Further details including a multi-layer extension of the

SLP method can be found in [BSZH+19].

The fabrication process starts with the preparation of an aluminum nitride (AlN) substrate which is coated with a 15 nm thin titanium (Ti) adhesion layer and 50 nm thin gold (Au) seed layer using resistive evaporation (Fig. 5.3 (a)). While the Ti layer serves as an adhesion promoter, the Au seed layer itself serves as the conductive layer for electrodeposition. The electrode layout is defined by optical lithography comprising spin coating of a 16 μm thick negative photoresist on top of the Au seed layer and a subsequent illumination with UV light using contact lithography (i.e. the photoresist mask is in direct contact with the photoresist). After the development of the resist, the defined areas on the substrate are filled up to the desired thickness performing Au electroplating in a sulphite-based bath (Fig. 5.3 (b)). Subsequently, the mask is chemically removed and the substrate is cleaned via oxygen-based plasma etching. Finally, the initial Au seed and Ti adhesion layers are removed via argon (Ar) etching and fluorine-based plasma etching, respectively, as shown in Fig. 5.3 (c).

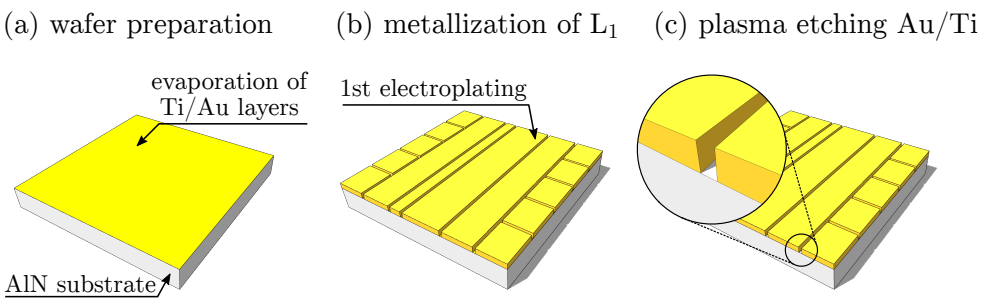

Figure 5.3: Simplified fabrication flow of the ConsTrap following the SLP method detailed in [BSZH+19]. The cartoon picture only illustrates the fabrication process and does not represent the layout of the installed trap.

5.1.5 Trap assembly

The trap is glued onto an oxygen-free high thermal conductivity (OFHC) copper holder using epoxy[38] in order to ensure good thermal conductivity and is surrounded by a custom printed circuit board[39] which is made of CuNiPdAu coated Rogers 4350B (see Fig. 5.4). In the following, this printed circuit

[38] Epoxy Technology Inc., EPO-TEK H74
[39] Contag AG

board will also referred to as the 'filterboard'. Its layout can be found in Appendix A.2.

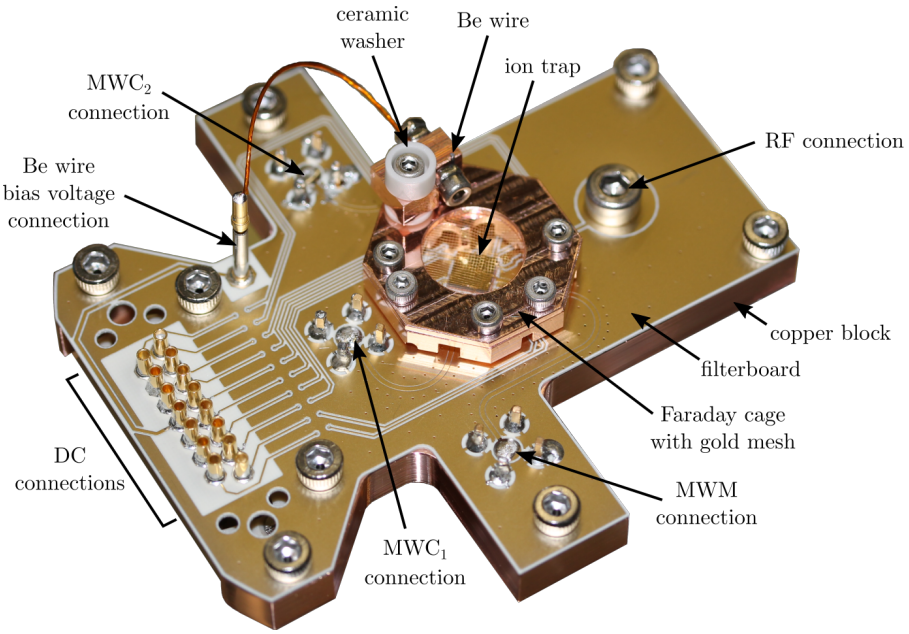

Figure 5.4: Photograph of the complete trap assembly including the filterboard, the Faraday cage and the copper block. The D-sub pins and SMA jacks are facing towards the backside of the filterboard. The copper block has pockets for RC filter elements soldered on the PCB's backside and a through hole to connect the RF pin of the resonator via a screw.

DC signals are connected to the filterboard via a 15-pin D-sub connector[40] and are each filtered by an RC filter consisting of a 1 kΩ resistor[41] and a 820 pF capacitor[42]. Here, the capacitors are placed close to the trap itself in order to establish a good ground connection of the DC electrodes for the trap RF. The resulting filter cut-off frequency is about $f_c \simeq 194\,\mathrm{kHz}$ (see Sec. 4.3.2 for more details). While the feedline for the trap RF is connected to the pin of the coaxial resonator with a screw, the external microwave signal connections are established via three custom SMA jacks made of Au-coated OFHC[43]. The SMA jacks and D-sub pins are connected to SMA and D-sub feedthroughs of the vacuum flange located at the backside of the assembly (cf. Fig. 4.2)

[40] Allectra, 212-PinF-25
[41] Barry Industries, RP0603BA-1001JN-91
[42] Novacap, 0603N821J101P
[43] Cinch Connectivity Solutions, 142-0701-491 (insulator and conductor pin)

using commercial SMA I-connectors[44] and a set of stacked D-sub adapters[45]. The feedlines of the three microwave signals leading to the trap are designed to be 50 Ω co-planar waveguides at the qubit frequency. Gold wire bonds connect all signal feedlines with the corresponding trap electrodes. A picture of the bonded trap, including the number of wire bonds used for the different electrodes, is shown in Fig. 5.5.

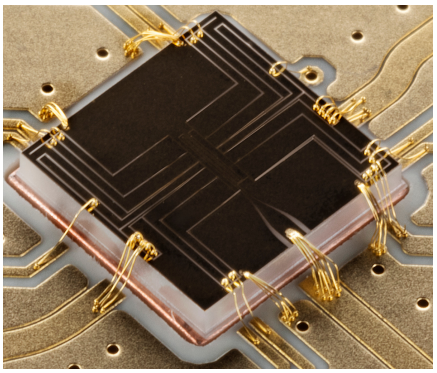

electrode	# wire bonds
DC	1
RF	3
MWC_1, MWC_2	4
MWM	10
ground	20

Figure 5.5: Photograph of the ConsTrap wire-bonded to a surrounding printed-circuit board used for connectivity, signal routing and filtering. The trap size is about $5 \times 5\,\mathrm{mm}^2$. The table on the right summarizes the number of wire bonds for the respective electrodes. Trap ground is connected to the common ground of PCB and vacuum chamber. The dark color of the electrodes is caused by an optical filter used for the photograph.

The Faraday cage around the trap consists of a gold mesh above the trap (through which the fluorescence is detected) and a copper frame with slits to all 6 unblocked viewports of the octagon vacuum chamber for laser access. While the Faraday cage is held at ground potential to shield the trap from ambient electronic noise as well as stray potentials from the partly dielectric viewports, the Be wire holder (see Fig.5.4) is isolated from the Faraday cage by a pair of ceramic washers and can thus be biased with a voltage during ion loading (cf. Sec. 5.1.6). The whole trap assembly is placed in a vacuum setup at room temperature as sketched in Fig. 5.6 and has a combined capacitance of 3.28 pF following the resonator measurements outlined in Sec. 4.3.1.1.

[44] Amphenol Corporation, SMA2071A1-3GT50G-50 (seal rings are removed)
[45] Allectra GmbH, 211-FS15-PK and 211-MS15-PK

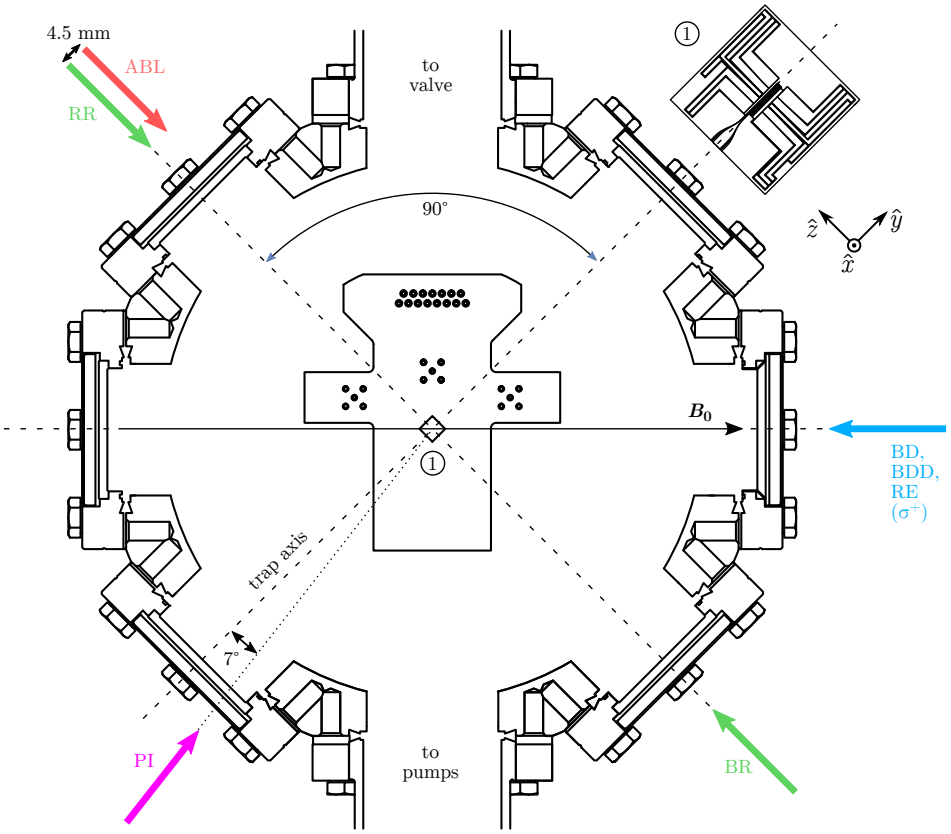

Figure 5.6: Orientation of the trap assembly inside the vacuum chamber including laser beam configuration. The trap axis has an angle of 45 ° to the quantization axis defined by the bias field $\boldsymbol{B_0}$. The inset labeled '1' shows a magnification of the ion trap at the center. The BD and BDD beam are used during state detection and Doppler cooling while the PI and ABL beam are needed for ion loading. The two Raman beams BR and RR are utilized to drive motional sideband transitions on the qubit and are purely aligned in the trap's radial plane. During sideband cooling and state preparation, the RE beam is used as a repumper.

5.1.6 Ion loading

The ion loading scheme in this work is an evolved version of the scheme described in [Wah16] and is based on laser ablation of a Be target using a Q-switched Nd:YAG pulse laser[46] at 1064 nm and subsequent photo-ionization from the ablation plume using a continuous wave laser at 235 nm (cf. Sec. 4.4). The procedure and beam configuration is explained in the following and illustrated in Fig. 5.7 (a). The output beam (diameter: 3 mm) of the pulsed laser (ABL; red) is focused by an $f = 200$ mm lens onto a Be wire target (diame-

[46] Continuum, Minilite I

ter: 0.5 mm, distance to trap center: 12 mm) to generate an ablation plume of beryllium atoms (Be; green) via laser ablation. For alignment purposes, the Be wire and the pulsed laser beam position can be monitored through a hole in the Faraday cage using a CCD camera. The ablation plume is collimated and directed towards the trapping region by a ∅1 mm aperture in the Faraday cage where the angle between the ABL beam and the directed plume is 27°. In the trapping region, neutral Be atoms can be ionized by the photo-ionization laser (PI; purple) focused to a diameter of $\sim 40\,\mu$m. As the direct laser access along the trap axis is blocked by wire bonds connecting the filterboard and the microwave conductor MWM, the PI beam forms an angle of 7° with the trap axis. The resulting angle between PI beam and directed ablation plume of 110° represents a compromise between the smallest possible Doppler-broadening during the ionization process at 90° and the ABL beam not passing above the trap to avoid potential damage. Once ionized, the $^9Be^+$ ions are Doppler cooled by two laser beams (BD,BDD; blue) around 313 nm (cf. Sec. 3.3) and are captured by the potential generated by the trap electrodes. The full sequence and pulse durations of the involved laser beams is shown in Fig. 4.14 (b). With a typical pulse energy of the ABL beam of ~ 2.3 mJ and a PI beam power of around $400\,\mu$W, each run of the loading sequence results in one to two trapped ions.

In comparison with the loading scheme presented in previous work [Wah16], the main differences of the scheme described here are given by the following two modifications. The first one is the replacement of a mechanical shutter with an AOM in the PI beamline (cf. Sec. 4.4) to enable vibration-free and faster beam switching. As a result of the limited exposure of the trap with deep-UV light, the temporary produced patch potentials due to the PI beam in the trap (the main cause of non-controllable radial mode frequency drifts in our experiment) could be significantly reduced. Second, as shown in Fig. 5.4, the Be wire is electrically connected to a D-sub pin and supplied with a bias voltage of +10 V from our DC setup during the loading sequence. Here, the supplied voltage is expected to deflect the trajectory of charged particles which are unintentionally produced in the ablation plume. As this partially prevents the charged particles from reaching the trap, it also reduces their uncontrolled creation of patch potentials. For demonstration experiments of ablation loading schemes in microfabricated traps, see [HGH$^+$07, LCL$^+$07].

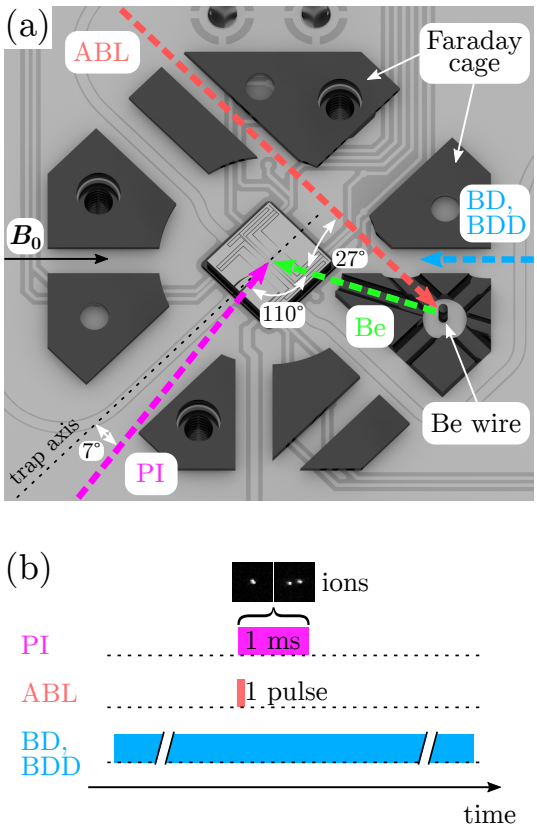

Figure 5.7: Ion loading procedure involving beams for photo-ionization (PI; purple), Doppler cooling (BD,BDD; blue) and laser ablation (ABL; red). The ablation plume of beryllium (Be; green) is directed towards the trap center. See main text for details. (a) Laser beam configuration and trap assembly around the ion trap (center) including part of the filterboard and a cross-section of the Faraday cage to highlight its through-holes for laser access. (b) Sequence and duration of the laser beam pulses. The number of trapped ions after the sequence depends on the ABL pulse energy and the PI beam power.

5.1.7 Micromotion compensation

If the pseudopotential of the ion trap is non-zero at the ion position, the ion undergoes an additional motion at the RF drive frequency $\Omega_{\mathrm{RF}} = 2\pi \times f_{\mathrm{RF}}$ called micromotion. While this motion always leads to undesirable effects like Doppler shifts, one generally distinguishes between two kinds of micromotion. The first one is called 'intrinsic' micromotion and is caused by residual RF field amplitudes resulting from the trap design itself [BMB+98]. For the ConsTrap electrode layout and the parameters given in Sec. 5.1.1, we expect this kind of micromotion to result in a micromotion amplitude along the $\{\hat{x}, \hat{y}, \hat{z}\}$ direction

of $\{6.346, 0.005, 0.001\}$ nm.

The second kind is caused by undesirable static electric fields which shift the ion out of the minimum of the intrinsic micromotion in the trap center. In surface-electrode ion traps such fields can for example originate from electric stray potentials due to charging of dielectric materials of the trap. As these static fields can usually be nulled by applying DC shim potentials, this micromotion is typically referred to as 'excess' micromotion.

In the experiment, we minimize excess micromotion in the radial plane by utilizing the near-field gradient of the MWM conductor to drive micromotion sidebands on selected hyperfine transitions of the electronic ground state as outlined in [WOC+13a]. Briefly summarized, the method can be described as follows.

May $\boldsymbol{r_{\mathrm{MM}}} = (x_{\mathrm{MM}}\mathbf{e_x} + z_{\mathrm{MM}}\mathbf{e_z})\cos(\Omega_{\mathrm{RF}}t)$ be the radial micromotion and f_{HFS} the transition frequency of the selected transition. When applying a microwave magnetic field gradient of frequency $f_{\mathrm{HFS}} + f_{\mathrm{RF}}$, the ion in its rest frame experiences a field of frequency f_{HFS} and amplitude

$$\hat{\boldsymbol{B}}_{\mathbf{MM}} = \frac{1}{2}B' \begin{pmatrix} \cos(\beta_{\mathrm{MM}}) & \sin(\beta_{\mathrm{MM}}) \\ \sin(\beta_{\mathrm{MM}}) & -\cos(\beta_{\mathrm{MM}}) \end{pmatrix} \begin{pmatrix} x_{\mathrm{MM}} \\ z_{\mathrm{MM}} \end{pmatrix} \tag{5.1}$$

where β_{MM} is the magnetic quadrupole orientation and B' denotes the near-field gradient. The resulting Rabi rate Ω_{MM} of the micromotion sideband is proportional to $\left|\hat{\boldsymbol{B}}_{\mathbf{MM}}\right|$ and hence, to the micromotion amplitude $|\hat{\boldsymbol{r}}_{\mathbf{MM}}|$. Consequently, we can minimize excess micromotion by displacing the ion via DC shim fields in the radial plane and determining the position for which the Rabi rate is smallest.

In general, any radial micromotion will result in an amplitude $\hat{\boldsymbol{B}}_{\mathbf{MM}}$ which can be decomposed in projections $B_{\parallel}$ or $B_{\perp}$ on $\boldsymbol{B_0}$ and thus, can be sensed using either a $\Delta m_F = 0$ or $\Delta m_F = 1$ transition. However, for sufficiently large angles θ_0 between the radial plane and the quantization field, also a single $\Delta m_F = 1$ transition can be employed as any orientation of $\hat{\boldsymbol{B}}_{\mathbf{MM}}$ results in a non-negligible $B_{\perp}$ component.

In our setup, this requirement is fulfilled ($\theta_0 = 45°$) enabling the excess micromotion minimization only via transition A. Here, the lowest Rabi frequency for a micromotion sideband-induced carrier transition for any orientation of $\hat{\boldsymbol{B}}_{\mathbf{MM}}$ can be calculated by [OLA+08]

$$\Omega_{\mathrm{MM}} = \frac{1}{2}\frac{B'}{\sqrt{2}}\,|\hat{\boldsymbol{r}}_{\mathbf{MM}}|\,\frac{\mu}{2\hbar} \tag{5.2}$$

where μ denotes the corresponding matrix element of transition A and $1/\sqrt{2}$ is the geometric factor representing the smallest possible $B_\perp$ projection. Assuming a gradient of $B' = 18.8\,\mathrm{T/m}$ (cf. Tab. 5.1) and a detection sensitivity on a micromotion sideband of $\Omega_{\mathrm{MM}} \times t_p = \pi/10$, this translates in a resolvable micromotion amplitude of about 0.4 nm for a drive time of $t_p = 2\,\mathrm{ms}$. In the following section, we use the derived RF null position as a reference to measure the resulting near-field pattern of the MWM conductor.

5.1.8 Microwave near-field gradient characterization

In order to characterize the oscillating magnetic near-field pattern of the MWM conductor around the RF null position, we measure its induced AC Zeeman shift on selected hyperfine transitions in the $^2S_{1/2}$ manifold as a function of radial ion displacement. To this end, we employ a Ramsey sequence which has been developed in [WOC+13a] and is shown in Fig. 5.8. For a generic hyperfine transition $|a\rangle \leftrightarrow |b\rangle$ with transition frequency ω_0, it can be described as follows.

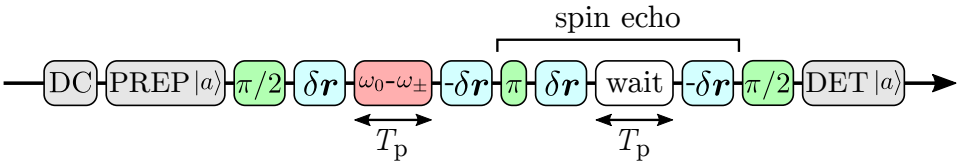

Figure 5.8: Pulse sequence to measure the magnetic fields of the MWM conductor at the ion position via phase accumulations from the corresponding AC Zeeman shifts. The indicated spin echo reduces the sensitivity to magnetic field fluctuations on time scales that are slower than the typical time of an individual experiment of around 400 μs.

First, we prepare the ion in state $|a\rangle$ and apply a resonant[47] $\pi/2$ pulse to produce a superposition of $|a\rangle$ and $|b\rangle$. Following this, we displace the ion in the radial plane by $\delta\boldsymbol{r}$ using suitable DC shim potentials (cf. Sec. 5.1.1) and subsequently off-resonantly excite the MWM conductor for a variable time T_p at frequency $\omega_0 - \omega_\pm$. Here, any oscillating magnetic field produced by the MWM conductor at the ion position induces an AC Zeeman shift on $|a\rangle \leftrightarrow |b\rangle$ and hence, causes the superposition to accumulate an additional phase. Finally, we move the ion back to the initial position (i.e. move the ion by $-\delta\boldsymbol{r}$), apply a second $\pi/2$ pulse resonant with $|a\rangle \leftrightarrow |b\rangle$ and detect the population

[47] Resonant to the transition $|a\rangle \leftrightarrow |b\rangle$.

in $|a\rangle$ via fluorescence detection. By observing population oscillations as a function of T_p, we can determine the phase accumulation per time and thus the AC Zeeman shift.

As performing a single experiment like this allows to measure the residual oscillating magnetic field at a specific ion position, repeating the experiment for multiple positions enables the construction of a magnetic field 'map' in the radial plane and hence, to infer the magnetic field distribution produced by the MWM conductor.

In the experiment, we investigate the induced AC Zeeman shifts on hyperfine transitions which depend differently on the residual field polarization in order to obtain complementary information. More specifically, we excite the MWM conductor at a frequency 10 MHz blue-detuned from the qubit transition and measure the induced AC Zeeman shifts on transition Q and C, resulting in $|a\rangle \equiv |1,1\rangle \leftrightarrow |b\rangle \equiv |2,1\rangle$ and $|a\rangle \equiv |1,0\rangle \leftrightarrow |b\rangle \equiv |2,0\rangle$, respectively. Here, the induced shift on transition Q mostly depends on the π component of the magnetic field at the ion position while for transition C also the σ^- and σ^+ field components contribute approximately equally [Wah16]. Consequently, the resulting data sets of both transitions have a visual difference as shown in the left column of Fig. 5.9.

As the near-field pattern of the MWM conductor is expected to follow a quadrupole-like shape, we can fit the experimental data sets to the 2D quadrupole model developed in [WHZ+17] in order to extract its relevant field properties. Neglecting derivatives of the magnetic field higher than the first one, a 2D magnetic quadrupole can be fully described by

$$\boldsymbol{B} = \mathfrak{Re}\Big\{ e^{i\omega t}\Big[B\left(\mathbf{e}_\alpha \sin\psi - i\mathbf{e}_{\alpha-\pi/2}\cos\psi\right) + B'\left(\mathbf{Q}_\beta \cos\psi + i\mathbf{Q}_{\beta-\pi/2}\sin\psi\right)\mathbf{r}\Big]\Big\} \quad (5.3)$$

where

$$\boldsymbol{r} = \begin{pmatrix} x \\ z \end{pmatrix}, \mathbf{e}_\alpha = \begin{pmatrix} \cos\alpha \\ \sin\alpha \end{pmatrix} \quad \text{and} \quad \mathbf{Q}_\beta = \begin{pmatrix} \cos\beta & \sin\beta \\ \sin\beta & -\cos\beta \end{pmatrix} . \quad (5.4)$$

Here, B and B' indicate the strength of the residual magnetic field and the gradient, respectively, with α and β denoting their rotation angle with respect to the $\hat{z}$-axis, and ψ characterizes the relative angle between the real and imaginary part of the gradient (i.e. its polarization). In order to use the model on the experimental AC Zeeman shift data, we insert $\boldsymbol{B}$ into the theoretical

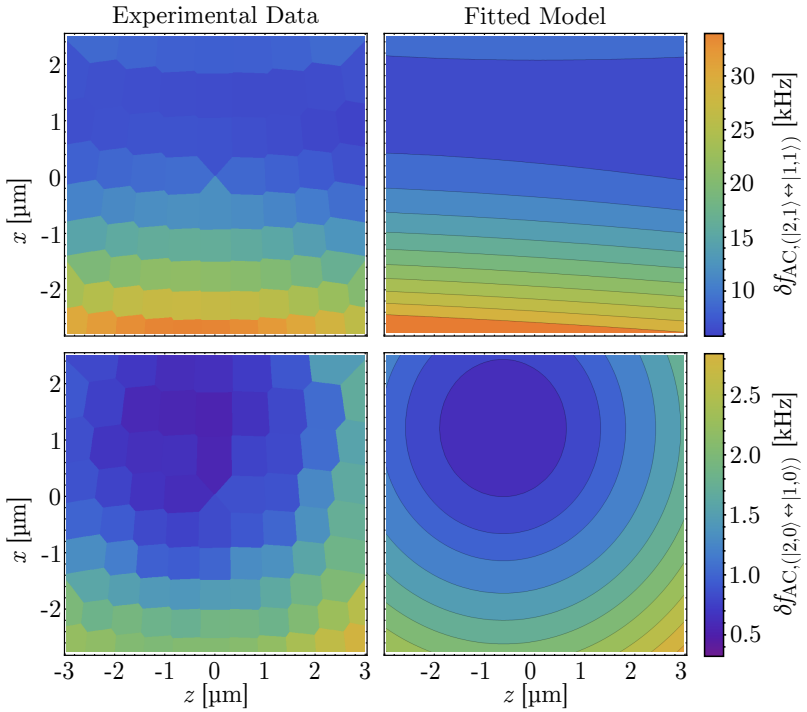

Figure 5.9: Absolute AC Zeeman shifts δf_{AC} induced on a single ion by the resulting near-field pattern of the MWM conductor as a function of radial position (x, z). The left column shows the resulting shifts on transition Q (top) and C (bottom) where each data point was obtained as illustrated in Fig. 5.8. The applied microwave power is $\sim 37.4\,\mathrm{dBm}$. The right column gives the corresponding result of a joint fit of the experimental data to a 2D quadrupole model. The x and z coordinate are with respect to the RF null position which is calculated to be about $70.6\,\mu\mathrm{m}$ above the chip surface using the gapless plane approximation.

function to calculate the AC Zeeman shift [WHZ+17], thus obtaining a new function which depends on the five parameters of the model. Leaving all of these parameters as fit parameters, a joint least-square fit of the data to this new function yields the values listed in Tab. 5.1. Here, we have substituted $\boldsymbol{r} \to \boldsymbol{r} - (x_0, z_0)^{\mathrm{T}}$ in Eq. 5.3 as the local field minimum is not located at the origin. Hence, x_0 and z_0 are additional fit parameters which are appended to the table.

Based on the fitted values we can conclude the following properties of the resulting quadrupole field of the MWM conductor. First, the gradient B' is, as expected from our simulations, mainly linearly polarized (ψ small) and almost aligned with the $\hat{x}$-axis ($\beta \approx 90°$). Second, for an applied microwave power of $\sim 37.4\,\mathrm{dBm}$ we achieve a magnetic field gradient of $19\,\mathrm{T/m}$ and a residual magnetic field at the local field minimum of the quadrupole of about $35\,\mu\mathrm{T}$

Parameter	B	B'	α	β	ψ	x_0	z_0
Unit	[μT]	[T/m]	[°]	[°]	[°]	[μm]	[μm]
Fitted value	35.5	18.85	84.7	87.61	3.97	1.21	-0.56
Fitted error	0.9	0.23	9.1	1.24	1.32	0.04	0.55

Table 5.1: Quadrupole parameters obtained by fitting the AC Zeeman shift data in Fig. 5.9 with the 2D quadrupole model in Eq. 5.3 as explained in the text. The underlying data is obtained for an applied microwave power at the MWM conductor of $\sim 37.4\,\mathrm{dBm}$.

corresponding to a power independent ratio of $B/B' = 1.88\,\mu\mathrm{m}$. Third, the local minimum of the quadrupole field is shifted by about $(1.21, -0.56)\,\mu\mathrm{m}$ with respect to the RF null position where we perform our experiments. Here, a possible reason for the mismatch might be due to back reflections of the applied microwave currents along the microwave lines of MWC_1 and MWC_2 which, in turn generate oscillating magnetic fields and hence, affect the original field pattern [Wah16, HZBS$^+$18]. Finally, based on the fitted gradient and the assumed orientation of the HF mode (i.e. $\sim 40°$ with respect to the $\hat{x}$-axis), we approximate the needed time for a two-qubit 1-loop MS gate to be around $t_g \sim 540\,\mu\mathrm{s}$ which, given the results in Sec. 5.3, is in reasonable good agreement with our observations.

5.2 Cooling results

5.2.1 Doppler cooling

In our experiment, Doppler cooling is performed on the closed cycling transition ${}^2S_{1/2}\,|F=2, m_F=2\rangle \leftrightarrow {}^2P_{3/2}\,\left|m_J=\frac{3}{2}, m_I=\frac{3}{2}\right\rangle$ by applying the red-detuned BD and BDD beams as outlined in Sec. 3.3. As the ions are confined in a harmonic well and the wave vector $\boldsymbol{k}$ of the BD beam has non-zero projections on all vibrational modes (cf. Fig. 5.6), laser cooling is accomplished in all three dimensions. Here, the Doppler temperature in the weak binding regime ($\gamma \gg \omega_j$) can be approximated as $T_D \simeq \hbar\gamma/(2k_B) = 0.47\,\mathrm{mK}$ where $\gamma = 2\pi \times 19.4\,\mathrm{MHz}$ is the natural linewidth of the closed cycling transition, $\hbar$ is the reduced Planck constant and k_B is the Boltzmann constant [WIBH87]. The energy of the ion in each mode can be expressed as $\bar{E}_j \simeq k_B T_D = \hbar\omega_j\,(\bar{n}_j + 1/2)$ where $\bar{n}_j$ is the mean phonon number of the corresponding motional mode with angular frequency ω_j. Hence, the mean phonon number at the Doppler limit is given by [WIBH87]

$$\bar{n}_j = \frac{1}{2}\left(\frac{\gamma}{\omega_j} - 1\right). \tag{5.5}$$

Based on this equation, the expected mean phonon numbers for typical trap frequencies in our setup after Doppler cooling calculate to $\bar{n} \sim 8$ for the axial mode ($\omega_{\mathrm{ax}} = 2\pi \times 1.1\,\mathrm{MHz}$) and $\bar{n} \sim 1$ for the radial modes ($\omega_{\mathrm{LF}} \simeq \omega_{\mathrm{HF}} \simeq 2\pi \times 6.4\,\mathrm{MHz}$). However, it should be noted that in practice these values are based on an overestimated cooling performance as, for example, the reduced cooling rate due to the angle between $\boldsymbol{k}$ and the respective mode is not considered.

Fig. 5.10 shows a comparison of the blue sideband (BSB) and red sideband (RSB) of a single ion's low-frequency (left) and high-frequency (right) radial mode in the Doppler cooled state as observed using the Raman beams. The two data sets were obtained following the steps:

1. Doppler cooling
2. State preparation $|2,2\rangle \rightarrow |\downarrow\rangle$
3. Measure the excitation probability $P_{|\uparrow\rangle}$ (i.e. the probability to find the ion in $|\uparrow\rangle$) for each radial mode after applying a 1st order RSB or BSB pulse of fixed length as a function of relative Raman laser detuning Δf

The data sets of each radial mode are jointly fitted to Eq. 5.7 and include the respective neighboring radial mode in the fitting procedure as outlined in Sec. 5.2.2. Inserting the obtained excitation probabilities of the sidebands in Eq. 5.8 results in a mean phonon number of the LF and HF mode after Doppler cooling of $\bar{n} \simeq 1.34$ and $\bar{n} \simeq 1.74$, respectively. We note that an analysis of the axial mode's mean phonon number was not possible as our Raman laser beams are purely aligned in the radial plane. However, we do not consider the calculated $\bar{n}$ of the axial mode to cause problems within the scope of this thesis.

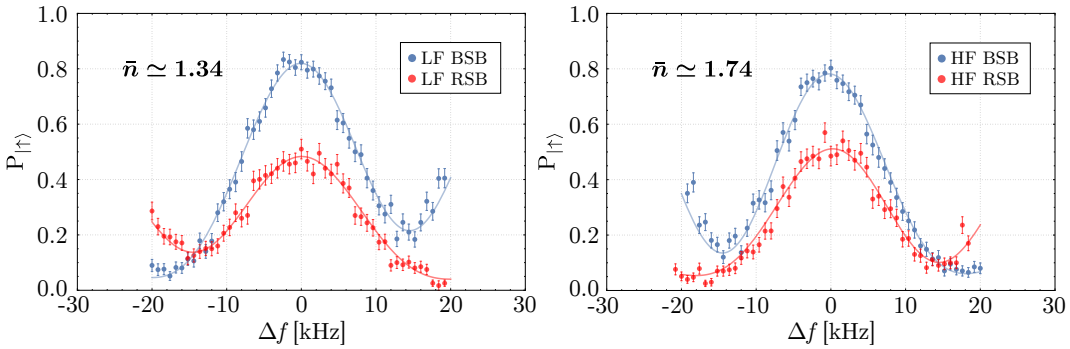

Figure 5.10: Comparison of the 1st order BSB and RSB of the LF (left) and HF (right) radial mode of a single ion after Doppler cooling using the Raman beams. The frequency detuning in each data set is given relative to the respective radial mode frequency and is in both cases $\sim 6.4\,\mathrm{MHz}$. The probe times for the LF and HF mode are $50\,\mu\mathrm{s}$ and $55\,\mu\mathrm{s}$, respectively.

5.2.2 Single-ion Raman sideband cooling

Prior to some experiments we use pulsed Raman sideband cooling to cool the thermal distribution of specific motional modes near to the motional ground state. To this end, we employ two Raman beams (RR and BR) and one repumping beam (RE) whose respective beam directions and couplings to atomic transitions are summarized in Fig. 5.6 and 3.3, respectively. While the two Raman beams are used to induce motional sideband transitions, the repumper performs optical pumping within each sideband cycle, and hence provides the required dissipative process.

As introduced in Sec. 2.1, a relevant parameter when driving motional sideband transitions with optical radiation is the dimensionless Lamb-Dicke parameter which gives the ratio of the ion's wavepacket size $q_j^0 = \sqrt{\hbar/(2m\omega_j)}$

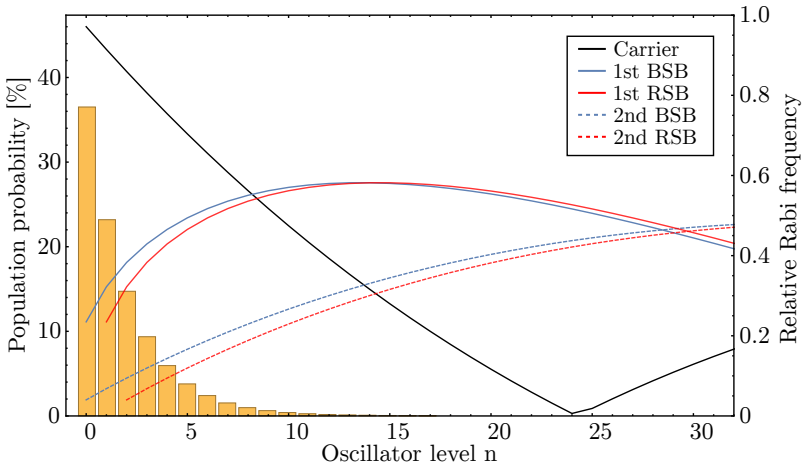

Figure 5.11: Simulated thermal population distribution of the HF radial mode after Doppler cooling and the corresponding relative Rabi frequencies of the carrier, 1st and 2nd order sideband transitions as a function of the oscillator level n. The Lamb-Dicke parameter and mean phonon number is $\eta_{\mathrm{HF}} \simeq 0.24$ and $\bar{n}_{\mathrm{HF}} \simeq 1.74$, respectively. Due to the comparable rotation angle, the simulated values for the LF mode are very similar.

in the ground state of motional mode j to the wavelength of the interacting light. For stimulated Raman transitions, it can be expressed as

$$\eta_j = \frac{2}{\lambda} \cos(\phi_j) \sin\left(\frac{\theta}{2}\right) \sqrt{\frac{h}{2m\nu_j}} \tag{5.6}$$

where m denotes the ion's mass, $\nu_j = \omega_j/(2\pi)$ is the frequency of the motional mode, $\theta \in [0, 180°]$ represents the angle between the wave vectors of the two Raman beams and $\phi_j \in [0, 90°]$ is the angle between the difference of these two wave vectors $\Delta\boldsymbol{k} = \boldsymbol{k}_1 - \boldsymbol{k}_2$ and the direction of the motional mode in question. In our experiment, the two Raman beams are counter-propagating (i.e. $\theta = 180°$) and result in a difference wave vector in the radial plane parallel to the trap surface. Hence, our beam configuration allows only to drive sideband transitions on motional modes in the radial plane. With $\lambda \approx 313\,\mathrm{nm}$, $\nu_{\mathrm{HF}} \simeq \nu_{\mathrm{LF}} \simeq 6.4\mathrm{MHz}$ as well as the assumed angles between $\Delta\boldsymbol{k}$ and radial modes of $\phi_{\mathrm{LF}} = 40°$ and $\phi_{\mathrm{HF}} = 50°$ (cf. Sec. 5.1.1), the Lamb-Dicke parameters for the LF and HF modes are $\eta_{\mathrm{LF}} \simeq 0.29$ and $\eta_{\mathrm{HF}} \simeq 0.24$ respectively. Based on these values, we can calculate the Rabi frequencies of the carrier, 1st and 2nd order sideband transitions as a function of the harmonic oscillator level n as exemplary shown for the HF mode in Fig. 5.11. Given the measured mean phonon number of both radial modes after Doppler cooling and the associated

thermal population distribution, it appears feasible to only employ 1st RSB transitions during the ground state cooling sequences of both radial modes. The full Raman sideband cooling procedure for one radial mode is listed below and results in the ion in $|2,2\rangle$ with the chosen mode near the motional ground state.

1. Doppler cooling
2. State preparation $|2,2\rangle \rightarrow |\downarrow\rangle$
3. Apply a Raman laser pulse of length t_p on the 1st RSB of the chosen motional mode to drive the transition $|\downarrow\rangle |n\rangle \rightarrow |\uparrow\rangle |n-1\rangle$
4. Carry out repumping scheme:
   (a) Apply an optical repumping pulse to drive the transition $|\uparrow\rangle \rightarrow {}^2P_{3/2} \left|m_J = \frac{1}{2}, m_I = \frac{3}{2}\right\rangle$ and thereby optically pump population from $|\uparrow\rangle$ to $|2,2\rangle$
   (b) Drive a π rotation on transition Q in order to clear out $|\downarrow\rangle$
   (c) Repeat (a) and (b) three times and add another optical repumping pulse at the end to fully prepare $|2,2\rangle$
5. Repeat step 2 to 4 with different times t_p to account for the varying π times of the different Fock states
6. Recollect the population lost to ${}^2S_{1/2}$ Zeeman sub states other than the qubit and $|2,2\rangle$ by sequentially transferring the population of each state to $|\uparrow\rangle$ and applying the repumping sequence (step 4)

Note that here we have introduced the repumping scheme which is used in step 4 and step 6 and is further discussed in Fig. 5.12.

In order to perform ground state cooling of both radial modes, we employ an interleaved sequence that alternates between the 1st RSB transitions of the chosen modes (step 3) while changing the interaction time t_p for each sideband pulse accordingly. The interleaved sequence is necessary as the ion recoil due to repumping pulses can affect the temperature of both modes. Fig. 5.13 shows the probability to detect the ion in $|\uparrow\rangle$ after preparing it in $|\downarrow\rangle$ and applying a RSB or BSB probing pulse of fixed length as a function of relative Raman detuning Δf. The result of each motional mode is fitted in a procedure in

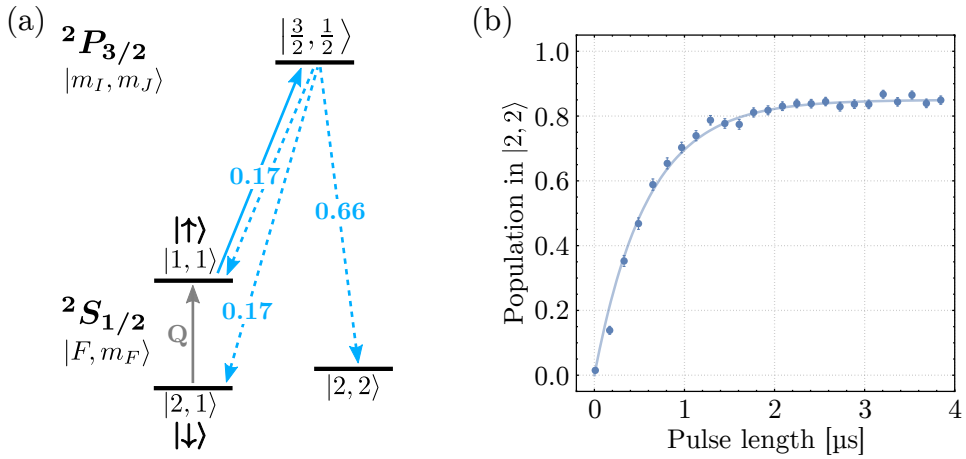

Figure 5.12: (a): Relevant level structure for the repumping scheme in step 4. The optical repumper (solid blue arrow) excites the electron from $|\uparrow\rangle$ to the excited state in the $^2P_{3/2}$ manifold from where it can decay into three states (dashed blue arrows) with the indicated probabilities. After an optical repumping pulse, a microwave-induced π rotation can be applied to transition Q. (b): Evolution of the population in $|2, 2\rangle$ as a function of time the repumper beam is turned on. At 0 μs the population is fully prepared in $|\uparrow\rangle$ while the remaining population during the repumping pulse is trapped in $|\downarrow\rangle$.

which the corresponding RSB and BSB are jointly fitted by a function of the form [Hom06]:

$$\mathrm{P}_{|\uparrow\rangle}(\Delta f) = a + b\left[\frac{\Omega_{SB}^2}{2\left(\Omega_{SB}^2 + \Delta f^2\right)}\left\{1 - \cos\left(\sqrt{\Omega_{SB}^2 + \Delta f^2}\, t_p\right)\right\}\right.$$
$$\left. + \frac{\Omega_{SB}^2}{2\left(\Omega_{SB}^2 + (\Delta f + \delta_r)^2\right)}\left\{1 - \cos\left(\sqrt{\Omega_{SB}^2 + (\Delta f + \delta_r)^2}\, t_p\right)\right\}\right]. \tag{5.7}$$

Here, a is the baseline, b is the amplitude of the excitation, Δf is the laser detuning from the sideband transition, Ω_{SB} is the Rabi frequency, t_p is the laser interaction time and δ_r denotes the frequency difference between the radial mode in question and the respective neighboring radial mode[48]. In the fit procedure, a, b, Ω_{SB}, t_p were left free while we set $\delta_r = \pm 30\,\mathrm{kHz}$ depending on the sideband type and radial mode[49]. For a thermal state of the motion, as it is the case after Doppler cooling and any cooling to near the ground state,

[48] For simplification, we assume the neighboring mode to have the same Ω_{SB}.
[49] The radial mode splitting at the time of the experiment was $\simeq 30\,\mathrm{kHz}$.

the mean phonon number $\bar{n}$ of a motional mode can be calculated by

$$\bar{n} = \frac{\mathrm{P}_{|\uparrow\rangle,\mathrm{RSB}}/\mathrm{P}_{|\uparrow\rangle,\mathrm{BSB}}}{1 - \mathrm{P}_{|\uparrow\rangle,\mathrm{RSB}}/\mathrm{P}_{|\uparrow\rangle,\mathrm{BSB}}} \tag{5.8}$$

where $\mathrm{P}_{|\uparrow\rangle,\mathrm{RSB}}$ and $\mathrm{P}_{|\uparrow\rangle,\mathrm{BSB}}$ are the excitation probabilities of the RSB and BSB sideband, respectively [TKK+00]. Using the fitted peak excitations shown in Fig. 5.13, the mean phonon number of the LF and HF radial mode after the interleaved cooling sequence are $\bar{n}_{\mathrm{LF}} \simeq 0.13$ and $\bar{n}_{\mathrm{HF}} \simeq 0.12$ after a total sideband cooling time of around 2.5 ms. However, given these comparably high mean phonon numbers, we suspect that the sideband times have not been fully optimized yet and need further adjustments to achieve maximum cooling performance. Additional limiting factors are given by motional heating as well as the repumper sequence which, according to our simulations, scatters on average 1.5 photons per cycle. In the future, the cooling could also be improved by using 2nd order sideband pulses, even though our Lamb-Dicke parameter is relatively low.

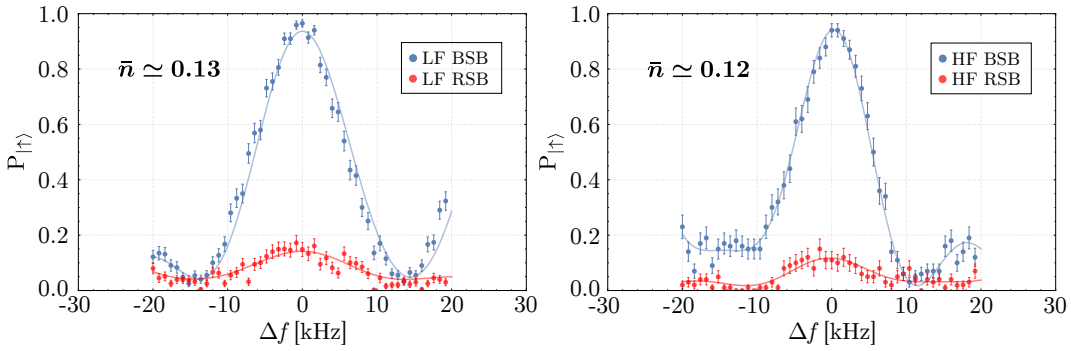

Figure 5.13: Comparison of the 1st RSB and 1st BSB excitation probability $\mathrm{P}_{|\uparrow\rangle}$ of a single ions LF (left) and HF (right) radial mode as a function of Raman laser detuning Δf relative to the corresponding sideband after performing an interleaved sideband cooling sequence on both radial modes. The data was obtained with a sequence composed of 30 RSB pulses for each mode while the sideband pulse lengths were experimentally optimized. The stated $\bar{n}$ is extracted based on the peak excitations of the fits (solid lines). The used probing times for the LF and HF mode are 65 μs and 75 μs, respectively.

Another way to verify 2D ground state cooling is Rabi flopping on the carrier transition where any population in $n > 0$ results in dephasing as the carrier Rabi frequency strongly depends on the oscillator level (cf. Fig. 5.11). Hence, Rabi oscillations on the carrier quickly decohere to half the excitation

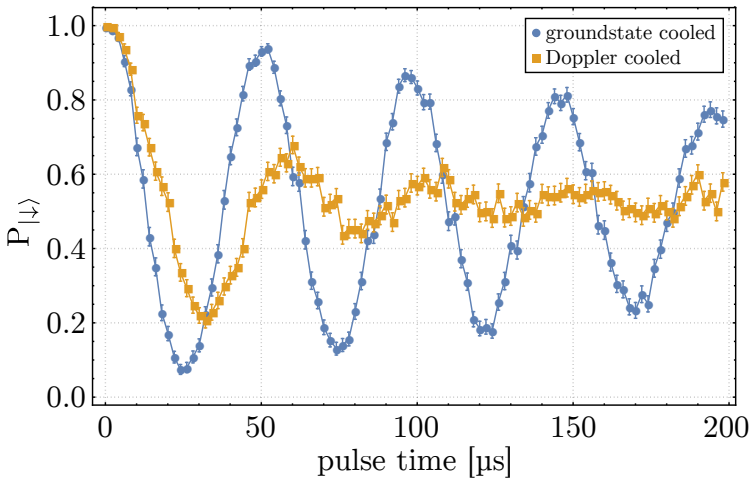

Figure 5.14: Rabi oscillations on the qubit carrier transition using the Raman beams. The orange data (squares) is taken after Doppler cooling while the blue data (disks) is measured after both radial modes are cooled near the motional ground state. A fit of an exponentially decaying sinusoid to the latter yields a $1/e$ decay time of $271 \pm 14\,\mu$s which is most likely limited by motional heating of the radial modes, imperfect ground state cooling and off-resonant photon scattering.

probability for a Doppler cooled ion while for a 2D ground state cooled ion several oscillations are observed, as shown in Fig. 5.14.

5.2.3 Single-ion heating rate measurements

After Doppler and Raman sideband cooling, the ions have a kinetic energy corresponding to a temperature well below the equilibrium temperature of the environment. Thus, leaving the cooled ion in the dark without laser cooling results in the ion to heat up with a rate which is determined by the electric-field noise spectral density at the ions' motional mode frequency [WMI+98]. Experimentally, one can deduce this quantity by measuring the mode's mean phonon number via sideband thermometry (cf. Sec. 5.2.2) as a function of waiting time without laser cooling, also known as the heating rate $\dot{\bar{n}}$. Fig. 5.15 depicts heating rate measurements of a single-ion's LF and HF radial mode at $\nu_{\mathrm{LF}} = 6.36\,\mathrm{MHz}$ and $\nu_{\mathrm{HF}} = 6.39\,\mathrm{MHz}$, respectively. Given the slope of a weighted linear fit to the data of each mode, the corresponding heating rates are $\dot{\bar{n}}_{\mathrm{LF}} = 117 \pm 6\,\mathrm{phonons/s}$ and $\dot{\bar{n}}_{\mathrm{HF}} = 122 \pm 12\,\mathrm{phonons/s}$. Based on these values, we can estimate the electric-field noise spectral density by [TKK+00]

$$S_E = \frac{4m\hbar\omega_j}{q_e^2}\,\dot{\bar{n}}_j \tag{5.9}$$

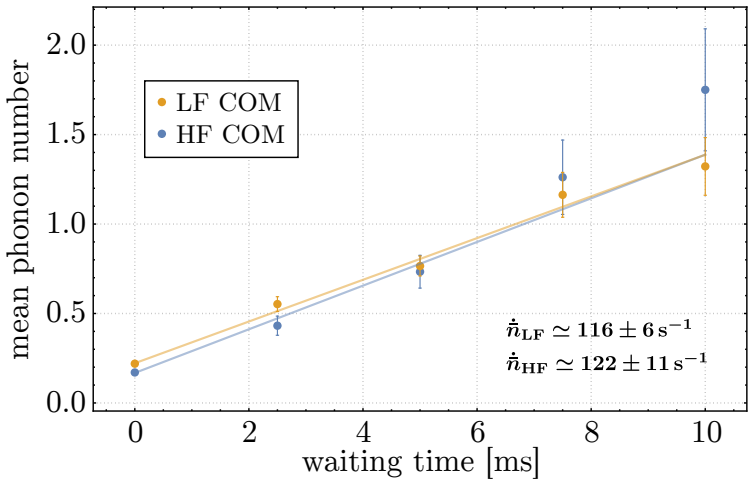

Figure 5.15: Heating rate measurements of a single ions radial LF and HF radial mode in which the mean phonon number is observed via sideband thermometry as a function of waiting time without cooling. For the experiments, both radial modes are cooled near the motional ground state using the Raman laser and an interleaved sideband sequence. The heating rates are determined by the slope of linear fits to the data which include the weights of the errors. The error bars of each data point are calculated from the errors of Gaussian fits to the sideband spectra employing error propagation through Eq. 5.8.

where m denotes the ion's mass, q_e is the elementary charge, $\nu_j = \omega_j/(2\pi)$ is the motional frequency of the mode considered and $\dot{\bar{n}}_j$ is the corresponding heating rate. Note that here we have neglected cross couplings between the trap rf and the noise field as they scale with ω_j^2/Ω_{RF}^2 (in our setup $\sim 10^{-3}$). For the LF and HF mode the extracted electric-field spectral noise density is about $1.1\times10^{-12}\,\mathrm{V^2m^{-2}Hz^{-1}}$ and $1.2\times10^{-12}\,\mathrm{V^2m^{-2}Hz^{-1}}$, respectively. The resulting product ωS_E for both modes is $\leq 7.7\times10^{-6}\,\mathrm{V^2m^{-2}}$ and shows good agreement with noise measurements in other traps reported in literature [DGB+14] given the nearest ion-to-electrode distance of $d \simeq 70\,\mu\mathrm{m}$ and the approximate scaling of $S_E \sim d^{-4}$ [DOS+06, SGS+18, BKW18].

5.2.4 Two-ion Raman sideband cooling and heating rate measurement

When two ions are held in the trap, the ion chain aligns along the weak trap axis (cf. Fig. 5.1) and the radial motional mode spectrum expands to two center-of-mass (COM) modes and two rocking modes as shown in Fig. 5.16. While the COM mode frequencies are given by the corresponding radial mode

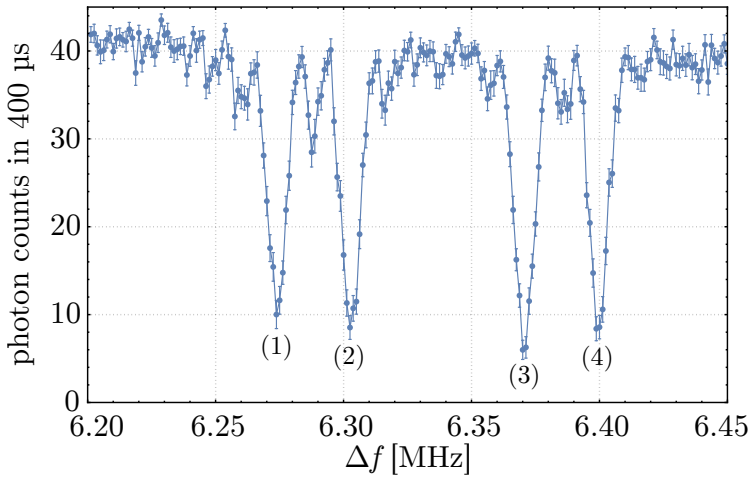

Figure 5.16: Typical 1st order BSB spectrum of all four radial modes of a two-ion crystal with $\omega_{ax} = 2\pi \times 1.1\,\mathrm{MHz}$ using a Raman frequency scan with respect to the qubit carrier. The photon counts on the $\hat{y}$-axis indicate the average photon counts for a detection time of $400\,\mu$s. Most experiments with two ions are carried out on the HF rocking mode labeled (2). The other modes are (1): LF rocking, (3): LF COM and (4): HF COM.

frequencies of a single ion, the frequency of the respective rocking mode can be calculated via $\omega_{\mathrm{rock}} = \sqrt{\omega_{\mathrm{COM}}^2 - \omega_{\mathrm{ax}}^2}$ as long as the condition $\omega_{\mathrm{ax}} < \omega_{\mathrm{rock}}, \omega_{\mathrm{COM}}$ is fulfilled.

In the following only the two rocking modes are considered as they typically show much lower heating rates compared to COM modes[50] and are hence more suitable for two-qubit gates in our setup. For two-ion rocking modes, the Lamb-Dicke parameter η_0 of the corresponding single ion mode reduces to $\eta_{\mathrm{rock}} = \eta_0/\sqrt{2}$ [MECZ99]. Hence, it appears again feasible to compose the Raman sideband cooling sequence for rocking modes of only 1st order RSB transitions like in the single-ion experiments (cf. Fig. 5.11).

Fig. 5.17 shows a sideband comparison of both rocking modes after employing an interleaved pulse sequence to cool both rocking modes simultaneously near the motional ground state. Here the cooling sequence for one rocking mode is composed of 20 RSB pulses and is identical to the single-ion procedure as listed in Sec. 5.2.2 when replacing $|\downarrow\rangle$ with $|\downarrow\downarrow\rangle$ and $|\uparrow\rangle$ with $|\uparrow\uparrow\rangle$. Again the RSB pulse lengths are optimized experimentally to result in the best cooling performance. Following [Web05, Hom06], the temperature analysis of

[50]The different heating rates originate from the differential ion motion for rocking modes which causes these modes to be excitable only by field gradients instead of by uniform fields like for COM modes [Jam98a, KWM+98].

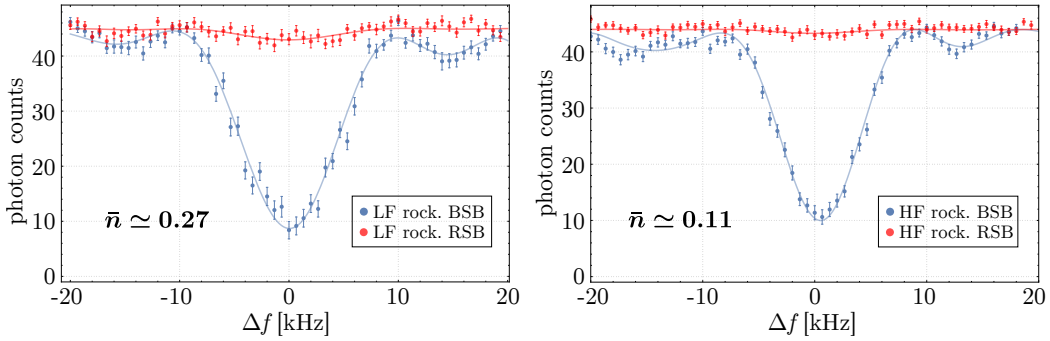

Figure 5.17: Sideband comparison of the two-ion LF rocking (left) and HF rocking (right) radial mode after an interleaved pulse sequence to cool both modes simultaneously. The x-axes indicate the Raman laser detuning Δf relative to the corresponding sideband while the y-axes give the average photon counts in 400 μs detection time. The raw histograms of the averaged photon counts enable the extraction of the probability to find the ions in $|\uparrow\uparrow\rangle$ after applying a RSB or BSB probing pulse of identical length and thus, allow the calculation of the corresponding $\bar{n}$ through Eq. 5.10. Probing times for the LF and HF mode are 95 μs and 118 μs, respectively. In both cases, the total sideband cooling time was about 3 ms.

two-ion modes differs from the single-ion scenario and requires the probabilities to find the ions in $|\uparrow\uparrow\rangle$ after applying a RSB and BSB pulse of identical length, given by $P_{|\uparrow\uparrow\rangle,\mathrm{RSB}}$ and $P_{|\uparrow\uparrow\rangle,\mathrm{BSB}}$. The ratio of both can then be related to the mean phonon number of a two-ion mode by

$$\frac{P_{|\uparrow\uparrow\rangle,\mathrm{RSB}}}{P_{|\uparrow\uparrow\rangle,\mathrm{BSB}}} = \left(\frac{\bar{n}}{\bar{n}+1}\right)^2 . \tag{5.10}$$

Experimentally, we can infer these probabilities by fitting a sum of Poisson distributions (cf. Sec. 3.5) to the raw histograms of the averaged photon count data of each sideband shown in Fig. 5.17. Solving Eq. 5.10 for $\bar{n}$ and inserting the peak excitation probabilities as obtained from a subsequent fitting procedure, we calculate a mean phonon number of the LF and HF rocking mode after sideband cooling of $\bar{n}_{\mathrm{LF,rock}} \simeq 0.27$ and $\bar{n}_{\mathrm{HF,rock}} \simeq 0.11$, respectively. However, it shall be noted that an accurate measurement of $\bar{n}$ using Eq. 5.10 is difficult for small ratios $P_{|\uparrow\uparrow\rangle,\mathrm{RSB}}/P_{|\uparrow\uparrow\rangle,\mathrm{BSB}}$ and hence, the given mean phonon numbers might only represent an upper bound [Web05].

To measure the corresponding heating rates, we prepare the mode in question near the motional ground state and determine $\bar{n}$ as a function of waiting time during which the ions can heat up. The result for the HF rocking mode is shown in Fig. 5.18 and indicates $\dot{\bar{n}}_{\mathrm{HF,rock}} \simeq 28 \pm 5\,\mathrm{phonons/s}$ based on the slope of a weighted linear fit to the data set.

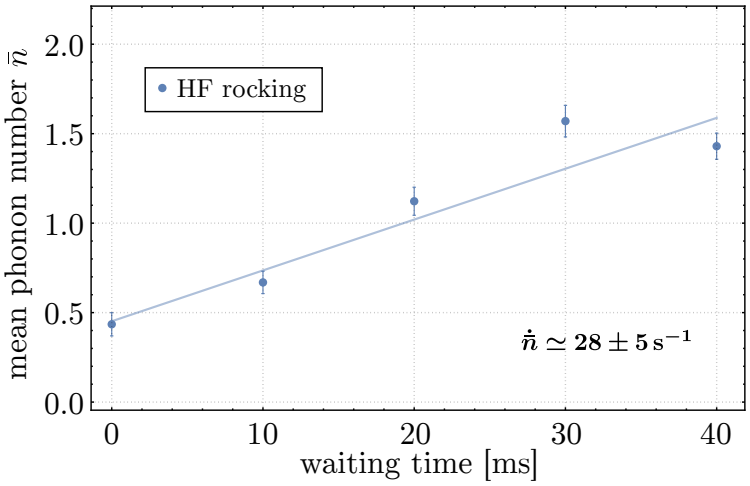

Figure 5.18: Heating rate measurement of the two-ion HF rocking mode. The error bar of each data point is calculated using the errors of a Gaussian fit to the excitation probabilities and performing error propagation through Eq. 5.10. The indicated $\dot{\bar{n}}$ is determined from the slope of a linear fit (solid line). As the data was taken before the sideband cooling sequence was further optimized, the initial mean phonon number is slightly higher than the one extracted from Fig. 5.17.

5.2.5 Single-ion microwave sideband cooling

To illustrate the potential of the near-field approach beyond entangling gates, we perform microwave sideband cooling of a Doppler cooled single-ion radial mode using the resulting field pattern of the MWM conductor. The sideband cooling procedure is identical to the one used during Raman sideband cooling when replacing the optical RSB pulses (step 3 in Sec. 5.2.2) with microwave-driven RSB pulses. Fig. 5.19 shows a sideband comparison of the radial LF mode (left column) and HF mode (right column) after Doppler cooling (top row) and an additional microwave cooling sequence (bottom row). While each mode is cooled in a separate experiment, the sideband cooling sequence comprises 6 RSB pulses of length 100 - 350 μs for both modes resulting in a total sequence time of 1.8 ms. The envelope of each microwave pulse is shaped with

a 2 μs long cumulative error function using the microwave envelope stabilization (cf. Sec. 4.7.1) where the flat part of the pulses corresponds to an applied microwave power of $\sim 5.5\,\mathrm{W}$. At this power level, the residual magnetic fields at the ion position induce AC Zeeman shifts on the order of 10 - 20 kHz with respect to the unperturbed sideband frequencies.

As in the Raman sideband cooling experiments, we measure the mean phonon number for each cooling condition via sideband thermometry. In the Doppler cooled state, we find the mean phonon number of the LF and HF mode to be $\bar{n}_{\mathrm{LF}} \simeq 1.59$ and $\bar{n}_{\mathrm{HF}} \simeq 1.7$, respectively, which is in good agreement to the measurements using optical beams. After applying the sideband cooling sequence, the mean phonon numbers of the LF and HF mode reduce to $\bar{n}_{\mathrm{LF}} \simeq 0.39$ and $\bar{n}_{\mathrm{HF}} \simeq 0.32$, respectively. Most likely, the final mean phonon number is limited by the comparably low number of RSB pulses used in the sequence. However, cooling attempts with more pulses have not been performed in order to limit the dissipated microwave power in the trap electrodes to a conservative level. Concerning the axial motional mode, microwave sideband cooling is not possible as the resulting near-field gradient of the MWM conductor along the trap axis is designed to be zero. For other implementations of microwave sideband cooling, see [OWC+11, WRW+15, SGWW18, SBS+19].

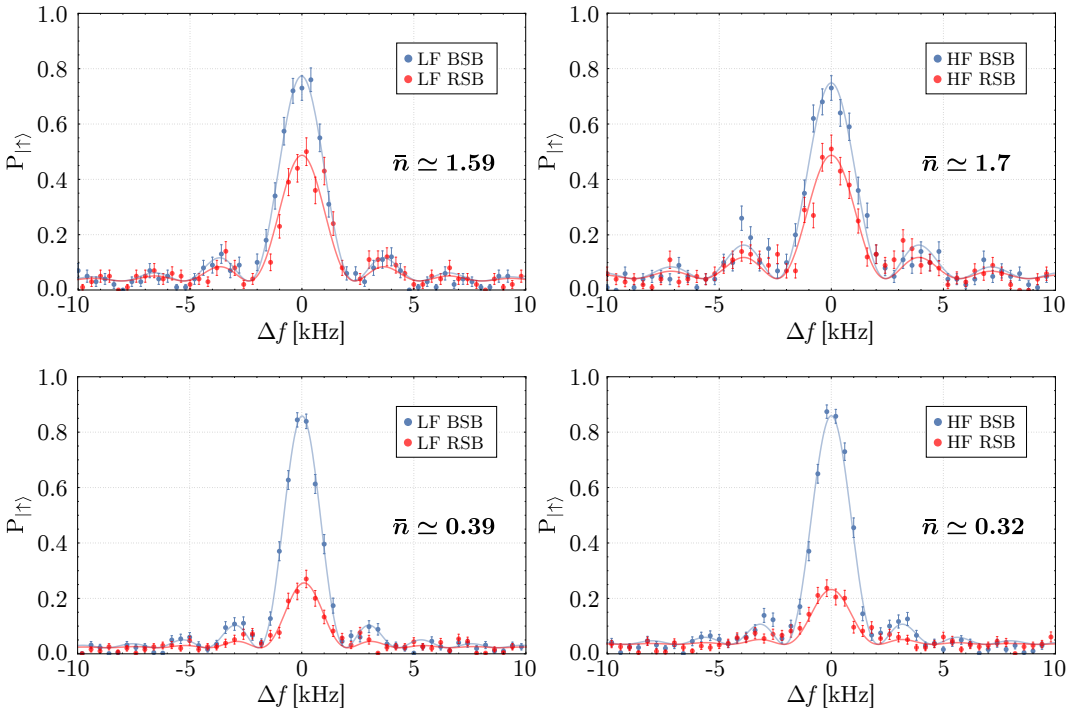

Figure 5.19: Excitation probabilities of a single ion's LF (left column) and HF (right column) radial mode as a function of microwave frequency detuning from the corresponding mode. The top row is obtained after Doppler cooling while the bottom row is obtained after applying a microwave sideband cooling sequence of 6 RSB pulses using the near-field gradient of the MWM conductor. Based on the π times of the blue sidebands after cooling the respective mode near the motional ground state, we measure the microwave Rabi frequencies for the LF and HF mode to be $\Omega_{\mathrm{LF}}/(2\pi) = 1.11\,\mathrm{kHz}$ and $\Omega_{\mathrm{HF}}/(2\pi) = 1.16\,\mathrm{kHz}$, respectively.

5.3 Two-qubit gate

The following section discusses the demonstration of a two-qubit Mølmer-Sørensen (MS) gate of 98.2±1.2% fidelity using the magnetic near-field gradient of the MWM conductor. Besides a description of the experimental gate implementation, the section comprises the fidelity measurement and a presentation of the error budget based on numerical simulations with experimental input parameters. The content of this section coarsely follows reference [HZS+19].

5.3.1 Gate parameters

The experimental sequence to drive the entangling gate starts with the standard preparation of Doppler-cooled ions, Raman sideband cooling of both radial rocking modes and a subsequent initialization of the ions in $|\uparrow\uparrow\rangle$ using a π rotation on transition A. The resulting thermal states of the LF and HF rocking modes are $\bar{n}_{\mathrm{LF,rock}} \simeq 0.27$ and $\bar{n}_{\mathrm{HF,rock}} \simeq 0.11$, respectively, while both radial COM modes are left in the Doppler cooled state. As the HF rocking mode is expected to have a lower heating rate than the two COM modes and, additionally, exhibits the highest projection on the resulting near-field gradient of the MWM conductor, we chose this mode for the gate operation. The radial mode frequencies are measured to be $(\omega_{\mathrm{LF,rock}}, \omega_{\mathrm{HF,rock}}, \omega_{\mathrm{LF,COM}}, \omega_{\mathrm{HF,COM}}) \simeq 2\pi \times (6.275, 6.318, 6.374, 6.416)\,\mathrm{MHz}$ while the axial mode is at $\omega_{\mathrm{ax}} \simeq 1.1\,\mathrm{MHz}$.

To perform the gate operation and ideally prepare the maximally entangled state $|\Psi\rangle$ (cf. Eq. 2.43), we apply a bichromatic microwave pulse to the MWM conductor using the blue and red sideband drive of the microwave setup described in Sec. 4.7. Here, the envelope of each sideband pulse is shaped with a $2\,\mu\mathrm{s}$ long cumulative error function at the beginning and end of the pulse (cf. Sec. 4.7.1). The frequency components of the bichromatic pulse are set to

$$\omega_{\mathrm{RSB}} = \omega_0 + \Delta_z - (\omega_{\mathrm{HF,rock}} + \delta_{\mathrm{g}}) \tag{5.11}$$

$$\omega_{\mathrm{BSB}} = \omega_0 + \Delta_z + (\omega_{\mathrm{HF,rock}} + \delta_{\mathrm{g}}) \tag{5.12}$$

where $\omega_0 \simeq 2\pi \times 1082.55\,\mathrm{MHz}$ is the qubit frequency, δ_{g} is the gate detuning and Δ_z denotes the differential AC Zeeman shift of the unperturbed qubit transition. For an applied microwave power of $\sim 5.5\,\mathrm{W}$ (37.4 dBm) in each tone we measure $\Delta_z/(2\pi) = 4.37\,\mathrm{kHz}$ and a resulting gate Rabi frequency of $\Omega_{\mathrm{g}}/(2\pi) = 1.071\,\mathrm{kHz}$. In order to optimize the gate, we fix the gate pulse duration $t_{\mathrm{g}} = \pi\sqrt{K}/\Omega_{\mathrm{g}}$ to the expected value based on the gate Rabi frequency

and subsequently scan for the detuning resulting in the highest preparation fidelity of $|\Psi\rangle$ (cf. Sec. 2.5.1). Following this procedure, we find an optimal gate time and gate detuning of $t_g = 808\,\mu$s and $\delta_g/(2\pi) = 3.4\,$kHz, respectively, corresponding to $K = 3$ loops in phase space.

Here, the observed mismatch of δ_g to the theoretically ideal detuning $\delta/(2\pi) = 3.71\,$kHz was tracked back to two effects: The first is a systematic frequency offset in the frequency measurement of $\nu_{\mathrm{HF,rock}} = \omega_{\mathrm{HF,rock}}/(2\pi)$ via the tickle method prior to the gate operation and is likely caused by the disturbing tickle fields at the ion position[51]. Following a frequency scan around zero detuning, we estimate this effect to be on the order of 100 - 200 Hz. The second one is an observed linear frequency 'chirp' of the radial mode frequency of about $0.3\,\mathrm{Hz}/\mu$s during the gate pulse itself which seems to be inherent to warm-up processes in the trap structures [Sep16]. This hypothesis is supported by an observed saturation behavior of the effect at around 1 ms (see Sec. 5.3.3.1 for further details). Consequently, the impact of the 'chirp' on the gate detuning can be reduced by preceding the gate with a warmup pulse. However, as we desired to keep the dissipated microwave power below a threshold equivalent to a 1.2 ms long gate pulse with 37.4 dBm in each sideband, the length of the warmup pulse was limited to $400\,\mu$s, leaving a mismatch contribution of the chirp to the gate detuning of about $(0.3\,\mathrm{Hz}/\mu\mathrm{s} \times 600\mu s)/2 \simeq 90\,$Hz. The full pulse sequence of the gate, including the warmup pulse, is illustrated in Fig. 5.20.

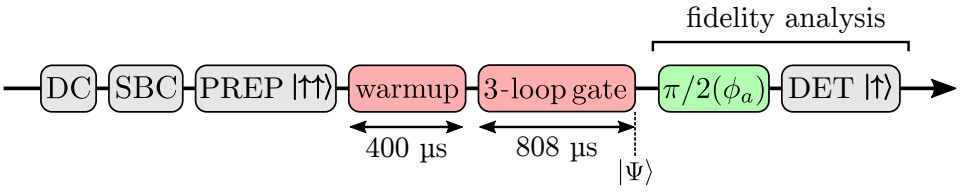

Figure 5.20: Pulse sequence of the two-qubit gate operation and the subsequent fidelity analysis of the ideally prepared state $|\Psi\rangle$.

[51] This could be due to (a) the fact that the tickle excites the motion of the ion(s) to potentially higher excursions than used during the gate which, through trap potential anharmonicities, would lead to a different observed effective motional frequency, and (b) an additional pseudopotential gradient from the tickle field itself, which offsets the position of the ion relative to the equilibrium position and leads to the observation of a different local frequency at the new position, again due to anharmonicities in the overall trap potential.

5.3.2 Fidelity measurement

We determine the fidelity $\mathcal{F}$ of our two-qubit gate by measuring the state preparation fidelity of the actually produced state with respect to the ideally prepared state $|\Psi\rangle$ as described in Sec. 2.5.1. To this end, we apply a $\pi/2$ analysis pulse on the qubit transition after the gate operation (see Fig. 5.20 for the pulse sequence) and observe the global ion fluorescence as a function of the pulse's phase ϕ_a. When employing our state detection procedure described in Sec. 3.5, this results in the oscillations of the population probabilities $\mathrm{P}_{\uparrow\uparrow}(\phi_a)$, $\mathrm{P}_{\uparrow\downarrow,\downarrow\uparrow}(\phi_a)$ and $\mathrm{P}_{\downarrow\downarrow}(\phi_a)$ as shown in Fig. 5.21.

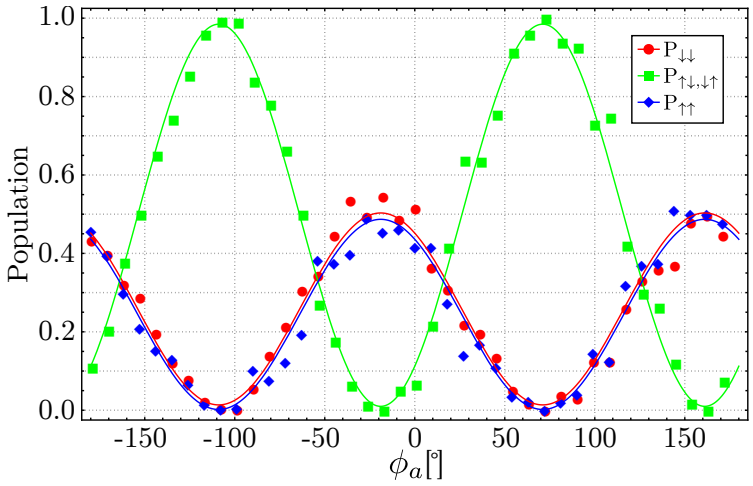

Figure 5.21: Population probabilities $\mathrm{P}_{\uparrow\uparrow}$, $\mathrm{P}_{\uparrow\downarrow,\downarrow\uparrow}$ and $\mathrm{P}_{\downarrow\downarrow}$ as a function of the analysis pulse's phase ϕ_a after the gate drive was applied. The solid lines are sinusoidal fits while each data point represents the average of 200 experiments. The total time for the phase scan amounts to about 3 min.

Fitting each population to a sinusoidal fit function of the form $f(\phi_a) = a + b\sin(2\phi_a + \phi_0)$ yields an amplitude of $\mathrm{P}_{\downarrow\downarrow} + \mathrm{P}_{\uparrow\uparrow} = 0.990 \pm 0.021$ and constitutes two of the three needed quantities for the fidelity determination via the identification $(\mathrm{P}_{\downarrow\downarrow} + \mathrm{P}_{\uparrow\uparrow}) = (\rho_{\downarrow\downarrow,\downarrow\downarrow} + \rho_{\uparrow\uparrow,\uparrow\uparrow})$.

For the remaining quantity, we need to calculate the parity $\Pi(\phi_a)$ as a function of the phase and fit the observed oscillations again with a sinusoid (see Fig. 5.22). Here, the fit yields an amplitude of $|A_\Pi| = 0.975 \pm 0.012$ resulting in a total gate fidelity of $\mathcal{F} = 1/2\,(\mathrm{P}_{\downarrow\downarrow} + \mathrm{P}_{\uparrow\uparrow}) + |A_\Pi|\,/2 = 98.2\,\%$. Based on the derived uncertainties from the population fits and their error propagation through Eq. 2.47, we find the fidelity error to be $\pm 1.2\,\%$.

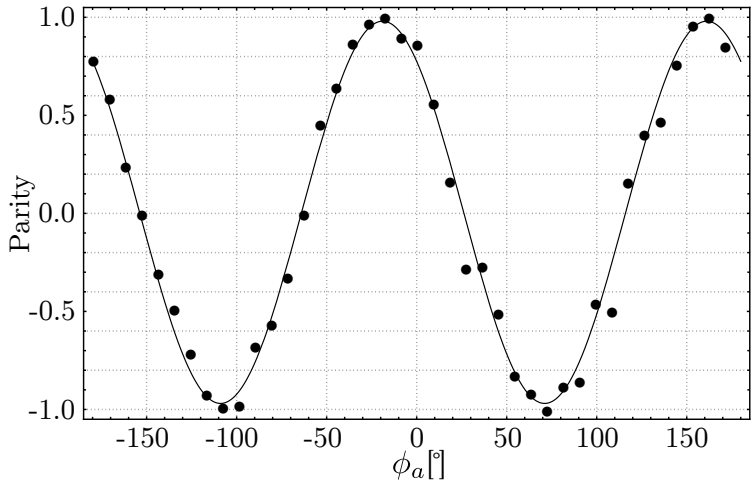

Figure 5.22: Parity $\Pi(\phi_a) = \mathrm{P}_{\downarrow\downarrow}(\phi_a) + \mathrm{P}_{\uparrow\uparrow}(\phi_a) - \mathrm{P}_{\uparrow\downarrow,\downarrow\uparrow}(\phi_a)$ signal after preparing the maximally entangled state $|\Psi\rangle$ using the population probabilities shown above. As the phase ϕ_a of the analysis pulse is varied, the parity oscillates as $\cos(2\phi_a)$ with an amplitude equal to twice the magnitude of the matrix element $\rho_{\downarrow\downarrow,\uparrow\uparrow}$.

5.3.3 Characterizing experimental sources of infidelity

In the following we present all measurements that have been carried out in order to estimate the size of certain error contributions for our best gate operation. Besides one exception, all experimentally determined parameters are translated to an infidelity $1-\mathcal{F}$ by Marius Schulte employing the master equation approach outlined in Sec. 2.5.2. We note that the error budget has no claim of completeness as error sources like slow radial mode fluctuations or a miscalibrated gate time or detuning are not yet considered. However, the current analysis still helps to identify present limitations of our approach and the experimental apparatus which need to be addressed in the future. A table listing all considered error sources and their respective infidelity contributions is given in Sec. 5.3.4.

5.3.3.1 Radial mode frequency instability

High-fidelity gates require the bichromatic gate drive to maintain a fixed detuning from the chosen motional mode frequency as otherwise the loops in motional phase space are not entirely closed and thus, the ions' spin and motional states remain entangled. As a consequence, the preparation fidelity of the desired maximally entangled state is reduced for detuning fluctuations during the gate operation.

To estimate the infidelity contribution of this effect in our setup, we investigate the frequency stability of the two-ion radial HF rocking mode, the selected mode for the gate operation, over time using the 'tickle' experiment illustrated in Fig. 5.23. The experiment starts with Doppler cooling and Raman sideband cooling of the HF rocking mode to a thermal state of $\bar{n} \simeq 0.11$. After preparing both ions in $|\downarrow\rangle$, we inject a 10 ms long tickle pulse of variable frequency to the trap electrode DC_2.

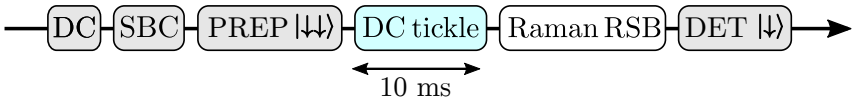

Figure 5.23: Pulse sequence to determine the HF rocking mode frequency of two ions prior to the gate operation.

Here, the tickle signal is produced by one of our DDS units and is guided through a series of attenuators[52] in order to enable a remotely adjustable signal amplitude of 0.5 dB step size around the desired power level of −67 dBm. After the tickle drive, we apply a Raman RSB π pulse on the HF rocking mode of length t_p and detect the population in state $|\downarrow\rangle$. Given an appropriate choice of t_p, which is optimized beforehand, this experiment results in one of the following two cases:

1. The tickle drive is (near) resonant with the HF rocking mode and heats the collective ion motion due to the arising forces of the additional tickle potential. As the HF rocking mode is now excited out of the ground sate, the RSB pulse induces a partial population transfer $|\downarrow\downarrow\rangle\,|n\rangle \rightarrow |\uparrow\uparrow\rangle\,|n-1\rangle$ resulting in a reduced fluorescence signal during the state detection of $|\downarrow\rangle$

2. The tickle drive is not resonant with the HF rocking mode, leaving the motion of the ions unaffected. Consequently, the RSB pulse does not induce a population transfer and the subsequent detection of $|\downarrow\rangle$ keeps the normal fluorescence level

Repeating this experiment for different tickle frequencies near the HF rocking mode results in a data set as shown in Fig. 5.24 (a) and enables the extraction of the mode frequency via a Lorentzian fit. Following this, we can measure two kinds of motional mode frequency fluctuations.

[52] Vaunix, Lab brick LDA-102; and Mini Circuits, VAT-20+

On the one hand, we can perform multiple tickle scans over time in order to reveal mode fluctuations on time scales longer than the tickle scan itself (typically $\sim$ 1min). On the other hand, we can also track the full width at half maximum (FWHM) from the Lorentzian fits to measure mode variations happening on time scales faster than an individual tickle scan. On the day of the best gate data, both of these measurements have been performed and imply a fluctuation of the HF rocking mode frequency of within $\pm 300\,\mathrm{Hz}$ during two hours (see Fig. 5.24 (b)) and a corresponding mean FWHM of about 110 Hz (see Fig. 5.24 (c)).

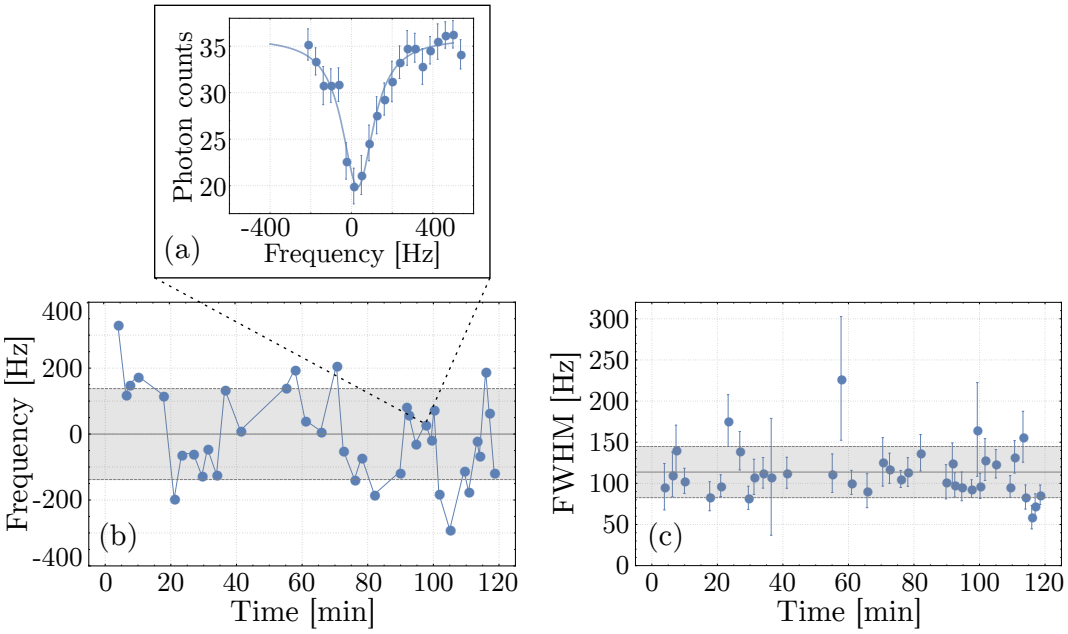

Figure 5.24: Frequency stability measurement of the two-ion rocking mode. Gray solid lines indicate the mean of the data points while the gray dashed lines denote the corresponding standard deviation. (a) Typical result of the tickle experiment used to determine the frequency and full-width half maximum (FWHM) of the motional mode following the sequence illustrated in Fig. 5.23. The frequency axis is with respect to the mean of the time tracking data shown in (b) at around 6.31 MHz. (c) Full-width at half maxima of the time tracking data shown on the left with a mean value of about 110 Hz. Each data point is obtained from a Lorentzian fit whose uncertainty is indicated by the error bars.

However, as the 'slow' mode fluctuations appear to happen on time scales way longer than an individual gate experiment, we decided to not yet include the influence of this error source in the current error analysis and to focus exclusively on frequency fluctuations on comparable time scales as the gate

operation itself. As a consequence, we only used the FWHM of the tickle scan right before the 98.2 % gate, given by 101 Hz, which is in reasonably good agreement with the measured mean FWHM. Based on this value, we assume the resulting standard deviation of the gate detuning from gate to gate to be $\sqrt{\langle(\delta_\epsilon/\delta)^2\rangle} = 1.1 \times 10^{-2}$.

Another detuning fluctuation is given by an observed linear frequency chirp of about 0.3 Hz/μs and is suggested to originate from thermal transients within the trap electrodes due to the gate drive being applied. While a similar effect has also been observed in another microwave near-field experiment [Sep16], the hypothesis of its thermal origin is additionally supported by an observed saturation of the effect at around 1 ms (see Fig. 5.25). However, even though we introduced a 400 μs long warmup pulse before the gate pulse in order to limit the chirp amplitude during the gate, we still estimate a linear detuning change of 180 Hz within the first 600 μs of the gate pulse.

Following our numerical simulations described in Sec. 2.5.2.1, the total infidelity due to both considered frequency fluctuations of the HF rocking mode calculates to 1.3×10^{-2}.

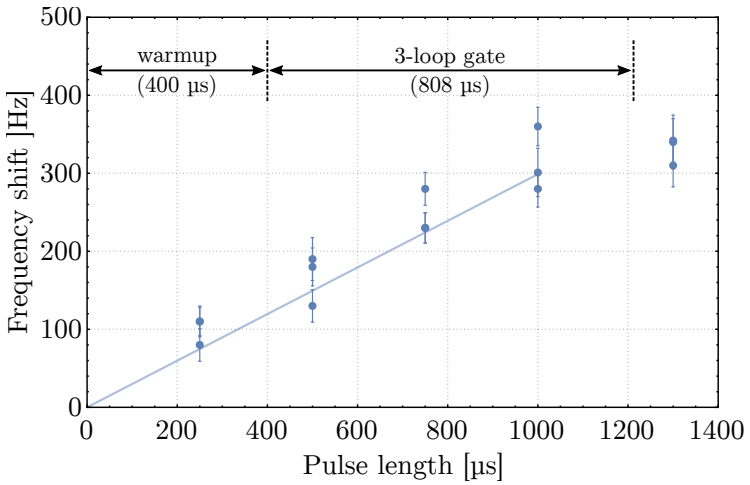

Figure 5.25: Frequency chirp on the single ion's radial HF COM mode as a function of time the gate drive is turned on. The data points are obtained by performing interleaved tickle experiments with and without the gate drive turned on while the gate pulse length is varied. The difference between both experiments is indicated as frequency shift. The data points imply a linear frequency chirp of around 0.3 Hz/μs up to a pulse length of about 1 ms as well as a constant frequency shift for longer pulse times.

5.3.3.2 Off-resonant couplings to spectator modes

Another error contribution is given by simultaneously driving the gate operation on other radial spectator modes whose center frequencies and relative frequency spacings to the HF rocking mode are listed in Tab. 5.2. As the

Radial mode	ν [MHz]	$\Delta\nu$ [kHz]
LF rocking	6.275	42.5
HF rocking	6.318	-
LF COM	6.374	56.0
HF COM	6.416	98.0

Table 5.2: Radial mode frequencies ν of a two-ion crystal as measured on the day of the best gate data. The right column indicates the respective detuning $\Delta\nu$ from the HF rocking mode which is used to produce the entangled state of the ions.

LF rocking mode with a relative frequency spacing of $\Delta\nu \simeq 2\pi \times 42.5\,\mathrm{kHz}$ is the nearest motional mode and hence contributes the largest error of this kind, we decided to only consider this mode in the analysis (cf. Sec. 2.5.2.2). Consequently, additional contributions of the COM modes have yet been neglected. Assuming equal Rabi frequencies for the HF and LF rocking mode, which seems feasible given the similar Rabi frequencies for both modes during microwave sideband cooling in Sec. 5.2.5, as well as the measured mean phonon numbers $\bar{n}_{\mathrm{LF,rock}} = 0.27$ and $\bar{n}_{\mathrm{LF,rock}} = 0.11$, respectively, we simulate the infidelity contribution due to competing gate dynamics to be 5.2×10^{-3}.

5.3.3.3 Motional heating

Another considered error contribution arises from uncontrollable heating of the chosen motional mode during the gate operation due to interactions of the ion with the environment. Following [SM00], we model this incoherent error source in our numerical simulations as a coupling between the motional mode with a thermal reservoir by including the Lindblad term $\mathcal{L}_h$ as defined in Sec. 2.5.2.3 in the master equation. With the estimated heating rate of the HF rocking mode of $\dot{\bar{n}} \simeq 28 \pm 5\,\mathrm{phonons/s}$ (cf. Fig.5.18), we find the resulting infidelity contribution induced by motional heating to be 3.8×10^{-3}.

5.3.3.4 Off-resonant carrier excitation

Even though we took special care in optimizing the geometry of the MWM conductor, applying the gate drive still results in residual oscillating magnetic fields at the ion position. As these fields can induce unwanted spin-flips on the qubit or spectator transitions during the gate operation, they can also contribute an error. However, as prohibitive dimensions of the Hilbert space prevented us from directly simulating this error source within our master equation approach, we decided to estimate its significance by performing the gate operation on a single ion with the very same parameters as for two ions (similar to ref. [Sep16]). Here, the gate drive is about 60 kHz detuned from the nearest motional mode, i.e. the single-ion LF COM, and is therefore not expected to induce sideband transitions. Consequently, only the influence of the gate drive on the qubit spin-states is revealed.

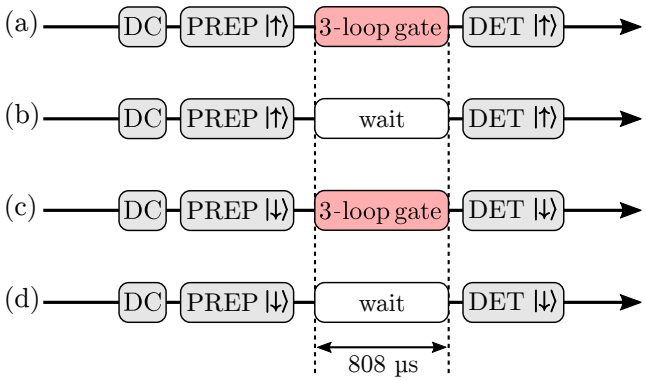

Figure 5.26: Pulse sequences to investigate the error source of off-resonant carrier excitations induced by the gate fields.

As shown in Fig. 5.26, we perform in total four experiments which can be separated in two groups. The first group comprises experiment (a) and (b) and investigates the influence of the gate operation on the population in $|\uparrow\rangle$. Here, the only difference between (a) and (b) is given by the replacement of the gate pulse in (a) with a waiting time of the same length in (b) prior to the detection of $|\uparrow\rangle$ common for both experiments. Conversely, the second group consists of the pulse sequences (c) and (d) and examines the impact of the gate operation on an ion initially prepared in $|\downarrow\rangle$. Again, the only difference between these two experiments is given by the fact that the gate pulse in (c) has been replaced with a waiting time in (d). In order to extract the influence of the gate on either qubit state, we repeat the experiments of each group about 3.8×10^4 times and measure the population deviation between

the experiments within the respective group. We find a population difference between experiment (b) and (a) of $\epsilon_\uparrow = 1.5 \times 10^{-3}$ and between experiment (d) and (c) of $\epsilon_\downarrow = 6.5 \times 10^{-4}$. Following [Bal17], we translate these errors into an infidelity contribution via $1 - \mathcal{F} \approx \frac{3}{2}(\epsilon_\uparrow + \epsilon_\downarrow)$ resulting in a gate error due to off-resonant carrier excitations of 3.2×10^{-3}.

Note, however, that within the limits of uncertainty of the data taken, the population difference between the two scenarios is still consistent with no population change at all, so that we only consider this result as an upper bound for the corresponding infidelity contribution. Consequently, this effect would have to be investigated in more detail once other sources of infidelity are further reduced.

5.3.3.5 Qubit decoherence

In order to investigate the coherence time τ_2 of the qubit transition, we employ the single-ion Ramsey experiment illustrated in Fig. 5.27 (a). Here, a scan of the relative phase of the two resonant $\pi/2$ pulses results in Ramsey fringes whose amplitude decreases for extending Ramsey times as noise reduces the phase coherence between the qubit and microwave drive. When following the typical approach, the decreasing fringe contrast is fitted by an exponential decay function in order to determine the coherence time (cf. Fig. 4.7). However, as the expected coherence time of our qubit transition would easily result in experimental sequences comparable to the typical ion lifetime ($\sim 20\,\mathrm{min}$), we decided to perform experiments only up to a Ramsey time of $T_{\mathrm{Ramsey}} = 0.5\,\mathrm{s}$. Consequently, only a lower bound of the coherence time can be given. Fig. 5.27 (b) shows a comparison of the Ramsey fringes as obtained for a Ramsey time of 0.1 s and 0.5 s. As the fringe contrast does not change significantly between both measurements, we conclude $\tau_2 > 0.5\,\mathrm{s}$ and calculate the infidelity contribution due to qubit decoherence to be smaller than 9.3×10^{-4} following our simulations described in Sec. 2.5.2.4.

As a final remark we note that measurements of long coherence times can be challenging without sympathetic cooling as the reduced fluorescence rate after the Ramsey experiment might, besides decoherence, also originate from ion heating.

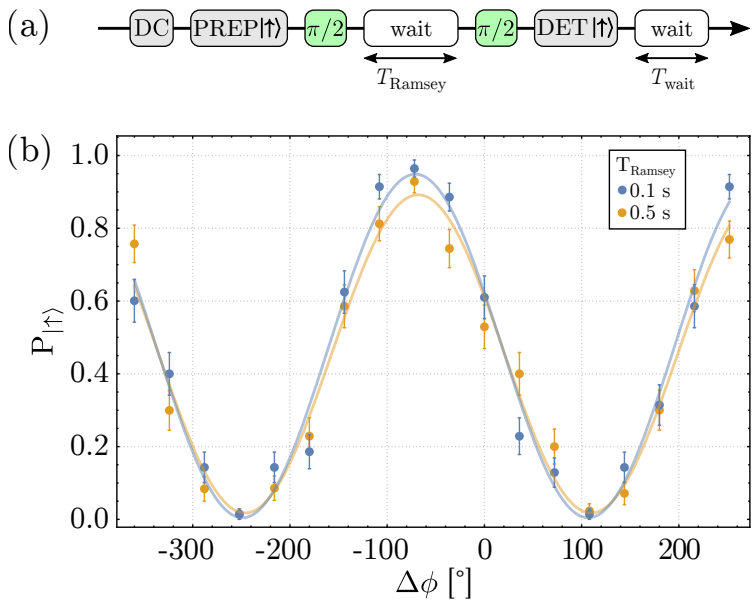

Figure 5.27: Ramsey experiment to estimate a lower bound on the qubit coherence time. The experimental sequence is shown in (a) and includes an additional waiting time of $T_{\mathrm{wait}} = 0.5\,\mathrm{s} - T_{\mathrm{Ramsey}}$ to maintain the same duty-cycle of the detection AOM for different Ramsey times. (b) Fringes comparison for two different Ramsey times. Sinusoidal fits (solid lines) yield a contrast of 0.95 ± 0.03 for $T_{\mathrm{Ramsey}} = 0.1\,\mathrm{s}$ and 0.89 ± 0.03 for $T_{\mathrm{Ramsey}} = 0.5\,\mathrm{s}$.

5.3.3.6 Microwave power instability and pulse shape

This subsection contains all considered error contributions connected to the pulse shape of the gate drive and comprises fluctuations of the differential AC Zeeman shift, the shape of each microwave sideband pulse as well as their relative Rabi frequency imbalance.

The differential AC Zeeman shift is induced by residual oscillating magnetic fields of both field patterns produced by the RSB and BSB drive at the ion position and was measured to be $\Delta_z/(2\pi) = 4.37\,\mathrm{kHz}$ employing Ramsey spectroscopy on the qubit transition while the gate drive was turned on. Although this shift of the qubit transition is taken into account in the frequencies of the gate fields (cf. Eq. 5.11 - 5.12), any power fluctuation of microwave pulses between gate operations can still alter the induced shift and hence, contribute an error due to the asymmetric detuning change of the bichromatic fields relative to the HF rocking mode. Following up on Sec. 4.7.1 we use an active feedback loop to stabilize the envelope of each sideband pulse to a reference waveform and find the pulse power of the sideband pulses to be stable within 0.08%

after around 40 μs with respect to the mean. Assuming this stability over the whole gate pulse length of 808 μs, we approximate the resulting standard deviation of the AC Zeeman shift to be $\sqrt{\langle(\Delta_\epsilon/\Delta_z)^2\rangle} = 8 \times 10^{-4}$. According to our simulations described Sec. 2.5.2.5, this translates into a gate infidelity of 1.1×10^{-4}.

To investigate the error contribution of imbalanced Rabi frequencies of both bichromatic field components, we connect the output of both sideband drives to diode detectors[53] and compare their pulse shapes on an oscilloscope. Following this, we measure the relative power difference between the pulses to be within $\sim 0.2\%$ for the chosen gate pulse length of 808 μs resulting in an insignificant simulated error contribution of 4.1×10^{-6}. Finally, we also include the additional gate dynamics and the changing AC Zeeman shift due to the adiabatic switching of the microwave pulses at the beginning and end with a 2 μs long cumulative error function (cf. Sec. 4.7.1) in our simulations. Based on the approximation that the flat part of the gate pulse is 808 μs long, we find the pulse shape to contribute a simulated infidelity of 6.3×10^{-4} to the overall error budget. For further details on the simulations of the last two effects, see Sec. 2.5.2.6.

5.3.4 Error budget summary

In summary, we have investigated the contribution of the different error sources listed in Tab. 5.3 to the infidelity of our best gate operation. Most of the tabulated infidelities are simulated via a master equation (cf. Eq. 2.49) assuming ideal gate dynamics and the specific noise contribution in form of the indicated parameter. According to our analysis, we find the following three error contributions to be most significant.

The first one is given by frequency instabilities of the HF rocking mode and comprises an instantaneous linewidth of $2\pi \times 101$ Hz as well as an induced frequency 'chirp' of 0.3 Hz within the first 600 μs of the gate operation. While the mode's linewidth can potentially be narrowed down by technical improvements of the RF setup [Har13], the impact of the 'chirp' on the gate detuning can, to some extent, be alleviated by e.g. longer warm-up pulses[54]. The second largest contribution is caused by driving the identical spin-spin interaction on the LF rocking mode with a relative frequency spacing of $\Delta = 42.5$ kHz. As this effect

[53] Herotek, Schottky diode detector DHM124AA, 50 Ω terminated at the oscilloscope

[54] As longer warm-up pulses also increase the thermal load deposited in the trap, this approach entails additional risks that need to be taken into account.

scales inversely with the radial mode splitting, it can be suppressed by engineering the trap potentials accordingly. The third largest error is induced by motional heating of the HF rocking mode by 28 phonons/s and is suspected to originate from electric-field noise emanating from the trap electrodes. While this incoherent error typically represents a non-negligible source of infidelity in surface traps at room temperature, its impact can significantly be reduced by an *in situ* surface cleaning of the trap electrodes [HCW$^+$12] or operating the trap at cryogenic temperatures [LGL$^+$08, CS14]. In our group, both of these countermeasures are currently pursued.

Finally, we note that, besides the aforementioned modifications to the apparatus, also more elaborate gate schemes including Walsh modulation [HCD$^+$12] or dynamic decoupling [HSA$^+$16] can be applied to decrease the sensitivity of the gate operation with respect to certain noise sources. However, as the presented work is meant to investigate current limitations of the setup in order to enable possible modifications in the future, non of these schemes have been implemented yet.

Error source	Parameter	Infidelity
Radial mode frequency instability	$0.3\,\mathrm{Hz}/\mu s$ 'chirp' for $600\,\mu$s, $\sqrt{\langle(\delta_\epsilon/\delta_\mathrm{g})^2\rangle} = 1.1 \times 10^{-2}$	1.3×10^{-2}
Off-resonant coupling to spectator modes	$\Delta\nu = 42.5\,\mathrm{kHz}$ with $\bar{n}_{\mathrm{LF,rock}} = 0.27$	5.2×10^{-3}
Motional heating	$\dot{\bar{n}}_{\mathrm{HF,rock}} = \gamma_h = 28\,\mathrm{s}^{-1}$	3.8×10^{-3}
Off-resonant carrier excitation	$\epsilon_\uparrow = 1.5 \times 10^{-3}$, $\epsilon_\downarrow = 6.5 \times 10^{-4}$ infidelity calculated following [Bal17]	$< 3.2 \times 10^{-3}$
Qubit decoherence	$\tau_2 = 1/\gamma_d > 0.5\,\mathrm{s}$	$< 9.3 \times 10^{-4}$
Microwave pulse shape	$2\,\mu$s cumulative error function	6.3×10^{-4}
Differential AC Zeeman shift fluctuation	$\sqrt{\langle(\Delta_\epsilon/\Delta)^2\rangle} = 8 \times 10^{-4}$	1.1×10^{-4}
Rabi frequency imbalance	$(\Omega_R/\Omega_B - 1) = 2 \times 10^{-2}$	4.1×10^{-6}

Table 5.3: Error budget of the two-qubit gate presented in Sec. 5.3.1. If not stated differently, the infidelities are obtained via the master equation Eq. 2.49 including the respective error source with a strength given by the parameters. The total infidelity amounts to 2.7 % and is consistence with the measured infidelity of the gate of 1.8 ± 1.2 %. We note that the error budget has no claim of completeness as, for example, additional error contributions such as imperfectly calibrated gate times and/or detunings are not yet considered.

Chapter 6

Prototype multi-layer ion trap

In this chapter we present a prototype multi-layer ion trap with integrated 3-dimensional (3D) microwave circuitry which has been developed to demonstrate microwave quantum logic operations with $^9Be^+$ qubits in a scalable architecture. The overall trap design originates from ref. [Wah16] and was fabricated based on a novel fabrication technique outlined in [BSZH+19]. The chapter starts with an introduction of the electrode layout, the fabrication process and the trap assembly. After a description of the relevant changes to the apparatus outlined in Ch. 4, a measurement of the secular frequencies as well as the characterization of the resulting near-field pattern of the MWM conductor are presented. The chapter coarsely follows reference [HZBS+18].

6.1 The trap

6.1.1 Fabrication and electrode layout

The multi-layer ion trap (also called 'ML5G') is a room-temperature, microfabricated surface-electrode ion trap with a nearest ion-to-electrode distance of $d \simeq 35\,\mu$m in which electrodes can extend up to three individual fabrication layers named L_1, V_1 and L_2 (bottom-up). The trap was fabricated by Amado Bautista-Salvador and co-workers at the cleanroom facilities of Physikalisch-Technische Bundesanstalt (PTB) in Braunschweig following the multi-layer processing (MLP) method depicted in a simplified version in Fig. 6.1. Further details on the fabrication can be found in ref. [BSZH+19].

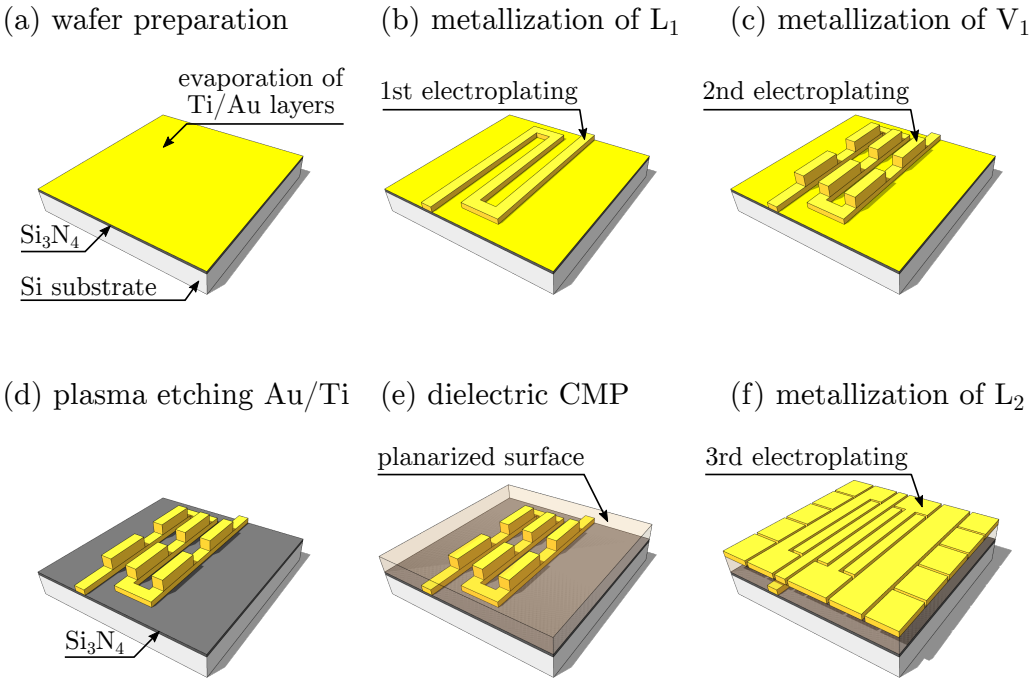

Figure 6.1: Simplified fabrication flow of the multi-layer ion trap. The shown electrode layout is only for illustration purposes and does not represent the layout of the installed trap. The figure is adapted from reference [BSZH+19].

Briefly summarized, the fabrication begins with a high-resistivity Si substrate which is coated with a 2 μm thick silicon nitride (Si_3N_4) layer employing plasma-enhanced chemical vapor deposition (PECVD) and continues with a thermal evaporation of a 10 nm thick titanium (Ti) adhesion layer as well as a 50 nm thick gold (Au) seed layer on top, see Fig. 6.1 (a). In the next steps, the bottom layer L_1 (Fig. 6.1 (b)) and the interconnect layer V_1 (Fig. 6.1 (c)) are metallized utilizing UV photolithography and Au electroplating. After removing the Ti adhesion and Au seed layer via plasma etching (Fig. 6.1 (d)), a dielectric film is spin coated on top of both metal layers and subsequently planarized in a chemical-mechanical polishing (CMP) step as depicted in Fig. 6.1 (e). The metallization of the upper layer L_2 follows a similar procedure as for the bottom layer L_1 and consists of a thermal evaporation of an Au/Ti layer on top of the planarized surface, Au electroplating as well as a final removal of the Ti/Au layers employing plasma etching (Fig. 6.1 (f)). Finally, the dielectric in the gaps is removed down to either L_1 or the substrate using fluorine-based plasma etching. Following this procedure, the layer thicknesses of the installed ML5G trap are measured to be $h_{L1} = 4.4\,\mu$m for L_1, $h_{V1} = 9.5\,\mu$m for V_1 and $h_{L2} = 5.2\,\mu$m for L_2 using a profilometer and resulted from an optimization

procedure with finite element simulations as described in the next section. The gap size was found to be $\sim 5\,\mu$m, resulting in an aspect ratio of 1:4 for the whole fabrication stack. Pictures of a fabricated trap are shown in Fig. 6.2.

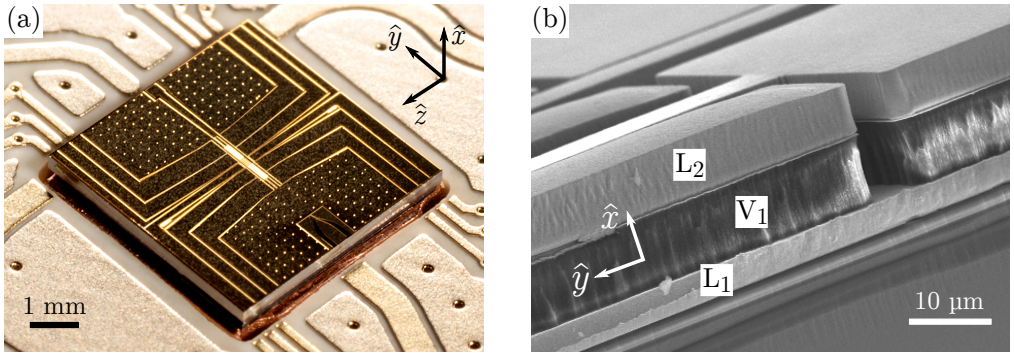

Figure 6.2: (a) Photograph of a diced ML5G chip before wire bonding the electrodes to the respective traces on the filterboard. The dots indicate vertical vias which connect ground planes in L_1 and L_2. The dark color of the electrodes is caused by an optical filter used for the photograph. (b) SEM picture of a cross-section of a cleaved chip to illustrate the different fabrication layers.

The fabricated electrode layout is sketched in a colorized version in Fig. 6.3 (a) and consists of 10 DC electrodes, one split RF electrode, one 3D microwave conductor labeled MWM and two additional microwave conductors labeled MWC_1 and MWC_2. Here, all electrodes and feedlines needed for ion trapping are located in the upper layer L_2 as shown in Fig. 6.3 (b) while the microwave conductor labeled MWM extends to all three fabrication layers as shown in Fig. 6.3 (c) enabling a more complex geometry as the one presented in the single-layer trap (see Sec. 6.1.2 for further details). However, in the experiment its purpose is again to induce motional sideband transitions on the field-independent qubit transition. Conversely, the microwave conductors MWC_1 and MWC_2 can each be used to drive spin-flip operations on the relevant hyperfine transitions of the electronic ground state. In this thesis we exclusively make use of MWC_2 while MWC_1 remains unused. Typical Rabi frequencies for spin operations induced by MWC_2 for an applied microwave power of $\sim 250\,$mW are listed in Tab. 3.2.

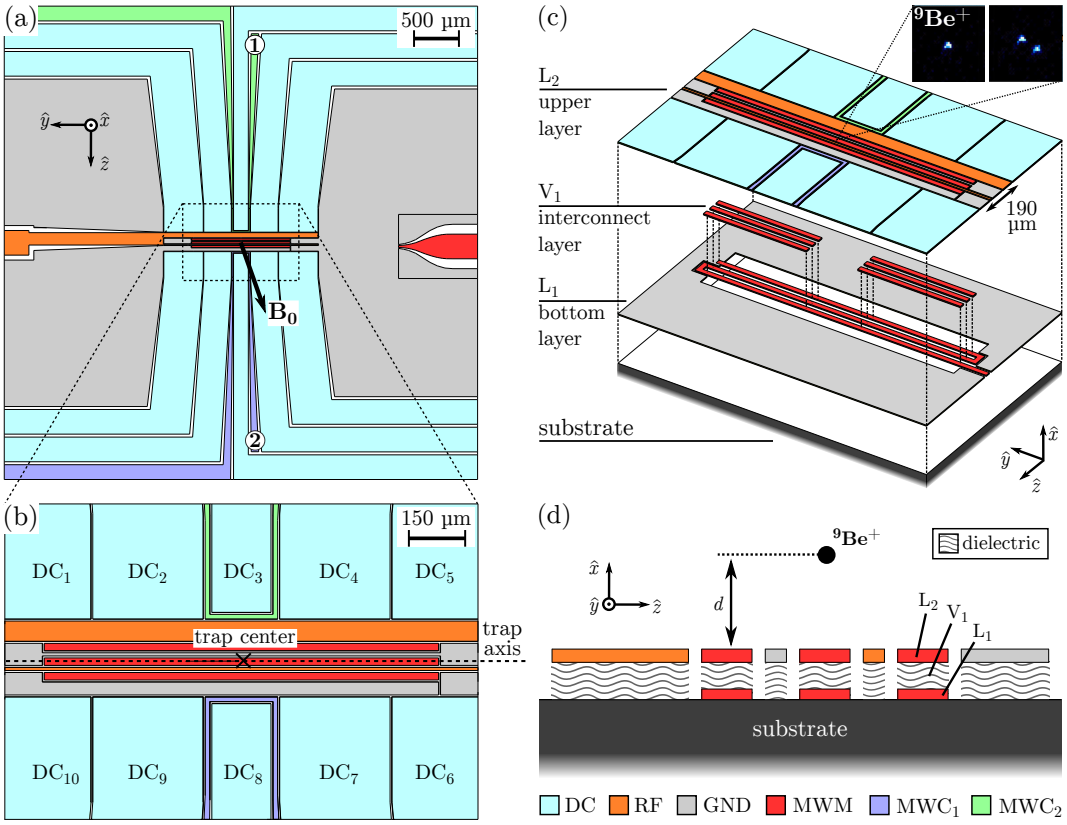

Figure 6.3: (a) Colorized electrode layout of the full multi-layer ion trap. The position marked '1' ('2') indicates the position at which the conductor labeled MWC_1 (MWC_2) is connected to a ground plane in L_1 through a via in V_1. The MWM conductor starts with a tapered bonding pad in L_1 and only extends to the upper layer L_2 in the central trap region. (b) Electrode layout of the upper layer L_2 around the trap center. (c) Exploded view of the three individual fabrication layers; for clarity, the dielectric material in L_1 and V_1 is not shown here. The inset shows fluorescing $^9Be^+$ ions on the EMCCD camera of the imaging setup. (d) Cross-section through the trap center showing all fabrication layers (L_1, V_1, L_2) as well as the dielectric to isolate different layers. The ion-to-electrode distance d is about 35 μm.

6.1.2 3D microwave conductor design

As outlined in Sec. 2.1.2, the MWM conductor design emerges from an optimization procedure using finite element software in order to maximize the gradient B' at the ion position while keeping B as small as possible. For the presented ML5G trap and the chosen ion-to-electrode distance of about $35\,\mu$m, the simulations[55] led to the electrode layout and MWM conductor design illustrated in Fig. 6.3. Here, the conductor implementation, which is illustrated with distorted dimensions and isolated from the neighboring electrodes in Fig. 6.4 for clarity, unifies several benefits when compared to an equivalent single-layer design. However, as the present thesis work was mainly concerned with the construction of the apparatus and the initial operation of the trap, only benefits related to its scalability are discussed in the following. Further details on the reduced coupling of the MWM conductor to other conductors or the improved field properties due to the implementation of the 'pocket' of length l_{th} within each meander segment can be found in ref. [HZBS+18]. In terms of scalability, the advantages are as follows.

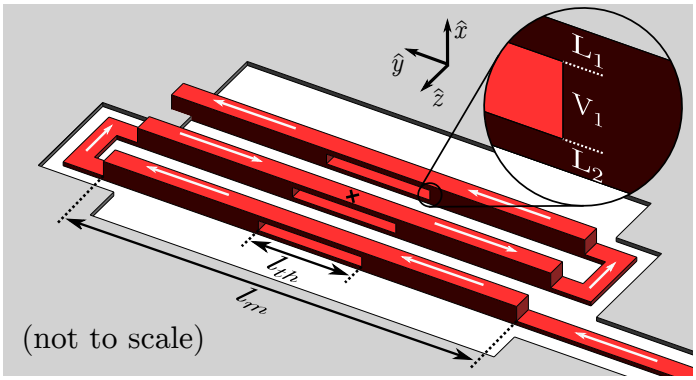

Figure 6.4: Schematic of the 3D meander-shaped microwave conductor MWM with distorted dimensions. For illustration purposes, we exclude all neighboring electrodes as well as the dielectric material in L_1 and V_1. The white arrows indicate a hypothetical DC current flow to guide the eye while the inset highlights the conductor's extension to all fabrication layers (L_1, V_1, L_2) along the three meander segments of length l_m. The pocket of length $l_{th} = 200\,\mu$m within each meander segment is purely located in the interconnect layer V_1 and has shown to improve the field properties of the MWM conductor in FEM simulations.

[55] The simulation model is based on the FEM software Ansys HFSS 17.2 and is described in ref. [Wah16]. For the ML5G trap the simulations have been mainly performed by Giorgio Zarantonello and Martina Wahnschaffe.

First, the possibility to place the conductor feedline completely in the bottom layer L_1 prevents interference with other electrodes in L_2 and thus demonstrates the potential of the multi-layer fabrication process when scaling up to larger arrays of ion traps and complex electrode arrangements [AUW+10]. In principle, the feedlines of the DC or RF electrodes could also be moved to L_1 in a future design.

Second, as shown in previous work [Wah16], one RF electrode has to be placed between two meander segments in order to achieve the desired overlap of the quadrupole's local field minimum with the RF null position. While this is in principle not a problem for a single trap module, it obstructs the approach of using a meander-shaped conductor to implement continuous RF electrodes as their maximum length is constrained to the segment length l_m of the meander structure. Hence, ion transport between different trap modules as envisioned by the QCCD architecture [WMI+98, KMW02] becomes only possible along one direction. However, for the 3D version of the MWM conductor the turning parts of the meander structure can be moved to the bottom layer L_2, thus enabling continuous RF electrodes and ion transport along the trap axis in both directions, cf. Fig 6.3 (b).

6.1.3 Trap assembly, beam configuration and loading

The assembly of the multi-layer trap is shown in Fig. 6.5 and mainly differs from the assembly of the ConsTrap in terms of the filterboard layout (see Appendix A.2 for a schematic). However, while the assembly is placed with the same orientation in the vacuum chamber like for the ConsTrap (cf. Fig. 5.6), the trap orientation was chosen slightly differently and is now rotated in a way that the radial plane forms a 30° angle with the quantization axis as shown in Fig. 6.6. Here, the three beams of the near-resonant beamline (BD, BDD, RE) are counter-propagating to the quantization axis to enable a pure σ^+-polarization for efficient Doppler cooling and optical repumping while the Raman beam configuration is chosen to form a $\Delta\boldsymbol{k}$ vector parallel to the quantization axis for 3D Raman sideband cooling. For ion loading we employ the same procedure as outlined in Sec. 5.1.6 which relies on laser ablation of a neutral beryllium target and subsequent photoionization via 235 nm photons. Details about the relative angles of the beams and the ablation plume are given in Fig. 6.6 (b) while further details on power levels and waists can be found in Sec. 5.1.6.

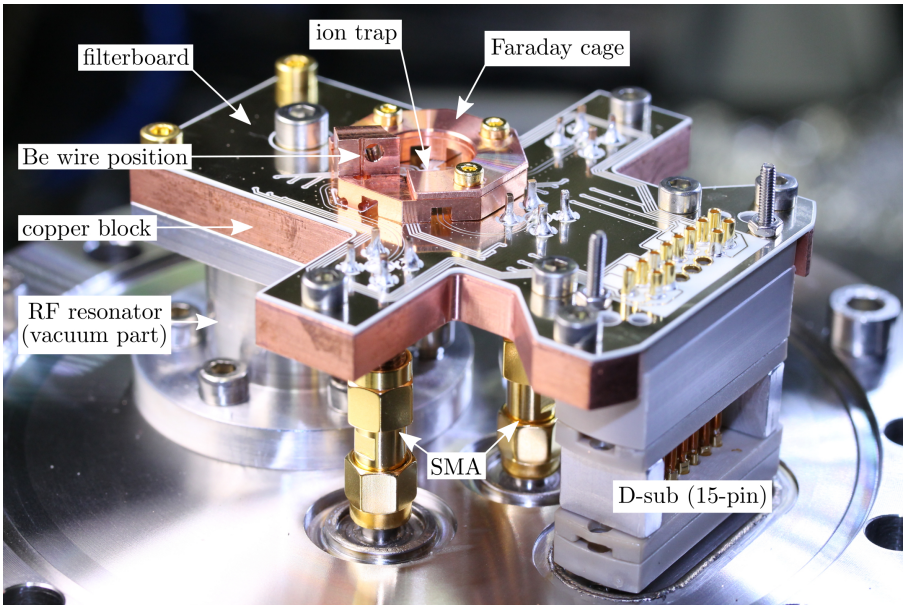

Figure 6.5: Photograph of the multi-layer ion trap assembly mounted to the feedthrough flange. The picture was taken before the gold mesh and beryllium wire were installed. The complete trap assembly is mounted on a single DN100 feedthrough flange via commercial connectors (SMA I-connectors for microwave signals, 15-pin D-sub for DC trap voltages) in order to simplify its installation or exchange in the cleanroom if needed.

6.2 Modified apparatus

The apparatus used for experiments with the ML5G trap is very similar to the one presented in Ch. 4. However, there are a few differences concerning the trap drives that are worthwhile to mention and are briefly listed in the following.

First, we changed the length of the coaxial resonator to 15 cm instead of 45 cm at atmosphere in order to increase the RF drive frequency from $\Omega_{\mathrm{RF}} \simeq 2\pi \times 88.2\,\mathrm{MHz}$ to $\Omega_{\mathrm{RF}} \simeq 2\pi \times 176.5\,\mathrm{MHz}$. Based on the new trap assembly and resonator length we followed the same procedure as outlined in Sec. 4.3.1.1 and found the capacitance of the trap assembly C_t and the loaded Q factor of the resonator to be 2.84 pF and ~ 50, respectively. Here, the comparably low Q factor of the resonator[56] is suspected to predominantly originate from the higher RF losses of the Silicon wafer when compared to the AlN wafer used

[56]For comparison the Q factor for the single-layer ion trap is ~ 367 at a resonator length of 45 cm and trap capacitance of $C_t = 3.28\,\mathrm{pF}$.

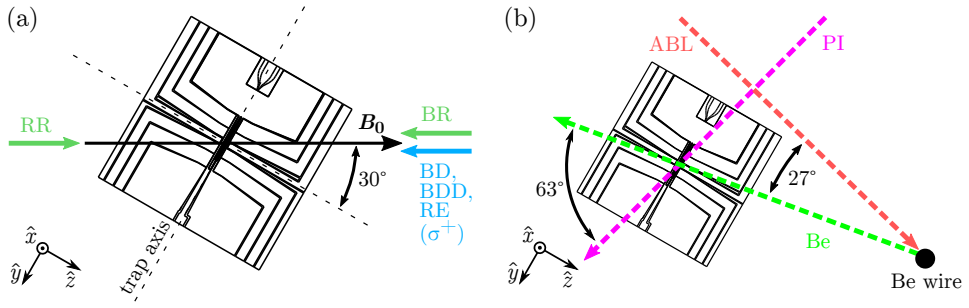

Figure 6.6: Beam configuration used for laser cooling and laser ablation loading in the ML5G trap. (a) Orientation of the multi-layer ion trap with respect to the quantization axis. BD/BDD: Doppler cooling beams, RE: repumper beam, RR/BR: Raman beams. (b) Beam geometry for laser ablation loading. The pulse laser (ABL) is focused on a beryllium target in order to produce an ablation plume (Be) which is guided towards the trap center via an aperture in the Faraday cage (cf. Fig. 6.5). At the trap center, neutral Be atoms can be ionized using the photoionization laser (PI). The Be wire has a diameter of 0.5 mm and a distance of about 12 mm to the trap center.

for the ConsTrap[57]. However, as both trap setups were operated at different RF drive frequencies and resonator lengths, the reason for the lower Q factor might also partially originate from other effects.

Second, we made use of the DC voltage amplifier boards mentioned in Sec. 4.3.2 in order to extend the voltage range of the arbitrary waveform cards from $\pm 10\,\mathrm{V}$ to about $\pm 50\,\mathrm{V}$. The main reason for this extension was to enable higher DC voltages and thus, higher axial trap frequencies than in the ConsTrap in order to simplify 3D sideband cooling (cf. Sec. 6.3.3).

6.3 Measurements

6.3.1 Secular frequencies

For axial and radial ion confinement, we apply DC voltages in the range of $\pm 26\,\mathrm{V}$ to DC_{1-10} and a radiofrequency signal of variable amplitude at $\Omega_{\mathrm{RF}} \simeq 2\pi \times 176.5\,\mathrm{MHz}$ to the RF electrode, respectively. According to our calculations based on the gapless plane approximation, the axial potential results in an axial trap frequency of 4 MHz and rotates the radial HF mode of about $-6°$ with

[57] The dissipation factor ($\tan\delta$) in the RF range is about 16 times higher for Silicon than for AlN [CBB+05].

respect to the $\hat{x}$-axis.

Experimentally, we test our electric-field model of the ML5G trap by measuring the secular frequencies and compare the results with the model predictions. To this end, we apply an oscillating 'tickle' voltage to DC_2 of the trap layout (cf. Fig. 6.3) which reduces the observed ion fluorescence when resonant with a motional mode frequency. Following this, we find the axial and radial mode frequencies of a single ion to be $(\omega_{\mathrm{ax}}, \omega_{\mathrm{LF}}, \omega_{\mathrm{HF}}) = 2\pi \times (4.12, 5.6, 9.33)\,\mathrm{MHz}$ as plotted in Fig. 6.7. Here, the axial trap frequency is in reasonably good agreement with the simulated value of 4 MHz. Concerning the radial modes, the model shows best agreement for an applied RF voltage of $V_{pp} \sim 104\mathrm{V}$ at $\Omega_{\mathrm{RF}} \simeq 2\pi \times 176.5\,\mathrm{MHz}$ corresponding to simulated LF and HF mode frequencies of 5.25 MHz and 9.57 MHz, respectively. The resulting intrinsic trap depth is $\sim 10\,\mathrm{meV}$.

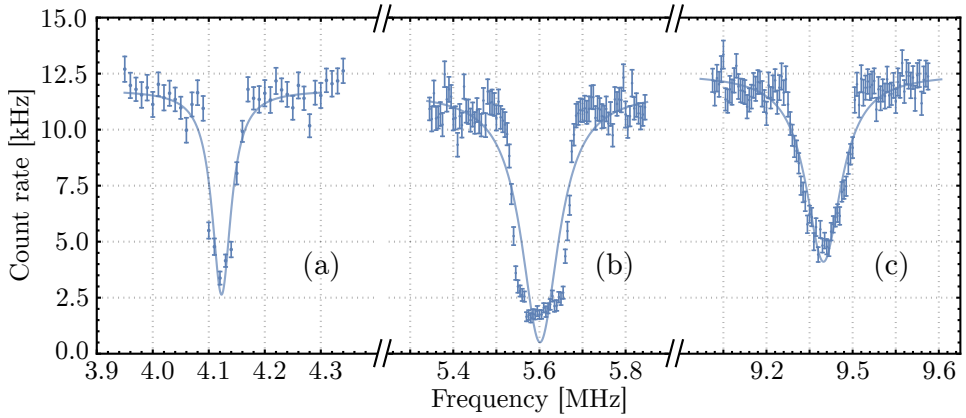

Figure 6.7: Trap frequency measurement of a single ion using the 'tickle' method. The frequencies are determined by a Lorentzian fit. (a): axial mode, (b): radial LF mode, (c): radial HF mode

6.3.2 Microwave near-field gradient characterization

To characterize the resulting magnetic near-field pattern of the MWM conductor, we measure its induced AC Zeeman energy shift on suitable hyperfine transition of the electronic ground state $^2S_{1/2}$ for different ion positions in the radial plane. The exact procedure is detailed in Sec. 5.1.8 and is based on a pulse sequence developed in [WOC+13a]. Briefly summarized, its basic idea is to off-resonantly excite the MWM conductor between two $\pi/2$ pulses of a Ramsey experiment and to measure the induced AC Zeeman shift on transition Q or C by fitting the observed phase accumulations of the respective superposition

state. While repeating this measurement for different radial positions allows to infer the spatial distribution of the resulting near-field pattern, retaking the measurement for different transitions enables complementary information about the field's properties as needed for a subsequent fit of the shift data to a 2D quadrupole model [WHZ+17].

Following this procedure, the left column in Fig. 6.8 shows the absolute AC Zeeman shifts on transition Q (top) and transition C (bottom) as a function of radial ion displacement when exciting the MWM conductor at a frequency 10 MHz blue detuned from transition Q. Like for the near-field characterization of the ConsTrap, the given x and z coordinates are referenced to the beforehand determined RF null position. In order to induce higher frequency shifts, the data of transition C is taken at a nominally 3 dB higher microwave power[58] than the qubit transition for which we apply 32.8 dBm. The right column displays a least square fit of the AC Zeeman shifts produced by the 2D quadrupole model of Eq. 5.3 (cf. Sec. 5.1.8). However, since the residual field in the minimum of the experimental data is too low to be fitted accurately, the residual magnetic field B as well as its orientation α have been manually set to zero in the fit procedure. For the remaining fit parameters, we obtain the values listed in Tab. 6.1.

Parameter	B	B'	α	β	ψ	x_{MW}	z_{MW}
Unit	[μT]	[T/m]	[°]	[°]	[°]	[μm]	[μm]
Fitted value	–	54.8	–	86.8	1.5	0.07	−0.14
Fitted error	–	1.7	–	7.6	7.6	0.05	0.65

Table 6.1: Resulting quadrupole parameters after fitting the AC Zeeman shift data in Fig. 5.9 to a quadrupole model as explained in the text. The shown values correspond to an applied microwave power at the MWM conductor of ~ 32.8 dBm.

In order to at least obtain an upper bound for B, we subsequently introduce it again in the fitted model as a parameter and calculate the required field to obtain the lowest measured AC Zeeman shift on transition C given by 551 Hz. Here, we assume that the measured shift represents the local minimum of the quadrupole and have set α to the orientation minimizing the coupling. Consequently, the resulting fitted value of B represents a worst-case scenario.

[58] The difference in applied microwave power is accounted for in the fit procedure by an additional fit parameter yielding a fitted power difference of 2.9 ± 1.5 dB.

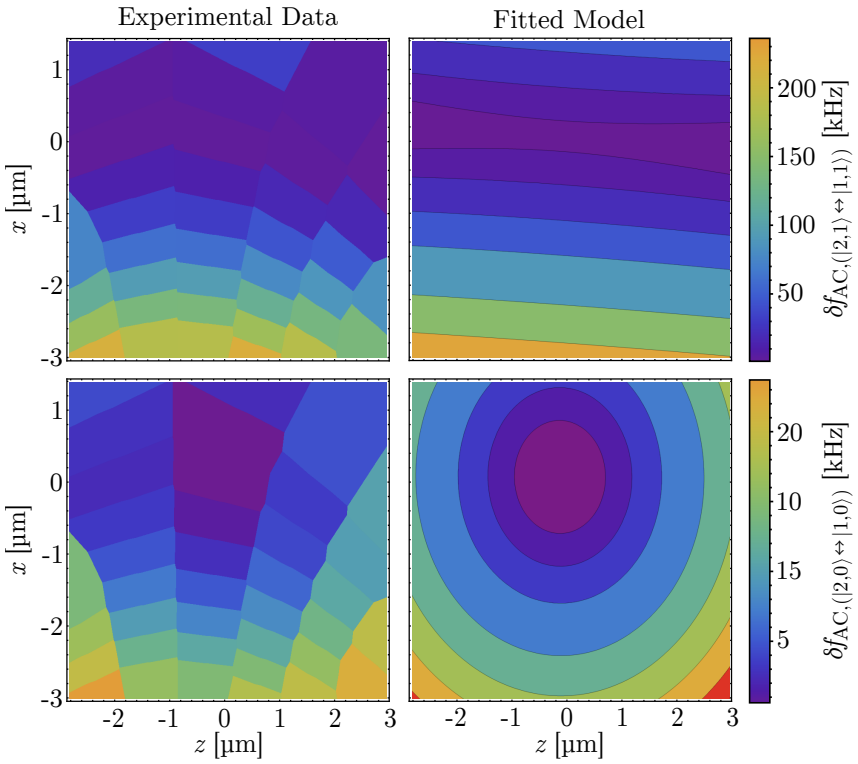

Figure 6.8: Absolute AC Zeeman shifts δf_{AC} induced by the produced near-field pattern of the MWM conductor as a function of x and z relative to the RF null position. Based on the gapless plane approximation, we estimate the RF null position to be at 34.6 μm above the chip surface. Figure reproduced from [HZBS+18].

Following this, we find B to be smaller or equal to 34 μT corresponding to a ratio of $B/B' \leq 0.62\,\mu$m. Based on these values, we can reach the following conclusions.

First, the gradient is mainly linear polarized (ψ small) and almost perpendicularly aligned to the chip surface ($\beta \simeq 87°$). Second, the quadrupole center is about $(\delta x, \delta z) = (0.07, -0.14)\,\mu$m shifted with respect to the RF null position. Third, when scaled to a roughly equivalent power level the achievable gradient in the ML5G trap is about 4.5 times higher than in the ConsTrap which is approximately consistent with the expected scaling of $B' \propto 1/d^2$ giving the different ion-to-electrode distances d in the single- and multi-layer trap of 70 μm and 35 μm, respectively. At the same time, the ratio B/B' in the ML5G trap is at least three times lower than in the ConsTrap when scaled to the approximately same applied microwave power, thus demonstrating the benefit of the relaxed constraints on the MWM conductor design in the multi-layer trap. Assuming the fitted value of B' and the calculated mode orientation of the

radial HF mode (cf. Sec. 6.1.1), we estimate the needed time for a single-loop two-qubit MS gate on the HF rocking mode to be on the order of $t_g \sim 120\,\mu$s.

6.3.3 Sideband cooling attempts

The ML5G trap was chronologically installed before the ConsTrap and was operated for about half a year until April 2018. The reason for its comparably short operation time was that, despite the observation of sideband transitions (cf. Fig. 6.9) and the comparably high secular frequencies (cf. Fig. 6.7), no sideband cooling could be achieved. The reasons for this are, however, still unclear and still under investigation.

The list of possible causes includes the different Raman beam geometry which would have required 3D ground state cooling as well as other modifications to the optical cooling setup in between ML5G and the ConsTrap. Other reasons might comprise a coupled ion motion along the different principle axes due to higher-order multipole terms in the trapping potential (see for example §3.4.2 of ref. [Bla10]) and a high heating rate due to the comparably small ion-to-electrode distance.

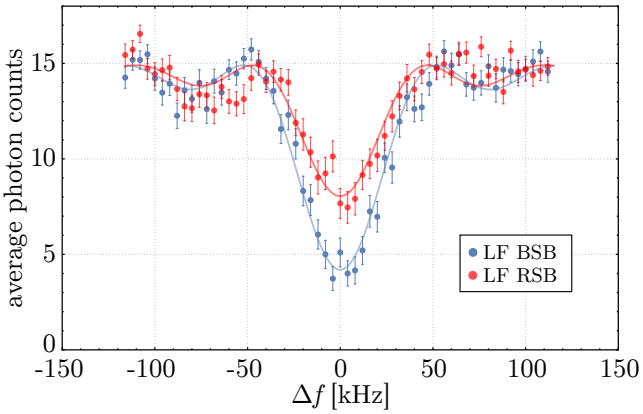

Figure 6.9: Sideband comparison of a single-ion's radial LF mode in the ML5G trap. The frequency detuning is with respect to the LF mode's center frequency at around $\omega_{\mathrm{LF}} = 2\pi \times 5.6\,\mathrm{MHz}$. The Raman beam probing time was $18\,\mu$s.

Chapter 7

Conclusions

7.1 Summary

During this thesis we have demonstrated the first microwave-driven two-qubit entangling gate in $^9Be^+$ ions using the resulting near-field pattern of a single microwave conductor embedded in a surface-electrode ion trap at room-temperature. We have tested the performance of the gate operation by preparing a maximally entangled state in a MS protocol and found the resulting state preparation fidelity to be $\mathcal{F} = 98.2 \pm 1.2\,\%$ employing a reduced tomography procedure. Following a numerical error analysis based on characterization measurements, we identified several infidelity contributions of the current experimental setup. However, almost all of them can be reduced upon technical improvements and do not represent a fundamental limitation to the approach. The three largest error contributions are found to be frequency fluctuations of the radial motional mode (1.3×10^{-2}), off-resonant couplings of the gate drive fields to spectator modes (5.2×10^{-3}) as well as motional heating (3.8×10^{-3}). Due to the optimized geometry of the employed microwave conductor, which has been designed to produce a high oscillating magnetic near-field gradient and small residual magnetic field at the ion position, the inherent error source of the microwave near-field approach of AC Zeeman shift fluctuations could be suppressed to an infidelity contribution of 1.1×10^{-4}. In total, the simulated infidelities of the considered noise sources amounts to 2.7×10^{-2} and is consistent with the experimentally measured infidelity of $1.8 \pm 1.2\,\%$.

Besides the implementation of the gate operation, the thesis work comprised comprehensive revisions to the apparatus as well as the design and construction of a Raman beamline. The latter has been successfully used to demonstrate ground state cooling of several radial motional modes near the motional ground state. Following a heating rate measurement of a single-ion's radial mode, we find good agreement with the expected scaling of the heating mechanism of $\propto d^{-4}$ given the ion trap's nearest ion-to electrode distance and a radial mode frequency of of $d = 70\,\mu$m and $\omega \simeq 2\pi \times 6.4\,$MHz, respectively. Furthermore, we also utilized the resulting microwave near-field gradient of the microwave conductor used for the gate to ground state cool a single ion's radial mode. Moreover, we tested a hybrid setup comprising permanent magnets and field coils with regard to its suitability to produce the needed quantization field of 22.3 mT for our to first-order field independent qubit transition. When compared to a previous version of the apparatus solely operating with field coils, the coherence time of the magnetic field-sensitive transition A could be increased by about an order of magnitude.

Finally, a prototype multi-layer surface-electrode ion trap with embedded microwave conductors for universal quantum logic operations has been installed and operated. The trap was fabricated in a novel fabrication technique developed in our group and comprises three individual fabrication layers. Making use of the additional layers, the trap's electrode layout features a 3-dimensional version of the meander-like microwave conductor whose geometry has been optimized for driving entangling quantum logic gates based on the microwave near-field approach. Following a characterization of the resulting field pattern with a single ion as local field probe, we find significantly better field properties when compared to previously tested single-layer designs. As the multi-layer microwave conductor addresses certain design restrictions of its 2D version and additionally enables the implementation of electrode feedlines in lower fabrication layers, the operated multi-layer ion trap demonstrates additional features regarding the scalability of the approach.

7.2 Outlook

Based on the presented results, future work will focus on reducing the largest infidelity contributions and increasing the fidelity as needed for fault-tolerant quantum computation. Here, especially the frequency stability and heating of the motional modes require larger modifications of the apparatus. While the

former might be improved by a re-design of the RF source including an active amplitude and frequency stabilization [Har13, JWCR$^+$16], the latter can likely be addressed in a vacuum setup with integrated Ar^+ gun for *in situ* cleaning of the electrode surfaces [HCW$^+$12]. Besides these technical modifications, which are both currently pursued in our group, further implementations of the gate operation could also focus on more elaborate gate schemes including Walsh modulation [HCD$^+$12] or dynamic decoupling [HSA$^+$16].

Furthermore, future efforts could also aim for an thorough investigation of standard preparation and measurement (SPAM) errors which include imperfections in the microwave transfer pulses as well as the state-dependent fluorescence detection. In case one of these two errors contributions is found to be limiting, the former could potentially be decreased by utilizing composite pulses (e.g. like the ones proposed in [TV11, GSHV14]) while the latter could likely be improved by increasing the photon collection efficiency of the imaging setup in order to reduce the overlap of the 0-ion, 1-ion and 2-ions bright Poisson distributions (cf. Fig. 3.5). Here, e.g. a new PMT with a higher quantum efficiency than 20 % at 313 nm might be a suitable option. Alternatively, also a new EMCCD camera with fast readout capabilities would help as it allows the individual state detection of multiple ions in spatially separated regions of interest and hence avoids at least the overlap of the 1-ion and 2-ions bright histograms.

In order to investigate the error per gate in a computational scenario, the single-qubit and multi-qubit gate error could be analysed using randomized benchmarking [KLR$^+$08, GMT$^+$12]. However, for the latter to be feasible the single-qubit error per gate would first need to be characterized and reduced well below the two-qubit gate error as otherwise a separation of the different gate error contributions is difficult. Moreover, randomized benchmarking of two-qubit gates also necessitates single-ion addressing [WOC$^+$13b] which has not yet been implemented in our setup and, additionally, might require sympathetic cooling of the ions due to the long gate times (microsecond scale).

Regarding the next trap design, a possible choice could be a multi-layer ion trap with a 3-dimensional meander for quantum logic operations and a similar ion-to-electrode distance as in the ConsTrap. Here, the electrode layout could be extended by other aspects of the QCCD architecture such as a junction or additional zones for ion loading or storage.

Appendix

A.1 Permanent magnet configuration

The following picture illustrates the used magnet configuration for both permanent magnet assemblies. In case the produced magnetic field of the assemblies decreases over time, additional sockets can be filled up.

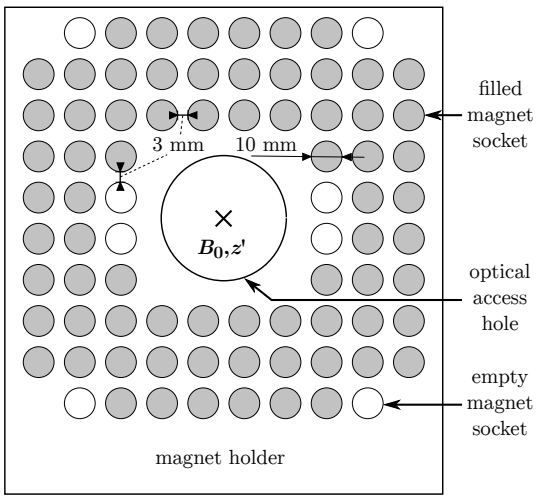

Figure A.1: Schematic of the magnet holder without the front panel. Figure adapted from [Jac17].

A.2 Schematics of filterboards

The filterboards of the two operated ion traps have been mainly designed by C. Ospelkaus and are attached here for completeness. The used components are identical for both filterboards and are summarized in Tab. A.1. For details on the used vacuum connectors, see Sec. 5.1.5.

Component	Company (model)	Comment
DC pins	Allectra (212-PinF-25)	-
SMD resistor	Barry Industries (RP0603BA-1001JN-91)	1 kΩ
SMD capacitor	Novacap (0603N821J101P)	820 pF
SMA jacks	Cinch Connectivity Solutions (142-0701-491)	insulator & conductor pin

Table A.1: Components of the single-layer and multi-layer trap filterboards.

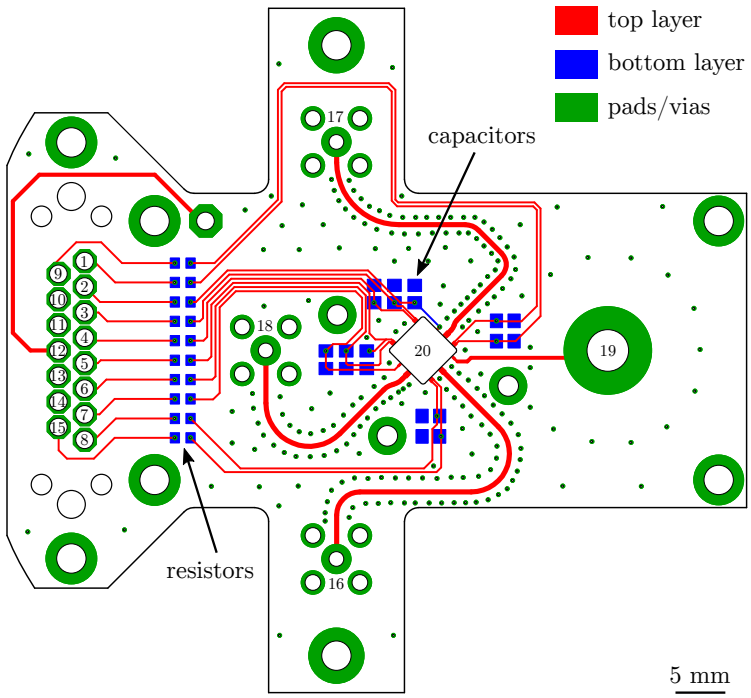

Figure A.2: Filterboard of the single-layer trap. 1: DC4, 2: DC3, 3: DC2, 4: DC1, 5: DC10, 6: DC9, 7: DC8, 8: DC7, 9: DC5, 10: NC, 11: NC, 12: Be wire, 13: NC, 14: NC, 15: DC6, 16: MWM, 17: MWC_1, 18: MWC_2, 19: RF, 20: ion trap

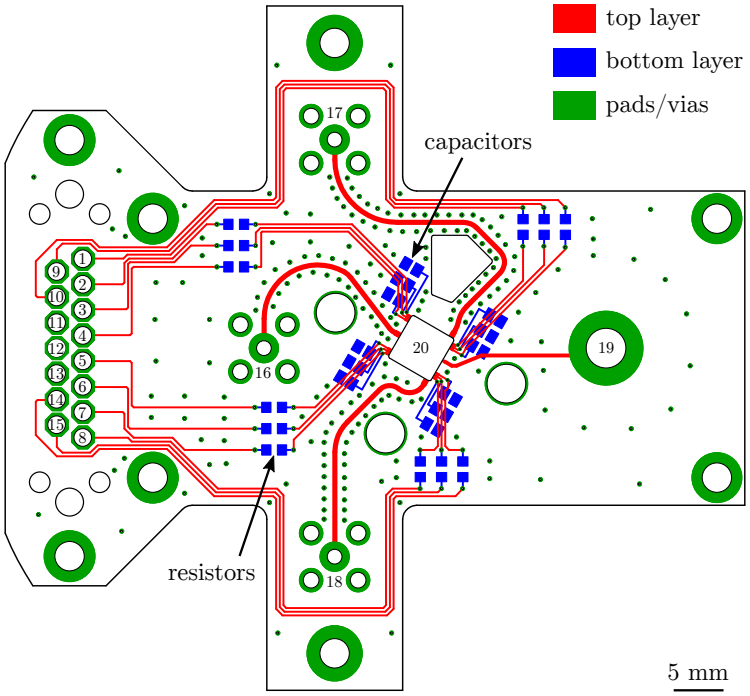

Figure A.3: Filterboard of the multi-layer trap. 1: DC9, 2: DC8, 3: DC7, 4: DC6, 5: DC5, 6: DC4, 7: DC3, 8: DC2, 9: DC10, 10: NC, 11: NC, 12: NC, 13: NC, 14: NC, 15: DC1, 16: MWM, 17: MWC_1, 18: MWC_2, 19: RF, 20: ion trap

A.3 Propagator calculations

As described in Sec. 2.4.2 we desire to calculate the exact propagator $\mathcal{U}(t)$ of the MS Hamiltonian of Eq. 2.24 in order to investigate the time evolution of an initially prepared state. For a short time step Δt and a starting time t_0, the corresponding propagator is given by

$$\begin{aligned}\mathcal{U}(\Delta t) &= e^{\left[\dot{\gamma}(t_0)a_j^\dagger - \dot{\gamma}^*(t_0)a_j\right]\Delta t} \\ &= \mathcal{D}(\dot{\gamma}(t_0)\Delta t)\end{aligned} \tag{A.1}$$

where we have defined

$$\dot{\gamma}(t_0) = -i\left(\frac{\Omega_g S_{\varphi_s}}{2}\right) e^{-i(\delta t_0 + \varphi_a)} \tag{A.2}$$

and used the unitary displacement operator $\mathcal{D}(\alpha) = e^{\alpha a_j^\dagger - \alpha^* a_j}$ which has the useful property that

$$\mathcal{D}(\alpha)\mathcal{D}(\beta) = \mathcal{D}(\alpha+\beta)e^{i\Im(\alpha\beta^*)}\ . \tag{A.3}$$

Dividing the time t into M multiple time intervals $\Delta\tilde{t} = t/M$ and defining $\tilde{t}_j = j \cdot \Delta\tilde{t}$, we can write

$$\begin{aligned}
\mathcal{U}(t) &\approx \mathcal{D}(\dot{\gamma}(\tilde{t}_M)\Delta\tilde{t}) \cdots \mathcal{D}(\dot{\gamma}(\tilde{t}_0)\Delta\tilde{t}) \\
&= \prod_{j=1}^{M} \mathcal{D}\left(\dot{\gamma}(\tilde{t}_{M-j})\Delta\tilde{t}\right) \\
&= \mathcal{D}\left(\sum_{j=1}^{M} \dot{\gamma}(\tilde{t}_{M-j})\Delta\tilde{t}\right) \prod_{j=1}^{M-1} e^{i\Im\left[\dot{\gamma}(\tilde{t}_j)\Delta\tilde{t}\sum_{k=0}^{j-1}\dot{\gamma}^*(\tilde{t}_k)\Delta\tilde{t}\right]} \\
&= \mathcal{D}\left(\sum_{j=1}^{M} \dot{\gamma}(\tilde{t}_j)\Delta\tilde{t}\right) e^{i\Im\left[\sum_{j=1}^{M-1}\dot{\gamma}(\tilde{t}_j)\Delta\tilde{t}\sum_{k=0}^{j-1}\dot{\gamma}^*(\tilde{t}_k)\Delta\tilde{t}\right]} .
\end{aligned} \tag{A.4}$$

Going to the limit of infinitesimal time steps $\Delta\tilde{t} \to dt$ translates the sums into integrals and yields

$$\mathcal{U}(t) = \mathcal{D}\left(\int_0^t \dot{\gamma}(t')\,dt'\right) e^{i\Im\left[\int_0^t \dot{\gamma}(t')\int_0^{t'}\dot{\gamma}^*(t'')\,dt''\,dt'\right]} \tag{A.5}$$

$$= \mathcal{D}\left(\gamma(t) - \gamma(0)\right) e^{i\Im\left[\int_0^t \dot{\gamma}(t')\cdot(\gamma^*(t')-\gamma^*(0))\,dt'\right]} . \tag{A.6}$$

In the following, both terms of the last equation will be treated separately. For the first term of the displacement operator and with the definition of $\dot{\gamma}(t)$ stated above, we can calculate

$$\gamma(t) = \int_0^t \dot{\gamma}(t')\,dt' \tag{A.7}$$

$$= -i\left(\frac{\Omega_g S_{\varphi_s}}{2}\right)\int_0^t e^{-i(\delta t'+\varphi_a)}\,dt' \tag{A.8}$$

$$= -i\left(\frac{\Omega_g S_{\varphi_s}}{2}\right)\left[\frac{ie^{-i(\delta t'+\varphi_a)}}{\delta}\right]_{t'=0}^{t'=t} \tag{A.9}$$

$$= -\left(\frac{\Omega_g S_{\varphi_s}}{2\delta}\right) e^{-i\varphi_a}\left(1 - e^{-i\delta t}\right) \tag{A.10}$$

$$= -\left(\frac{\Omega_g S_{\varphi_s}}{2\delta}\right) e^{-i\varphi_a} e^{-i\frac{1}{2}\delta t}\left(e^{+i\frac{1}{2}\delta t} - e^{-i\frac{1}{2}\delta t}\right) \tag{A.11}$$

$$= -i\left(\frac{\Omega_g S_{\varphi_s}}{\delta}\right) e^{-i\varphi_a} e^{-i\frac{1}{2}\delta t}\sin\left(\frac{1}{2}\delta t\right) \tag{A.12}$$

where we choose the integration constant such that $\gamma(0) = 0$. Consequently, the displacement operator term simplifies to $\mathcal{D}(\gamma(t))$. The exponent of the

remaining exponential term of Eq. A.6 now calculates to

$$
\begin{aligned}
& i\Im\left[\int_0^t \dot{\gamma}(t')\cdot(\gamma^*(t')-\gamma^*(0))\,dt'\right] \\
&= -i\Im\left[i\left(\frac{\Omega_g S_{\varphi_s}}{2}\right)^2 \frac{1}{\delta}\int_0^t e^{-i\delta t'}\left(e^{i\delta t'}-1\right)\,dt\right] \\
&= -i\Im\left[i\left(\frac{\Omega_g S_{\varphi_s}}{2}\right)^2 \frac{1}{\delta}\int_0^t \left(1-e^{-i\delta t'}\right)\,dt\right] \\
&= -i\Im\left[i\left(\frac{\Omega_g S_{\varphi_s}}{2}\right)^2 \frac{1}{\delta}\left(t+\frac{1}{i\delta}\left[e^{-i\delta t'}\right]_{t'=0}^{t'=t}\right)\right] \\
&= -i\Im\left[i\left(\frac{\Omega_g S_{\varphi_s}}{2}\right)^2 \frac{1}{\delta}\left(t+\frac{1}{i\delta}\left(e^{-i\delta t}-1\right)\right)\right] \\
&= -i\left(\frac{\Omega_g S_{\varphi_s}}{2\delta}\right)^2 \left(t+\frac{\sin(-\delta t)}{\delta}\right) \\
&= -i\left(\frac{\Omega_g S_{\varphi_s}}{2\delta}\right)^2 (t\delta-\sin(\delta t))\ .
\end{aligned}
\tag{A.13}
$$

Finally, merging both obtained expressions back into Eq. A.6 yields

$$
\mathcal{U}(t)=\mathcal{D}(\gamma(t))\exp\left[-i\left(\frac{\Omega_g S_{\varphi_s}}{2\delta}\right)^2 (t\delta-\sin(\delta t))\right] \tag{A.14}
$$

which is identical to the expression of Eq. 2.32 used in the main text.

Bibliography

[ABH+05] M. Acton, K.-A. Brickman, P. C. Haljan, P. J. Lee, L. Deslauriers, and C. Monroe. Near-Perfect Simultaneous Measurement of a Qubit Register. *arXiv:quant-ph/0511257*, November 2005. arXiv: quant-ph/0511257.

[AGH+11] D T C Allcock, L Guidoni, T P Harty, C J Ballance, M G Blain, A M Steane, and D M Lucas. Reduction of heating rate in a microfabricated ion trap by pulsed-laser cleaning. *New Journal of Physics*, 13(12):123023, December 2011.

[AHB+13] D. T. C. Allcock, T. P. Harty, C. J. Ballance, B. C. Keitch, N. M. Linke, D. N. Stacey, and D. M. Lucas. A microfabricated ion trap with integrated microwave circuitry. *Applied Physics Letters*, 102(4):044103–044103–4, January 2013.

[AUW+10] J M Amini, H Uys, J H Wesenberg, S Seidelin, J Britton, J J Bollinger, D Leibfried, C Ospelkaus, A P VanDevender, and D J Wineland. Toward scalable ion traps for quantum information processing. *New Journal of Physics*, 12(3):033031, March 2010.

[Bal17] Christopher J. Ballance. *High-Fidelity Quantum Logic in Ca+*. Springer Theses. Springer International Publishing, Cham, 2017.

[BBC+95] Adriano Barenco, Charles H. Bennett, Richard Cleve, David P. DiVincenzo, Norman Margolus, Peter Shor, Tycho Sleator, John A. Smolin, and Harald Weinfurter. Elementary gates for quantum computation. *Physical Review A*, 52(5):3457, November 1995.

[BDS+03] M. D. Barrett, B. DeMarco, T. Schaetz, V. Meyer, D. Leibfried, J. Britton, J. Chiaverini, W. M. Itano, B. Jelenković, J. D. Jost, C. Langer, T. Rosenband, and D. J. Wineland. Sympathetic cooling of 9be+ and 24mg+ for quantum logic. *Physical Review A*, 68(4):042302, October 2003.

[Ber84] Berry Michael Victor. Quantal phase factors accompanying adiabatic changes. *Proceedings of the Royal Society of London. A. Mathematical and Physical Sciences*, 392(1802):45–57, March 1984.

[BGL+12] R. Bowler, J. Gaebler, Y. Lin, T. R. Tan, D. Hanneke, J. D. Jost, J. P. Home, D. Leibfried, and D. J. Wineland. Coherent Diabatic Ion Transport and Separation in a Multizone Trap Array. *Physical Review Letters*, 109(8):080502, August 2012.

[BHIW86] J. C. Bergquist, Randall G. Hulet, Wayne M. Itano, and D. J. Wineland. Observation of Quantum Jumps in a Single Atom. *Physical Review Letters*, 57(14):1699–1702, October 1986.

[BHL+16] C. J. Ballance, T. P. Harty, N. M. Linke, M. A. Sepiol, and D. M. Lucas. High-Fidelity Quantum Logic Gates Using Trapped-Ion Hyperfine Qubits. *Physical Review Letters*, 117(6):060504, August 2016.

[BKRB08] Jan Benhelm, Gerhard Kirchmair, Christian F. Roos, and Rainer Blatt. Towards fault-tolerant quantum computing with trapped ions. *Nat Phys*, 4(6):463–466, June 2008.

[BKW18] Ivan A. Boldin, Alexander Kraft, and Christof Wunderlich. Measuring anomalous heating in a planar ion trap with variable ion-surface separation. *Physical Review Letters*, 120(2), January 2018. arXiv: 1708.03147.

[Bla10] R.B. Blakestad. *Transport of Trapped-Ion Qubits within a Scalable Quantum Processor*. PhD Thesis, University of Colorado, 2010.

[BLLO83] G. C. Bjorklund, M. D. Levenson, W. Lenth, and C. Ortiz. Frequency modulation (FM) spectroscopy. *Applied Physics B*, 32(3):145–152, November 1983.

[BMB+98] D. J. Berkeland, J. D. Miller, J. C. Bergquist, W. M. Itano, and D. J. Wineland. Minimization of ion micromotion in a Paul trap. *Journal of Applied Physics*, 83(10):5025, 1998.

[BOV+09] R. B. Blakestad, C. Ospelkaus, A. P. VanDevender, J. M. Amini, J. Britton, D. Leibfried, and D. J. Wineland. High-Fidelity Transport of Trapped-Ion Qubits through an X-Junction Trap Array. *Physical Review Letters*, 102(15):153002, April 2009.

[Bow15] Ryan Bowler. *Coherent Ion Transport in a Multi-electrode Trap Array.* PhD thesis, University of Colorado, 2015.

[BSZH+19] A. Bautista-Salvador, G. Zarantonello, H. Hahn, A. Preciado-Grijalva, J. Morgner, M. Wahnschaffe, and C. Ospelkaus. Multilayer ion trap technology for scalable quantum computing and quantum simulation. *New Journal of Physics*, 21(4):043011, April 2019.

[BWB+13] R. Bowler, U. Warring, J. W. Britton, B. C. Sawyer, and J. Amini. Arbitrary waveform generator for quantum information processing with trapped ions. *Review of Scientific Instruments*, 84(3):033108–033108–6, March 2013.

[BWC+11] K. R. Brown, A. C. Wilson, Y. Colombe, C. Ospelkaus, A. M. Meier, E. Knill, D. Leibfried, and D. J. Wineland. Single-qubit gate error below 10ˆ{-4} in a trapped ion. *Physical Review A*, 84(3):030303, 2011.

[BWWI85] J. J. Bollinger, J. S. Wells, D. J. Wineland, and Wayne M. Itano. Hyperfine structure of the 2p 2p_{1/2} state in 9be+. *Physical Review A*, 31(4):2711–2714, April 1985.

[CBB+05] J. Chiaverini, R.B. Blakestade, J. Britton, J.D. Jost, C. Langer, D. Leibfried, and D.J. Wineland. Surface-electrode architecture for ion-trap quantum information processing. *Quantum Information and Computation*, 5(6):419–439, 2005.

[CEC98] O. Chubar, P. Elleaume, and J. Chavanne. A three-dimensional magnetostatics computer code for insertion devices. *Journal of Synchrotron Radiation*, 5(3):481–484, May 1998.

[CKDO14] M. Carsjens, M. Kohnen, T. Dubielzig, and C. Ospelkaus. Surface-electrode Paul trap with optimized near-field microwave control. *Applied Physics B*, 114(1-2):243–250, 2014.

[CLH+14] D. P. L. Aude Craik, N. M. Linke, T. P. Harty, C. J. Ballance, D. M. Lucas, A. M. Steane, and D. T. C. Allcock. Microwave control electrodes for scalable, parallel, single-qubit operations in a surface-electrode ion trap. *Applied Physics B*, 114(1-2):3–10, January 2014.

[CLS+17] D. P. L. Aude Craik, N. M. Linke, M. A. Sepiol, T. P. Harty, J. F. Goodwin, C. J. Ballance, D. N. Stacey, A. M. Steane, D. M. Lucas, and D. T. C. Allcock. High-fidelity spatial and polarization addressing of 43ca+ qubits using near-field microwave control. *Physical Review A*, 95(2):022337, February 2017.

[CN97] Isaac L. Chuang and M. A. Nielsen. Prescription for experimental determination of the dynamics of a quantum black box. *Journal of Modern Optics*, 44(11-12):2455–2467, November 1997.

[CS14] J. Chiaverini and J. M. Sage. Insensitivity of the rate of ion motional heating to trap-electrode material over a large temperature range. *Physical Review A*, 89(1):012318, January 2014.

[CZ95] J. I. Cirac and P. Zoller. Quantum Computations with Cold Trapped Ions. *Physical Review Letters*, 74(20):4091, May 1995.

[DGB+14] N. Daniilidis, S. Gerber, G. Bolloten, M. Ramm, A. Ransford, E. Ulin-Avila, I. Talukdar, and H. Häffner. Surface noise analysis using a single-ion sensor. *Physical Review B*, 89(24):245435, June 2014.

[DHK+83] R. W. P. Drever, J. L. Hall, F. V. Kowalski, J. Hough, G. M. Ford, A. J. Munley, and H. Ward. Laser phase and frequency stabilization using an optical resonator. *Applied Physics B*, 31(2):97–105, June 1983.

[DiV95] David P. DiVincenzo. Two-bit gates are universal for quantum computation. *Physical Review A*, 51(2):1015–1022, February 1995.

[DiV00] David P. DiVincenzo. The Physical Implementation of Quantum Computation. *Fortschritte der Physik*, 48(9-11):771–783, September 2000.

[DLF+16] S. Debnath, N. M. Linke, C. Figgatt, K. A. Landsman, K. Wright, and C. Monroe. Demonstration of a small programmable quantum computer with atomic qubits. *Nature*, 536(7614):63–66, August 2016.

[DOS+06] L. Deslauriers, S. Olmschenk, D. Stick, W. K. Hensinger, J. Sterk, and C. Monroe. Scaling and Suppression of Anomalous Heating in Ion Traps. *Physical Review Letters*, 97(10):103007, 2006.

[DP85] David Deutsch and Penrose Roger. Quantum theory, the Church–Turing principle and the universal quantum computer. *Proceedings of the Royal Society of London. A. Mathematical and Physical Sciences*, 400(1818):97–117, July 1985.

[ECC97] P. Elleaume, O. Chubar, and J. Chavanne. Computing 3d magnetic fields from insertion devices. In *Proceedings of the 1997 Particle Accelerator Conference (Cat. No.97CH36167)*, volume 3, pages 3509–3511 vol.3, May 1997.

[Fey82] Richard P. Feynman. Simulating physics with computers. *International Journal of Theoretical Physics*, 21(6-7):467–488, June 1982.

[FML+17] C. Figgatt, D. Maslov, K. A. Landsman, N. M. Linke, S. Debnath, and C. Monroe. Complete 3-Qubit Grover search on a programmable quantum computer. *Nature Communications*, 8(1):1918, December 2017.

[FSL+95] P. T. H. Fisk, M. J. Sellars, M. A. Lawn, C. Coles, A. G. Mann, and D. G. Blair. Very high Q microwave spectroscopy on trapped 171yb+ ions: application as a frequency standard. *IEEE Transactions on Instrumentation and Measurement*, 44(2):113–116, April 1995.

[GFW+14] F. Gebert, M. H. Frosz, T. Weiss, Y. Wan, A. Ermolov, N. Y. Joly, P. O. Schmidt, and P. St J. Russell. Damage-free single-

mode transmission of deep-UV light in hollow-core PCF. *Optics Express*, 22(13):15388–15396, June 2014.

[GMT+12] J. P. Gaebler, A. M. Meier, T. R. Tan, R. Bowler, Y. Lin, D. Hanneke, J. D. Jost, J. P. Home, E. Knill, D. Leibfried, and D. J. Wineland. Randomized Benchmarking of Multiqubit Gates. *Physical Review Letters*, 108(26):260503, June 2012.

[Gro97] Lov K. Grover. Quantum Mechanics Helps in Searching for a Needle in a Haystack. *Physical Review Letters*, 79(2):325–328, July 1997.

[Gro12] Sebastian Grondkowski. *Pulsgenerator für die Quanteninformationsverarbeitung mit einzelnen gespeicherten Ionen.* Bachelor's Thesis, Gottfried Wilhelm Leibniz Universität Hannover, Hannover, 2012.

[Gro14] Sebastian Grondkowski. Quantenkontrolle von 9be+ Hyperfein-Qubits. Master's thesis, Gottfried Wilhelm Leibniz Universität Hannover, Hannover, 2014.

[GSHV14] Genko T. Genov, Daniel Schraft, Thomas Halfmann, and Nikolay V. Vitanov. Correction of Arbitrary Field Errors in Population Inversion of Quantum Systems by Universal Composite Pulses. *Physical Review Letters*, 113(4):043001, July 2014.

[GTL+16] J. P. Gaebler, T. R. Tan, Y. Lin, Y. Wan, R. Bowler, A. C. Keith, S. Glancy, K. Coakley, E. Knill, D. Leibfried, and D. J. Wineland. High-Fidelity Universal Gate Set for 9be+ Ion Qubits. *Physical Review Letters*, 117(6):060505, August 2016.

[HAB+14] T. P. Harty, D. T. C. Allcock, C. J. Ballance, L. Guidoni, H. A. Janacek, N. M. Linke, D. N. Stacey, and D. M. Lucas. High-Fidelity Preparation, Gates, Memory, and Readout of a Trapped-Ion Quantum Bit. *Physical Review Letters*, 113(22):220501, November 2014.

[Har13] Thomas Harty. *High-Fidelity Microwave-Driven Quantum Logic in Intermediate-Field 43Ca+.* PhD thesis, Oxford, 2013.

[HC80] T. W. Hänsch and B. Couillaud. Laser frequency stabilization by polarization spectroscopy of a reflecting reference cavity. *Optics Communications*, 35(3):441–444, December 1980.

[HCD+12] D. Hayes, S. M. Clark, S. Debnath, D. Hucul, I. V. Inlek, K. W. Lee, Q. Quraishi, and C. Monroe. Coherent Error Suppression in Multiqubit Entangling Gates. *Physical Review Letters*, 109(2):020503, 2012.

[HCW+12] D. A. Hite, Y. Colombe, A. C. Wilson, K. R. Brown, U. Warring, R. Jördens, J. D. Jost, K. S. McKay, D. P. Pappas, D. Leibfried, and D. J. Wineland. 100-Fold Reduction of Electric-Field Noise in an Ion Trap Cleaned with In Situ Argon-Ion-Beam Bombardment. *Physical Review Letters*, 109(10):103001, September 2012.

[HGH+07] R. J. Hendricks, D. M. Grant, P. F. Herskind, A. Dantan, and M. Drewsen. An all-optical ion-loading technique for scalable microtrap architectures. *Applied Physics B*, 88(4):507–513, June 2007.

[HHJ+09] Jonathan P. Home, David Hanneke, John D. Jost, Jason M. Amini, Dietrich Leibfried, and David J. Wineland. Complete Methods Set for Scalable Ion Trap Quantum Information Processing. *Science*, 325(5945):1227–1230, September 2009.

[HKW+18] Frederick Hakelberg, Philip Kiefer, Matthias Wittemer, Tobias Schaetz, and Ulrich Warring. Hybrid setup for stable magnetic fields enabling robust quantum control. *Scientific Reports*, 8(1):4404, March 2018.

[HMF+18] S. Hannig, J. Mielke, J. A. Fenske, M. Misera, N. Beev, C. Ospelkaus, and P. O. Schmidt. A highly stable monolithic enhancement cavity for second harmonic generation in the ultraviolet. *Review of Scientific Instruments*, 89(1):013106, January 2018.

[Hom06] Jonathan Home. *Entanglement of Two Trapped-Ion Spin Qubits*. PhD thesis, Oxford, 2006.

[HOS+06] W. K. Hensinger, S. Olmschenk, D. Stick, D. Hucul, M. Yeo, M. Acton, L. Deslauriers, C. Monroe, and J. Rabchuk. T-junction ion trap array for two-dimensional ion shuttling, storage, and

manipulation. *Applied Physics Letters*, 88(3):034101–034101–3, January 2006.

[HSA+16] T. P. Harty, M. A. Sepiol, D. T. C. Allcock, C. J. Ballance, J. E. Tarlton, and D. M. Lucas. High-Fidelity Trapped-Ion Quantum Logic Using Near-Field Microwaves. *Physical Review Letters*, 117(14):140501, September 2016.

[HZBS+18] Henning Hahn, Giorgio Zarantonello, Amado Bautista-Salvador, Martina Wahnschaffe, Matthias Kohnen, Joerg Schoebel, Piet O. Schmidt, and Christian Ospelkaus. Multilayer ion trap with 3-dimensional microwave circuitry for scalable quantum logic applications. *arXiv:1812.02445 [quant-ph]*, December 2018. arXiv: 1812.02445.

[HZS+19] Henning Hahn, Giorgio Zarantonello, Marius Schulte, Amado Bautista-Salvador, Klemens Hammerer, and Christian Ospelkaus. Integrated 9be+ multi-qubit gate device for the ion-trap quantum computer. *arXiv:1902.07028 [quant-ph]*, February 2019. arXiv: 1902.07028.

[Jac17] Frederik Jacobs. *Realisierung langlebiger Qubit-Zustände in 9Be+-Ionen*. Bachelor's Thesis, Leibniz Universität Hannover, November 2017.

[Jam98a] Daniel F. V. James. Theory of Heating of the Quantum Ground State of Trapped Ions. *Physical Review Letters*, 81(2):317–320, July 1998.

[Jam98b] D.F.V. James. Quantum dynamics of cold trapped ions with application to quantum computation. *Applied Physics B: Lasers and Optics*, 66(2):181–190, February 1998.

[JBT+09] M. Johanning, A. Braun, N. Timoney, V. Elman, W. Neuhauser, and Chr. Wunderlich. Individual Addressing of Trapped Ions and Coupling of Motional and Spin States Using rf Radiation. *Physical Review Letters*, 102(7):073004, February 2009.

[JHA+09] J. D. Jost, J. P. Home, J. M. Amini, D. Hanneke, R. Ozeri, C. Langer, J. J. Bollinger, D. Leibfried, and D. J. Wineland. En-

tangled mechanical oscillators. *Nature*, 459(7247):683–685, June 2009.

[JMBW95] S. R. Jefferts, C. Monroe, E. W. Bell, and D. J. Wineland. Coaxial-resonator-driven rf (Paul) trap for strong confinement. *Physical Review A*, 51(4):3112, April 1995.

[JWCR+16] K. G. Johnson, J. D. Wong-Campos, A. Restelli, K. A. Landsman, B. Neyenhuis, J. Mizrahi, and C. Monroe. Active stabilization of ion trap radiofrequency potentials. *Review of Scientific Instruments*, 87(5):053110, May 2016.

[Kin99] Brian E. King. *Quantum State Engineering and Information Processing with Trapped Ions*. PhD thesis, University of Colorado, Boulder, 1999.

[KKM+00] D. Kielpinski, B. E. King, C. J. Myatt, C. A. Sackett, Q. A. Turchette, W. M. Itano, C. Monroe, D. J. Wineland, and W. H. Zurek. Sympathetic cooling of trapped ions for quantum logic. *Physical Review A*, 61(3):032310, February 2000.

[KLR+08] E. Knill, D. Leibfried, R. Reichle, J. Britton, R. B. Blakestad, J. D. Jost, C. Langer, R. Ozeri, S. Seidelin, and D. J. Wineland. Randomized benchmarking of quantum gates. *Physical Review A*, 77(1):012307, January 2008.

[KM97] A. Kramida and W. C. Martin. A Compilation of energy Levels and Wavelengths for Spectrum of Neutral Beryllium (Be I). *J. Phys. Chem. Ref. Data*, 26:1185, 1997.

[KMW02] D. Kielpinski, C. Monroe, and D. J. Wineland. Architecture for a large-scale ion-trap quantum computer. *Nature*, 417(6890):709–711, June 2002.

[Kni10] Emanuel Knill. Physics: Quantum computing. *Nature*, 463:441–443, January 2010.

[KPS+12] A. Khromova, Ch. Piltz, B. Scharfenberger, T. F. Gloger, M. Johanning, A. F. Varón, and Ch. Wunderlich. Designer Spin Pseudomolecule Implemented with Trapped Ions in a Magnetic Gradient. *Physical Review Letters*, 108(22):220502, June 2012.

[KWM+98] B. E. King, C. S. Wood, C. J. Myatt, Q. A. Turchette, D. Leibfried, W. M. Itano, C. Monroe, and D. J. Wineland. Cooling the Collective Motion of Trapped Ions to Initialize a Quantum Register. *Physical Review Letters*, 81(7):1525, 1998.

[LAK+13] Hsiang-Yu Lo, Joseba Alonso, Daniel Kienzler, Benjamin C. Keitch, Ludwig E. de Clercq, Vlad Negnevitsky, and Jonathan P. Home. All-solid-state continuous-wave laser systems for ionization, cooling and quantum state manipulation of beryllium ions. *Applied Physics B*, 114(1-2):17–25, September 2013.

[Lan06] Christopher E. Langer. *High Fidelity Quantum Information Processing with Trapped Ions*. PhD Thesis, University of Colorado, Boulder, Colorado, 2006.

[LCL+07] David R. Leibrandt, Robert J. Clark, Jaroslaw Labaziewicz, Paul Antohi, Waseem Bakr, Kenneth R. Brown, and Isaac L. Chuang. Laser ablation loading of a surface-electrode ion trap. *Physical Review A*, 76(5):055403, November 2007.

[LDM+03] D. Leibfried, B. DeMarco, V. Meyer, D. Lucas, M. Barrett, J. Britton, W. M. Itano, B. Jelenkovic, C. Langer, T. Rosenband, and D. J. Wineland. Experimental demonstration of a robust, high-fidelity geometric two ion-qubit phase gate. *Nature*, 422(6930):412–415, March 2003.

[LGL+08] Jaroslaw Labaziewicz, Yufei Ge, David R. Leibrandt, Shannon X. Wang, Ruth Shewmon, and Isaac L. Chuang. Temperature Dependence of Electric Field Noise above Gold Surfaces. *Physical Review Letters*, 101(18), October 2008.

[LJL+10] T. D. Ladd, F. Jelezko, R. Laflamme, Y. Nakamura, C. Monroe, and J. L. O'Brien. Quantum computers. *Nature*, 464(7285):45–53, March 2010.

[Lo15] Hsiang-Yu Lo. *Creation of Squeezed Schrödinger's Cat States in a Mixed-Species Ion Trap*. PhD thesis, ETH Zürich, 2015.

[LOJ+05] C. Langer, R. Ozeri, J. D. Jost, J. Chiaverini, B. DeMarco, A. Ben-Kish, R. B. Blakestad, J. Britton, D. B. Hume, W. M. Itano, D. Leibfried, R. Reichle, T. Rosenband, T. Schaetz, P. O.

Schmidt, and D. J. Wineland. Long-Lived Qubit Memory Using Atomic Ions. *Physical Review Letters*, 95(6):060502, 2005.

[MBM+16] Karan K. Mehta, Colin D. Bruzewicz, Robert McConnell, Rajeev J. Ram, Jeremy M. Sage, and John Chiaverini. Integrated optical addressing of an ion qubit. *Nature Nanotechnology*, 11(12):1066–1070, December 2016.

[MECZ99] G. Morigi, J. Eschner, J. I. Cirac, and P. Zoller. Laser cooling of two trapped ions: Sideband cooling beyond the Lamb-Dicke limit. *Physical Review A*, 59(5):3797–3808, May 1999.

[MHS+11] D. L. Moehring, C. Highstrete, D. Stick, K. M. Fortier, R. Haltli, C. Tigges, and M. G. Blain. Design, fabrication and experimental demonstration of junction surface ion traps. *New Journal of Physics*, 13(7):075018, 2011.

[MK13] C. Monroe and J. Kim. Scaling the Ion Trap Quantum Processor. *Science*, 339(6124):1164–1169, March 2013.

[MNM+16] Thomas Monz, Daniel Nigg, Esteban A. Martinez, Matthias F. Brandl, Philipp Schindler, Richard Rines, Shannon X. Wang, Isaac L. Chuang, and Rainer Blatt. Realization of a scalable Shor algorithm. *Science*, 351(6277):1068–1070, March 2016.

[MRR+14] C. Monroe, R. Raussendorf, A. Ruthven, K. R. Brown, P. Maunz, L.-M. Duan, and J. Kim. Large-scale modular quantum-computer architecture with atomic memory and photonic interconnects. *Physical Review A*, 89(2), February 2014.

[MS99] Klaus Mølmer and Anders Sørensen. Multiparticle Entanglement of Hot Trapped Ions. *Physical Review Letters*, 82(9):1835, March 1999.

[MSJ00] G.J. Milburn, S. Schneider, and D.F.V. James. Ion Trap Quantum Computing with Warm Ions. *Fortschritte der Physik*, 48(9-11):801–810, September 2000.

[MVL+11] J. True Merrill, Curtis Volin, David Landgren, Jason M. Amini, Kenneth Wright, S. Charles Doret, C-S Pai, Harley Hayden, Tyler Killian, Daniel Faircloth, Kenneth R. Brown, Alexa W. Harter,

and Richart E. Slusher. Demonstration of integrated microscale optics in surface-electrode ion traps. *New Journal of Physics*, 13(10):103005, 2011.

[MW01] Florian Mintert and Christof Wunderlich. Ion-Trap Quantum Logic Using Long-Wavelength Radiation. *Physical Review Letters*, 87(25):257904, November 2001.

[NMM+18] V. Negnevitsky, M. Marinelli, K. K. Mehta, H.-Y. Lo, C. Flühmann, and J. P. Home. Repeated multi-qubit readout and feedback with a mixed-species trapped-ion register. *Nature*, page 1, November 2018.

[noa16] QuTiP: Quantum tool box in PYTHON, 2016.

[NSD86] Warren Nagourney, Jon Sandberg, and Hans Dehmelt. Shelved optical electron amplifier: Observation of quantum jumps. *Physical Review Letters*, 56(26):2797–2799, June 1986.

[OIB+07] R. Ozeri, W. M. Itano, R. B. Blakestad, J. Britton, J. Chiaverini, J. D. Jost, C. Langer, D. Leibfried, R. Reichle, S. Seidelin, J. H. Wesenberg, and D. J. Wineland. Errors in trapped-ion quantum gates due to spontaneous photon scattering. *Physical Review A*, 75(4):042329, April 2007.

[OLA+08] C. Ospelkaus, C. E. Langer, J. M. Amini, K. R. Brown, D. Leibfried, and D. J. Wineland. Trapped-Ion Quantum Logic Gates Based on Oscillating Magnetic Fields. *Physical Review Letters*, 101(9):090502, 2008.

[OLJ+05] R. Ozeri, C. Langer, J. D. Jost, B. DeMarco, A. Ben-Kish, B. R. Blakestad, J. Britton, J. Chiaverini, W. M. Itano, D. B. Hume, D. Leibfried, T. Rosenband, P. O. Schmidt, and D. J. Wineland. Hyperfine Coherence in the Presence of Spontaneous Photon Scattering. *Physical Review Letters*, 95(3):030403, July 2005.

[OM01] Mário H Oliveira and José A Miranda. Biot-Savart-like law in electrostatics. *European Journal of Physics*, 22:31, 2001.

[Osp16] C. Ospelkaus. Microwave quantum control notes. *private communication*, 2016.

[OWC+11] C. Ospelkaus, U. Warring, Y. Colombe, K. R. Brown, J. M. Amini, D. Leibfried, and D. J. Wineland. Microwave quantum logic gates for trapped ions. *Nature*, 476(7359):181–184, 2011.

[OYM+07] S. Olmschenk, K. C. Younge, D. L. Moehring, D. N. Matsukevich, P. Maunz, and C. Monroe. Manipulation and detection of a trapped Yb+ hyperfine qubit. *Physical Review A*, 76(5), November 2007.

[PAS75] O. Poulsen, T. Andersen, and N. J. Skouboe. Fast-beam, zero-field level-crossing measurements of radiative lifetimes, fine and hyperfine structures in excited states of ionic and neutral beryllium. *Journal of Physics B: Atomic and Molecular Physics*, 8(9):1393, 1975.

[Pau90] Wolfgang Paul. Electromagnetic traps for charged and neutral particles. *Reviews of Modern Physics*, 62(3):531–542, 1990.

[PCZ97] J. F. Poyatos, J. I. Cirac, and P. Zoller. Complete Characterization of a Quantum Process: The Two-Bit Quantum Gate. *Physical Review Letters*, 78(2):390–393, January 1997.

[Pre98] Preskill John. Reliable quantum computers. *Proceedings of the Royal Society of London. Series A: Mathematical, Physical and Engineering Sciences*, 454(1969):385–410, January 1998.

[RKM+01] M. A. Rowe, D. Kielpinski, V. Meyer, C. A. Sackett, W. M. Itano, C. Monroe, and D. J. Wineland. Experimental violation of a Bell's inequality with efficient detection. *Nature*, 409(6822):791–794, February 2001.

[RKS+06] M. Riebe, K. Kim, P. Schindler, T. Monz, P. O. Schmidt, T. K. Körber, W. Hänsel, H. Häffner, C. F. Roos, and R. Blatt. Process Tomography of Ion Trap Quantum Gates. *Physical Review Letters*, 97(22):220407, December 2006.

[RSK+16] T. Ruster, C. T. Schmiegelow, H. Kaufmann, C. Warschburger, F. Schmidt-Kaler, and U. G. Poschinger. A long-lived Zeeman trapped-ion qubit. *Applied Physics B*, 122(10), October 2016.

[SBS+19] R. Srinivas, S. C. Burd, R. T. Sutherland, A. C. Wilson, D. J. Wineland, D. Leibfried, D. T. C. Allcock, and D. H. Slichter. Trapped-Ion Spin-Motion Coupling with Microwaves and a Near-Motional Oscillating Magnetic Field Gradient. *Physical Review Letters*, 122(16):163201, April 2019.

[SCR+06] S. Seidelin, J. Chiaverini, R. Reichle, J. J. Bollinger, D. Leibfried, J. Britton, J. H. Wesenberg, R. B. Blakestad, R. J. Epstein, D. B. Hume, W. M. Itano, J. D. Jost, C. Langer, R. Ozeri, N. Shiga, and D. J. Wineland. Microfabricated Surface-Electrode Ion Trap for Scalable Quantum Information Processing. *Physical Review Letters*, 96(25):253003, June 2006.

[SdMFZ99] E. Solano, R. L. de Matos Filho, and N. Zagury. Deterministic Bell states and measurement of the motional state of two trapped ions. *Physical Review A*, 59(4):R2539, April 1999.

[Sep16] M. A. Sepiol. *A high-fidelity microwave driven two-qubit quantum logic gate in 43Ca+*. PhD thesis, Oxford, 2016.

[SGS+18] J. A. Sedlacek, A. Greene, J. Stuart, R. McConnell, C. D. Bruzewicz, J. M. Sage, and J. Chiaverini. Distance scaling of electric-field noise in a surface-electrode ion trap. *Physical Review A*, 97(2):020302, February 2018.

[SGWW18] Theeraphot Sriarunothai, Gouri Shankar Giri, Sabine Wölk, and Christof Wunderlich. Radio frequency sideband cooling and sympathetic cooling of trapped ions in a static magnetic field gradient. *Journal of Modern Optics*, 65(5-6):560–567, March 2018.

[Sho94] P. W. Shor. Algorithms for quantum computation: Discrete logarithms and factoring. In *Proc. 35th Annual Symposium on Foundations of Computer Science*, pages 124–134, Los Alamitos, 1994. IEEE Computer Society Press.

[SKHR+03] Ferdinand Schmidt-Kaler, Hartmut Häffner, Mark Riebe, Stephan Gulde, Gavin P. T. Lancaster, Thomas Deuschle, Christoph Becher, Christian F. Roos, Jürgen Eschner, and Rainer Blatt. Realization of the Cirac–Zoller controlled-NOT quantum gate. *Nature*, 422(6930):408–411, March 2003.

[SKK+00] C. A. Sackett, D. Kielpinski, B. E. King, C. Langer, V. Meyer, C. J. Myatt, M. Rowe, Q. A. Turchette, W. M. Itano, D. J. Wineland, and C. Monroe. Experimental entanglement of four particles. *Nature*, 404(6775):256–259, March 2000.

[SM99] Anders Sørensen and Klaus Mølmer. Quantum Computation with Ions in Thermal Motion. *Physical Review Letters*, 82(9):1971–1974, March 1999.

[SM00] Anders Sørensen and Klaus Mølmer. Entanglement and quantum computation with ions in thermal motion. *Physical Review A*, 62(2):022311, July 2000.

[SNBT86] Th. Sauter, W. Neuhauser, R. Blatt, and P. E. Toschek. Observation of Quantum Jumps. *Physical Review Letters*, 57(14):1696–1698, October 1986.

[Ste14] Mariia Stepanova. *Laser frequency stabilization for quantum logic experiments with single trapped 9Be+ ions*. Bachelor's Thesis, Leibniz Universitaet Hannover, December 2014.

[SVL+17] D. H. Slichter, V. B. Verma, D. Leibfried, R. P. Mirin, S. W. Nam, and D. J. Wineland. UV-sensitive superconducting nanowire single photon detectors for integration in an ion trap. *Optics Express*, 25(8):8705–8720, April 2017.

[TKK+00] Q. A. Turchette, Kielpinski, B. E. King, D. Leibfried, D. M. Meekhof, C. J. Myatt, M. A. Rowe, C. A. Sackett, C. S. Wood, W. M. Itano, C. Monroe, and D. J. Wineland. Heating of trapped ions from the quantum ground state. *Physical Review A*, 61(6):063418, May 2000.

[TV11] Boyan T. Torosov and Nikolay V. Vitanov. Smooth composite pulses for high-fidelity quantum information processing. *Physical Review A*, 83(5):053420, May 2011.

[TWK+98] Q. A. Turchette, C. S. Wood, B. E. King, C. J. Myatt, D. Leibfried, W. M. Itano, C. Monroe, and D. J. Wineland. Deterministic Entanglement of Two Trapped Ions. *Physical Review Letters*, 81(17):3631–3634, October 1998.

[Ude15] Fabian Ude. *Abbildungsoptik für einzelne 9Be+ Ionen*. Bachelor's Thesis, Leibniz Universität Hannover, Hannover, 2015.

[WAF+13] Kenneth Wright, Jason M. Amini, Daniel L. Faircloth, Curtis Volin, S. Charles Doret, Harley Hayden, C-S Pai, David W. Landgren, Douglas Denison, Tyler Killian, Richart E. Slusher, and Alexa W. Harter. Reliable transport through a microfabricated X -junction surface-electrode ion trap. *New Journal of Physics*, 15(3):033004, 2013.

[Wah16] Martina Wahnschaffe. *Engineered microwave control for trapped ions*. Dissertation, Gottfried Wilhelm Leibniz Universität, Hannover, June 2016.

[WBI83] D. J. Wineland, J. J. Bollinger, and Wayne M. Itano. Laser-Fluorescence Mass Spectroscopy. *Physical Review Letters*, 50(9):628, February 1983.

[Web05] Simon Webster. *Raman sideband cooling and coherent manipulation of trapped ions*. PhD thesis, Oxford, 2005.

[Wes08] J. H. Wesenberg. Electrostatics of surface-electrode ion traps. *Physical Review A*, 78(6):063410, December 2008.

[WHZ+17] M. Wahnschaffe, H. Hahn, G. Zarantonello, T. Dubielzig, S. Grondkowski, A. Bautista-Salvador, M. Kohnen, and C. Ospelkaus. Single-ion microwave near-field quantum sensor. *Applied Physics Letters*, 110(3):034103, January 2017.

[WIBH87] D. J. Wineland, Wayne M. Itano, J. C. Bergquist, and Randall G. Hulet. Laser-cooling limits and single-ion spectroscopy. *Physical Review A*, 36(5):2220–2232, September 1987.

[WMI+98] D.J. Wineland, C. Monroe, W.M. Itano, B.E. King, D. Leibfried, D.M. Meekhof, C. Myatt, and C. Wood. Experimental Primer on the Trapped Ion Quantum Computer. *Fortschritte der Physik*, 46(4-5):363–390, June 1998.

[WOC+13a] U. Warring, C. Ospelkaus, Y. Colombe, K. R. Brown, J. M. Amini, M. Carsjens, D. Leibfried, and D. J. Wineland. Techniques for microwave near-field quantum control of trapped ions. *Physical Review A*, 87(1):013437, January 2013.

[WOC+13b] U. Warring, C. Ospelkaus, Y. Colombe, R. Jördens, D. Leibfried, and D. J. Wineland. Individual-Ion Addressing with Microwave Field Gradients. *Physical Review Letters*, 110(17):173002, April 2013.

[WOV+11] A. C. Wilson, C. Ospelkaus, A. P. VanDevender, J. A. Mlynek, K. R. Brown, D. Leibfried, and D. J. Wineland. A 750-mW, continuous-wave, solid-state laser source at 313 nm for cooling and manipulating trapped 9be+ ions. *Applied Physics B*, 105(4):741–748, December 2011.

[WRW+15] S. Weidt, J. Randall, S. C. Webster, E. D. Standing, A. Rodriguez, A. E. Webb, B. Lekitsch, and W. K. Hensinger. Ground-State Cooling of a Trapped Ion Using Long-Wavelength Radiation. *Physical Review Letters*, 115(1):013002, June 2015.

[ZPH+17] J. Zhang, G. Pagano, P. W. Hess, A. Kyprianidis, P. Becker, H. Kaplan, A. V. Gorshkov, Z.-X. Gong, and C. Monroe. Observation of a many-body dynamical phase transition with a 53-qubit quantum simulator. *Nature*, 551(7682):601–604, November 2017.

Acknowledgements

At this point I would like to take the opportunity to thank all people who directly or indirectly contributed to this work.

First of all, I express my sincere gratitude to my supervisor Prof. Dr. Christian Ospelkaus who let me join his research group in Hannover already during my studies and taught me most of what I know about quantum physics, ions and electronics. Thank you for supporting me in so many different aspects over all our years together.

I would like to extend my gratitude to my second referee Prof. Dr. Piet O. Schmidt who welcomed me in the QUEST Institute at PTB and was always deeply interested in what we are currently working on. Thanks for all your thoughts and support during the last 5 years.

Furthermore, I wish to thank Prof. Dr. David Lucas to be my third referee and Prof. Dr. Klemens Hammerer to chair my defense.

Special thanks goes to Giorgio Zarantonello with whom I spent most of my time in the lab installing ion traps and taking measurements. I still cannot believe how quickly everything worked out after we spent all the years overcoming never ending obstacles. Thanks to you and all our discussions, like when commuting from Hannover to Braunschweig, I gained many interesting aspects on our experiment. I would also like to thank our Post-Doc Dr. Amado Bautista-Salvador for fabricating all our operated ion traps and developing the multi-layer fabrication process which opens promising perspectives for the future. I always enjoyed my time with you in and outside the office. I further wish to thank Dr. Martina Wahnschaffe and Dr. Matthias Kohnen. Without their work this thesis would have not been possible as it is. Martina developed the simulation model which enabled the design of all operated traps and was, alongside with Matthias, decisively involved in the construction of

the initial apparatus. A huge thank goes also to Dr. Steven King and Dr. Tobias Leopold from the HiCI experiment. Thanks for the fun time and commenting on parts of my thesis. I also like to thank my office mate Jonathan Morgner from whom I received helpful comments about my thesis and who is currently working on the 'Argon chamber' and the new trap RF circuit. I am sure that Giorgio and you will soon push the experiment to new levels. My grateful thanks also go to Marius Schulte and Prof. Dr. Klemens Hammerer for the fruitful collaboration we had about the error budget analysis. I also thank Timko Dubielzig for his very last comments on my thesis.

In addition to the ones mentioned above, I wish to thank all other members from the QUEST Institute at PTB as well as the research groups of Christian and Silke Ospelkaus at IQO in Hannover. It was always a pleasure to work or socialize with you all!

Finally, I would like to thank my family and my girlfriend, Marlen, for putting so much trust in me throughout my whole time as a PhD student. Especially the last few months would have been so much harder without your continuous motivation and support.

List of publications

- H. Hahn, G. Zarantonello, M. Schulte, A. Bautista-Salvador, K. Hammerer, and C. Ospelkaus. Integrated $^{9}Be^{+}$ multi-qubit gate device for the ion-trap quantum computer. *arXiv:1902.07028 [quant-ph]*, February 2019, in submission.

- H. Hahn*, G. Zarantonello*, A. Bautista-Salvador, M. Wahnschaffe, M. Kohnen, J. Schoebel, P. O. Schmidt, and C. Ospelkaus. Multilayer ion trap with 3-dimensional microwave circuitry for scalable quantum logic applications. *arXiv:1812.02445 [quant-ph]*, December 2018, in submission.
  * these authors contributed equally

- A.-G. Paschke, G. Zarantonello, H. Hahn, T. Lang, M. Marangoni, C. Manzoni, G. Cerullo, and C. Ospelkaus. Versatile control of $^{9}Be^{+}$ ions using a spectrally tailored UV frequency comb. *Physical Review Letters*, 122(12):123606, March 2019.

- A. Bautista-Salvador, G. Zarantonello, H. Hahn, A. Preciado-Grijalva, J. Morgner, M. Wahnschaffe, and C. Ospelkaus. Multilayer ion trap technology for scalable quantum computing and quantum simulation. *New Journal of Physics*, 21(4):043011, April 2019.

- M. Wahnschaffe, H. Hahn, G. Zarantonello, T. Dubielzig, S. Grondkowski, A. Bautista-Salvador, M. Kohnen, and C. Ospelkaus. Single-ion microwave near-field quantum sensor. *Applied Physics Letters*, 110(3):034103, January 2017.

Henning Hahn

Brauhofstr. 4
30449 Hannover

Research

04/2014 - 07/2019	**Doctoral Studies** Physikalisch-Technische Bundesanstalt & Leibniz Universität Hannover *PhD thesis in the group of Prof. Dr. C. Ospelkaus*
11/2013 - 03/2014	**Stay Abroad** University of Sydney & National Measurement Institute, Australia *Guest researcher in the group of Prof. Dr. M. Biercuk*

University

10/2009 - 09/2012	**Master of Science (Physics)** Leibniz Universität Hannover, Institut für Quantenoptik *Master thesis in the group of Prof. Dr. C. Ospelkaus*
09/2010 - 02/2011	**Stay Abroad** Universidad de Salamanca, Spain *ERASMUS Programme*
10/2006 - 12/2009	**Bachelor of Science (Physics)** Leibniz Universität Hannover, Laserzentrum Hannover *Bachelor thesis in the group of Prof. Dr. Lubatschowski*

School

06/1991 - 06/2005	**Abitur** Gymnasium Groß Ilsede